

**Gas system, gas quality monitor
and detector control**
of the
ALICE Transition Radiation Detector
and studies for a pre-trigger data read-out system

Dissertation
zur Erlangung des Doktorgrades
der Naturwissenschaften

Vorgelegt beim Fachbereich Physik
Institut für Kernphysik



Nora Pitz
geboren in Wetzlar/Germany

Frankfurt/Main, Mai 2012
(D 30)

vom Fachbereich Physik der
Johann Wolfgang Goethe-Universität
als Dissertation angenommen

Dekan Prof. Dr. Michael Huth

Erster Gutachter Prof. Dr. Harald Appelshäuser (Institut für Kernphysik)

Zweiter Gutachter Prof. Dr. Christoph Blume (Institut für Kernphysik)

Datum der Disputation:

Zusammenfassung

Die Teilchenphysik strebt nach dem Verständnis grundlegender physikalischer Gesetze, die über die elementaren Bausteine der Materie sowie Raum und Zeit herrschen. Alles im Universum besteht aus diesen Basisbausteinen, den Elementarteilchen, die von wenigen fundamentalen Kräften beeinflusst werden. Manche Elementarteilchen sind stabil und bilden Materie, andere haben eine flüchtige Existenz und existierten z.B. nur wenige Momente nach dem Urknall, sind aber heute nicht mehr in unserem Universum zu finden. Mit Hilfe von Beschleunigern und der Hochenergiephysik bekommt man stetig einen tieferen Einblick in die Welt der Elementarteilchen und die fundamentalen Wechselwirkungen zwischen ihnen, was die Möglichkeiten zur Erforschung des Aufbaus der Materie erweitert und die Wissenschaft näher zur Beantwortung der grundlegenden Fragen bringt, woraus das Universum besteht und wie es funktioniert.

Aus Theorie und Experimenten entwickelte sich ein Schema, das einen Großteil aller bisherigen teilchenphysikalischen Beobachtungen erklären kann: das sogenannte Standardmodell der Teilchenphysik. Den Gesetzen der speziellen Relativitätstheorie folgend beschreibt es zwölf Elementarteilchen - sechs Leptonen und sechs Quarks (und ihre Antiteilchen) - sowie drei Grundkräfte, mittels derer sie interagieren. Diese Kräfte lassen sich durch ihre Art der Wechselwirkung erläutern. Man unterscheidet zwischen der starken, der schwachen sowie der elektromagnetischen Wechselwirkung. Jede Wechselwirkung hat ihr zugeordnete Austauschteilchen zur Übermittlung der Kräfte: Das masselose Photon wird der elektromagnetischen, die W- und Z-Bosonen der schwachen und acht unterschiedliche Gluonen der starken Wechselwirkung zugeschrieben. Ein weiteres (hypothetisches) Teilchen im Standardmodell ist das Higgs-Boson, mit Hilfe dessen man sich die verschiedenen Massen der

Elementarteilchen durch eine unterschiedlich starke Kopplung an jenes zu erklären erhofft. Das Standardmodell ist allerdings bislang unvollständig, da es weder in der Lage ist, die gravitative Wechselwirkung zu erklären, noch die drei anderen Grundkräfte in einer einzigen Theorie zusammenzufassen. Erfolgreich wurden bisher nur die elektromagnetische und schwache zur elektroschwachen Kraft vereinigt. Zudem versagt es in der Beschreibung der Masse der Neutrinos und beinhaltet viele freie Parameter, die nicht aus der Theorie hervorgehen, sondern experimentell bestimmt werden müssen. Um den Lösungen zu diesen und weiteren Problemen näher zu kommen, gibt es bereits alternative Modelle und erweiternde Theorien, die jedoch Vorhersagen in bisher unter Laborbedingungen nie erreichten Energiebereichen beinhalten. Diese enormen Energien können nur bei einer Teilchenkollision in einem Hochenergie-Beschleuniger entstehen. Der Large Hadron Collider (LHC) am Kernforschungszentrum CERN bei Genf soll Zugang zu diesen unbekanntem Energiebereichen schaffen, indem er es ermöglicht, zum einen Protonen (einfach positiv geladene Teilchen), zum anderen Bleikerne (82-fach positiv geladene Teilchen) auf nahezu Lichtgeschwindigkeit zu beschleunigen und damit auf Energien von bis zu 7 TeV (pro Proton) und 574 TeV (pro Bleikern) zu bringen.

Die bei den Kollisionen entstehenden Teilchen werden im Rahmen verschiedener Experimente mit Hilfe von Detektoren registriert. Die vier größten sind namentlich ATLAS (A Toroidal LHC ApparatuS), CMS (Compact Muon Solenoid) und LHCb, die sich hauptsächlich auf Proton-Proton-Kollisionen konzentrieren sowie der ALICE-Detektor (A Large Ion Collider Experiment), der im Bereich der Schwerionenphysik bei Blei-Blei-Kollisionen für eine Reihe von Observablen ausgelegt ist, sich aber vor allem dem Nachweis und der Untersuchung des sogenannten Quark-Gluon-Plasmas (QGP) widmet. Neben Schwerionenkollisionen wird der ALICE-Detektor allerdings auch leichtere Stoßsysteme in Proton-Proton-Kollisionen untersuchen. Bei einer Schwerionenkollision entsteht ein Feuerball von sehr hoher Dichte und Temperatur. Übersteigt diese Temperatur einen kritischen Wert, so existieren Quarks und Gluonen Theorien zufolge nicht mehr in gebundenem Zustand. Es bildet sich das QGP, in dem sie sich quasi frei bewegen. Man nimmt an, dass sich das frühe Universum kurz nach dem Urknall in einem solchen Zustand befunden haben muss.

Mit der Zeit expandiert der Feuerball und kühlt dabei ab. Wird die kritische Temperatur wieder unterschritten, kommt es zur (Re-)Hadronisierung bzw. Bildung einer Vielzahl von Mesonen und Baryonen, die während des Weiteren Abkühlens voneinander entkoppeln und den Feuerball verlassen. Dabei können mehrere Zehntausend zu detektierende Teilchenspuren entstehen.

Neben dem Nachweis und der Erforschung der Eigenschaften des Higgs-Bosons sowie der Erzeugung und Untersuchung des Quark-Gluon-Plasmas verfolgt die Wissenschaft mit Hilfe des LHC weitere Ziele. Unter anderem strebt man nach der Untersuchung möglicher Substrukturen von Quarks und Leptonen, der Suche nach supersymmetrischen Teilchen und damit Hinweisen auf eine Theorie zur Vereinheitlichung der o.g. Grundkräfte (“Grand Unified Theory”) und der “Superstringtheorie”. Desweiteren erhofft man sich die Aufklärung der Struktur von dunkler Materie und die Klärung der Materie-Antimaterie-Asymmetrie des Universums.

Wie bereits erwähnt ist ALICE das einzige LHC-Experiment, das explizit Fragestellungen im Bereich der Schwerionenphysik in den Mittelpunkt seiner Forschungen stellt. Die einzelnen ALICE-Subdetektoren wurden dazu ausgelegt und optimiert, unterschiedliche Signaturen des erwarteten Quark-Gluon-Plasmas nachzuweisen und damit dessen Erforschung zu ermöglichen. Der ALICE-Detektor kann generell in zwei Bereiche unterteilt werden: den zentralen Detektorteil (Central Barrel) und den anschließenden Myon-Arm. Insgesamt hat er eine Länge von 25 m bei einem Durchmesser von 16 m und einem Gewicht von ca. 10.000 t.

Der Übergangsstrahlungsdetektor (Transition Radiation Detector - TRD) ist einer der zentralen Detektoren in ALICE. Seine Hauptaufgabe liegt in der Elektronenidentifikation bei Impulsen $p_t > 1 \text{ GeV}/c$, da hier die Messungen des spezifischen Energieverlustes (dE/dx) der Zeitprojektionskammer (Time Projection Chamber - TPC) - ein weiterer zentraler Detektor - nicht mehr ausreichen. Die Schwierigkeit bei der korrekten Identifikation von Elektronen in diesen Impulsbereichen liegt darin, dass um einige Größenordnungen mehr Pionen erzeugt werden. Der TRD bestimmt dennoch Elektronen mit einer Güte von mehr als 90%, worin nur ein Anteil von unter 1% an Pionen als Elektronen falsch identifiziert werden. Daneben liefert der TRD ein schnelles Triggersignal für geladene Teilchen mit hohem Transversalimpuls

$p_t > 3 \text{ GeV}/c$ und leistet einen wesentlichen Beitrag zur Optimierung der Spurverfolgung von Reaktionsprodukten der Teilchenkollisionen. Sein vollständiger Aufbau umfasst 18 Supermodule, die zylindrisch um die Strahlachse des LHC angeordnet sind. Derzeit sind 13 Supermodule installiert und funktionsfähig. Ein SM enthält entsprechend seiner Position in ALICE entweder 30 oder 24 Kammern, die jeweils aus einem Radiator zur Erzeugung von Übergangsstrahlung, einer gasgefüllten Driftkammer mit angrenzendem Verstärkungsbereich und der Auslese-Elektronik bestehen. Insgesamt ist der TRD eine Anordnung von 522 Kammern und wird mit ca. 28 m^3 eines Xe-CO₂ [85-15%] Gasgemisches betrieben.

Die Arbeit für die vorliegende Dissertation umfasste Entwicklung, Inbetriebnahme, Prüfung, Wartung und Betrieb von Detektorteilen des TRD, mit dem Hauptaugenmerk auf seinem Gassystem und Gasqualitätsmonitor, der Verbesserung der Steuerungssoftware, sowie Studien zur Realisierbarkeit eines neuen Pretrigger-Moduls zur Datenauslese.

Das TRD-*Gassystem* mischt, verteilt und zirkuliert das operative Gasgemisch durch den Detektor. Für seinen reibungslosen Betrieb wurde es im Rahmen dieser Arbeit kontinuierlich überwacht, kontrolliert und gewartet und seine Gesamtoptimierung durch die Eindämmung von Gaslecks, fortlaufende Verbesserungen sowie Planung und Durchführung von Upgrades erreicht.

Gasqualitätsmonitore vom Typ "GOOFIE" (Gas prOportional cOunter For drift-ing Electrons - Gas-Proportionalzähler für driftende Elektronen) können in Gasdetektoren als Online-Überwachungssystem der Driftgeschwindigkeit, Gasverstärkung und Gaseigenschaften verwendet werden. Eines dieser Geräte wurde erfolgreich in das TRD-Gassystem eingebaut und in Betrieb genommen, ein weiteres überwacht das Gas der TPC. Beide Geräte wurden auf die spezifischen Bedürfnisse der Detektoren angepasst, standen unter ständiger Überwachung und Kontrolle, und mussten sowohl auf Hard- als auch auf Softwareseite weiterentwickelt werden.

Um die Bedienung des TRD zu optimieren, wurden als Teil dieser Arbeit Modifikationen an seiner DCS-Software (*Detector Control System*) durchgeführt, die zur Überwachung, Steuerung, dem Betrieb, der Regulierung und Konfiguration von Hardware- und Computeranlagen eingesetzt wird. Das DCS ist so konzipiert, dass

ein Benutzer mit Hilfe von Anwenderschnittstellen, die die von den Systemen kommenden Informationen anzeigen, mit den Geräten interagieren kann. Der Schwerpunkt dieser Arbeit lag auf der Verbesserung des Designs der Benutzeroberfläche sowie Optimierung der Bedienfreundlichkeit und damit der Operation des TRD.

Während des laufenden Betriebs erfordert die Elektronik des TRD ein frühes Start-Signal (“Pretrigger”) von den Vorwärtsdetektoren oder dem Time-Of-Flight-Detektor. Eine neues Hardware-Modul soll für die Sammlung und Auslese aller zum Pretrigger-Signal beitragenden ALICE-Triggerdaten sorgen. Dieses Modul mit dem Namen *PIMDDL* (Pre-trigger Interface Module Detector Data Link - Pretrigger-Schnittstellenmodul zur Detektor-Daten-Verbindung) soll mit Hilfe der gesammelten Daten die Vorhersage, Überprüfung und Visualisierung der vollen Funktionalität des Pretrigger-Systems ermöglichen. Darüber hinaus soll es sämtliche Funktionalitäten der sogenannten Control-Box Bottom bereitstellen sowie die bereits bestehenden Aufgaben des “PIM” (Pretrigger Interface Module) erfüllen, um diese beiden Module in der Zukunft zu kombinieren und zu ersetzen. Die konzeptionelle Idee wurde im Rahmen dieser Arbeit auf Realisierbarkeit hin untersucht. Nach der finalen Ausarbeitung, Konstruktion und ersten Tests an der Universität Heidelberg (Physikalisches Institut) wurden im TRD-Teststand am CERN/Point 2 die Funktionalitäten erfolgreich überprüft. Die Komplettierung der Software und der Einbau in ALICE stehen noch aus.

Abstract

The main purpose of the Transition Radiation Detector (TRD) located in the central barrel of ALICE (A Large Ion Collider Experiment) is electron identification for separation from pions at momenta $p_t > 1$ GeV/ c , since in this momentum range the measurements of the specific energy loss (dE/dx) of the Time Projection Chamber (TPC) is no longer sufficient. Furthermore, it provides a fast trigger for high transverse momentum charged particles ($p_t > 3$ GeV/ c) and makes a significant contribution to the optimization of the tracking of reaction products in heavy-ion collisions. Its whole setup comprises 18 supermodules out of which 13 are presently operational and mounted cylindrically around the beam axis of the Large Hadron Collider (LHC). A supermodule contains either 30 or 24 chambers, each consisting of a radiator for transition radiation creation, a drift and an amplifying region followed by the read-out electronics. In total, the TRD is an array of 522 chambers operated with about 28 m³ of a Xe-CO₂ [85-15%] gas mixture.

During the work of this thesis, the testing, commissioning, operation and maintenance of detector parts, the gas system and its online quality monitor, improvements on the detector control user-interface and studies about a new pre-trigger module for data read-out have been accomplished.

The TRD *gas system* mixes, distributes and circulates the operational gas mixture through the detector. Its overall optimization has been achieved by minimizing gas leakage, surveying, controlling, maintaining and continuously improving it as well as designing and carrying out upgrades.

Gas quality monitors of the type “GOOFIE” (Gas prOportional cOunter For drifting Electrons) can be used in gaseous detectors as on-line monitors of the electron drift velocity, gain and gas properties. One of these devices has been implemented

within the TRD gas system, while another one surveys the gas of the TPC. Both devices had to be adapted to the specific needs of the detectors, were under constant surveillance and control, and needed to be further developed on both hardware and software side.

To improve the operation of the TRD, modifications on its DCS software (*Detector Control System*) used for monitoring, controlling, operating, regulating and configuring of hardware and computing devices have been carried out. The DCS is designed to enable an operator to interact with equipment through user interfaces that display the information from the system. The main focus of this work was laid on the optimization of the usability and design of the user interface.

The front-end electronics of the TRD require an early start signal (“pre-trigger”) from the fast forward detectors or the Time-Of-Flight detector during the running periods. The realization of a new hardware concept for the read-out of the TRD pre-trigger system has been studied and first tests were performed. This new module called *PIMDDL* (Pre-trigger Interface Module Detector Data Link) is meant to acquire all data necessary to simulate and predict the full pre-trigger functionality, and to verify its proper operation. Furthermore, it shall provide all functionalities of the so-called Control Box Bottom as well as keep the functionalities of the already existing PIM (Pre-trigger Interface Module) in order to combine and replace these two modules in the future.

Contents

1 Particle Physics	1
1.1 Introduction	1
1.2 Quantum Chromodynamics	4
1.3 The Quark-Gluon Plasma	6
2 The Large Hadron Collider	13
3 A Large Ion Collider Experiment	19
4 Transition Radiation Detector	29
4.1 Transition Radiation	29
4.2 Detectors	31
5 The TRD Gas System	39
5.1 Overview	39
5.2 The Main Modules	44
5.3 Analysis Of The Gas	48
5.4 Gas Purification	57
5.5 Surveillance And Control Software	63
5.6 Operating, Maintaining, Upgrading	65
6 GOOFIE - A gas quality monitor	81
6.1 Motivation	81
6.2 Theoretical Basics	82
6.3 Layout And Principle Of Operation	83
6.4 Data acquisition and analysis	89

Contents

6.5	Maintenance, Modifications, Upgrades	93
7	Detector Control System - DCS	105
7.1	Introduction	105
7.2	PVSS	108
7.3	TRD DCS	110
7.4	Upgrade Of The TRD UI	113
8	Read-Out Of The TRD Pre-Trigger System	123
8.1	The ALICE Trigger System	123
8.2	The ALICE Data Acquisition System	131
8.3	The Pre-Trigger System	133
8.4	Studies On Realizing The Read-Out	140
	Summary And Outlook	149
	List of Figures	153
	List of Tables	163
	References	165
	Danksagung	173

1 Particle Physics

This chapter gives a short introduction to particle physics and quantum chromodynamics in general. Focus is then laid on discussing the quark-gluon plasma since the main goal of the ALICE detector is to provide insight into this state of matter that is believed to have existed just after the Big Bang.

1.1 Introduction

Particle physics deals with the search for the fundamental particles that form matter and the forces with which they interact. The forces can be described by the **interactions** between these particles; their basic characteristics are summarized in table 1.1.

Interaction	relative strength	effective range [m]	mediator(s)	effected particles
strong	1	10^{-15}	8 gluons	quarks
gravitation	10^{-38}	∞	graviton	all
electromagn.	10^{-2}	∞	photons	quarks charged leptons
weak	10^{-5}	10^{-18}	W^{\pm}, Z^0	quarks leptons

Table 1.1: Fundamental interactions and their characteristics [1].

One of the major goals of the research in this field of physics is understanding all those forces in detail and to unite them in one global description. So far it

1 Particle Physics

was possible to find a theory to merge the electric and magnetic forces within the **electromagnetic interaction**, as well as a unification between the electromagnetic and the weak interaction - the **electroweak interaction**. There are many approaches to reconcile the electroweak and the **strong force** within a common (grand unified) theory but none is yet complete. The biggest problems come from the **gravitational force** since it is the least understood at the microscopic level. On the experimental side, there are technological challenges as a consequence of the immense energies required to directly verify the existence of the particles predicted by the theories. The interactions are described with the help of quantum field theories (**quantum chromodynamics (QCD)**, **Glashow-Weinberg-Salam model** of the electroweak interaction, **quantum electrodynamics (QED)**) and **general relativity** which postulate systems represented by an infinite number of dynamical degrees of freedom - **fields** - and the particles mediating the forces - **gauge bosons**. The effective ranges of the forces vary a lot, characterized by the mass of the exchanged particle [2].

The gravitation has a hardly measurable effect on microscopic systems, thus it is ignored when talking about particle physics. The other forces build the fundamentals of the **Standard Model** of the elementary particles, which groups most of the known subatomic particles. It is based on the twelve elementary particles of spin- $\frac{1}{2}$ known as fermions (6 quarks and 6 leptons plus their anti-particles) and the gauge bosons mediating the strong (eight gluons: g_α ; $\alpha = 1, \dots, 8$), weak (W^\pm and Z bosons) and electromagnetic (photon: γ) interactions plus the hypothetical spin 0 Higgs boson. The gauge bosons have spin 1, whereas the graviton is supposed to be a spin-2 particle. In the Standard Model the fermions are the particles that make up matter. Noticeably, the quarks with electric charge $Q = \frac{2}{3}$ come in a group of three, as do the quarks with $Q = -\frac{1}{3}$ and the electron, muon and tau ($Q = -1$) as well as their neutrinos known as the electron, muon and tau neutrinos (ν_e, ν_μ, ν_τ ; $Q = 0$). The six types of quarks, known as flavors, are grouped into three different generations according to their mass: up and down, charm and strange, top and bottom. Unlike the force-carrying particles, the matter particles have associated antimatter particles with the same mass but opposite electric charge and quantum numbers. Theoretical

physics has not yet explained why there are three generations of particles that form matter. With the above described 16(+1) fundamental particles, which can be found in figure 1.1, the Standard Model describes approximately 200 composite particles and their interactions.

Quarks have an additional quantum number, the **color**, which can be of three types: **red, green, blue** (generically denoted as q_i , $i = 1, 2, 3$). Since color is not seen in nature, the elementary quarks must be confined in the observable matter particles, the **colorless** hadrons. They are made of either two or three quarks. Mesons are formed by a quark and anti-quark pair (e.g. $\pi^+ = u\bar{d}$), whereas baryons are made of 3 quarks or 3 anti-quarks (e.g. $p = uud$) [3].

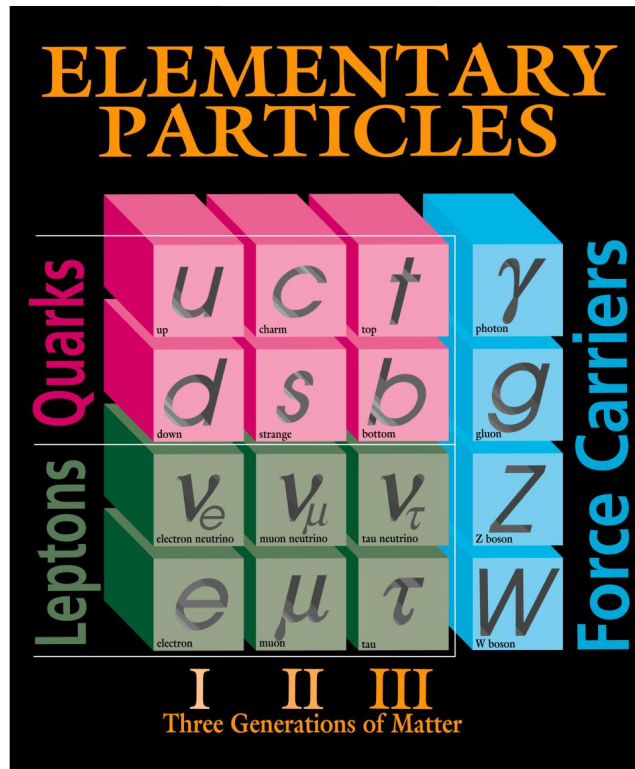


Figure 1.1: The model to describe the particles and forces that comprise all that surrounds us is called the **Standard Model** - it has been widely successful in explaining observed phenomena and correctly predicting new measurements. The above picture shows the elementary particles and gauge bosons (i.e. the force “carriers”) [4].

1.2 Quantum Chromodynamics

QCD describes the **strong interaction** which affects all hadrons (baryons and mesons), i.e. all particles built by quarks. The exchange/gauge bosons of the strong interaction are its eight massless gluons, each carrying a color and an anti-color charge which lets them not just intermediate between the quarks but also interact amongst themselves. Moreover, they can split into a quark-antiquark pair. The gluon exchange thus forms a complex web of gluons, quarks and antiquarks which makes the strong nuclear force difficult to grasp. These vector bosons have spin 1 and a negative intrinsic parity. The strength of the interaction between two quarks is mainly determined by the strong coupling constant α_S . α_S is an effective constant since it is dependent of Q^2 - the momentum transfer between the quarks. In comparison to the electromagnetic interaction, where α is (basically) independent of Q^2 , this dependence is very strong. One way of seeing it: a quark is surrounded by a cloud of virtual particles (gluons and quark-antiquark pairs) and the color charge of a quark is partly compensated (“screened”) by the color charges of the quark-antiquark pairs in the cloud. However, unlike the electrically neutral virtual photons in the vicinity of an electron (QED), the virtual gluons in the vicinity of a quark have their own color charge, wherefore they can interact with each other and produce a virtual $q\bar{q}$ -pair or radiate and absorb another gluon. The net effect of polarization of virtual gluons in the vacuum is to enhance (“antiscreen”) the electric and strong charge. The charge seen by the interacting particles gets smaller the closer they get. The antiscreening from the gluons is much stronger than the screening and as a result the color charge of the quarks is not shielded but increased [3]. α_S , in the first order of the perturbation theory of strong interactions/QCD, is [1]:

$$\alpha_S(Q^2) = \frac{12\pi}{(33 - 2n_f)} \ln(Q^2/\Lambda^2) \quad (1.1)$$

$n_f \approx 3.6$ is the number of involved quarks (**u, d, c, s, t, b**) in the observed momentum transfer (pair production) and the factor 33 comes from the gluon interactions. Equation 1.1 is only valid for $Q^2 \gg \Lambda^2$, where Λ is an additional parameter, setting the scale of renormalization. The coupling constant becomes “strong” roughly at

the scale of Λ . It cannot be derived from theory itself but has to be determined experimentally. It has been established to use the mass of the Z^0 boson as a renormalization point or common scale for the determination of Λ . The results of the measurements of α_S can be seen in figure 1.2 which puts the average value of Λ at (213 ± 9) MeV ($\alpha_S(M_{Z^0}) = 0.1184 \pm 0.0007$) [5].

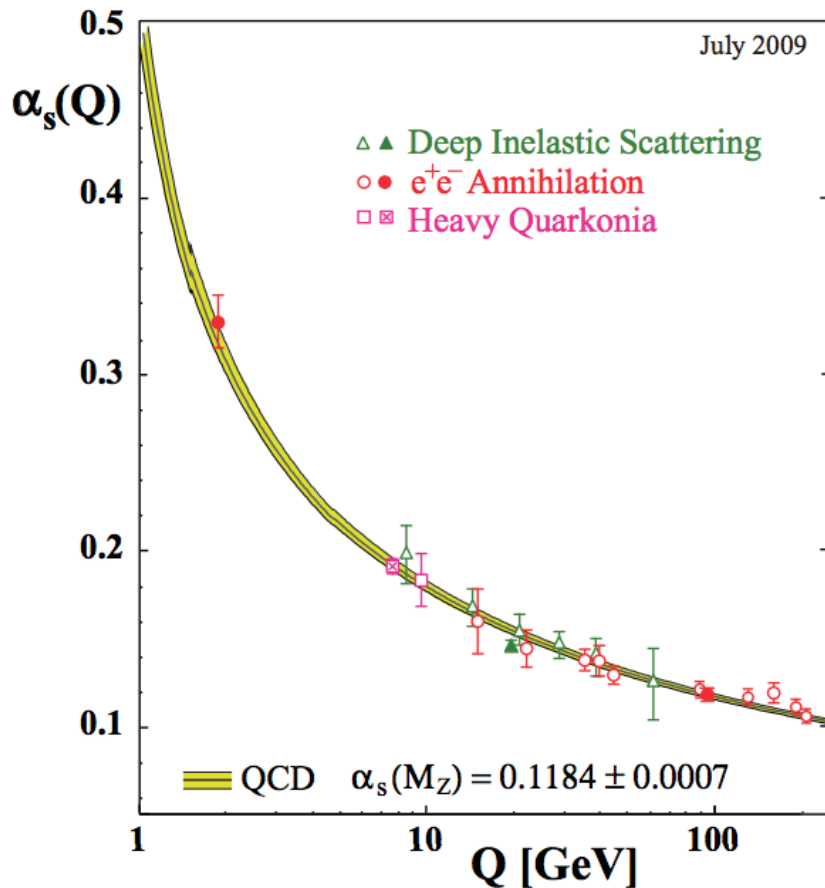


Figure 1.2: Measurements of the strong coupling constant α_S as a function of the respective energy scale Q [5].

The fact that α_S decreases with decreasing distance and hence higher Q^2 can be pictured by a potential between the quark and antiquark of a $q\bar{q}$ -pair. It has a short range Coulomb-like term and a long range linear term. As the distance r between two quarks becomes larger the potential strength and therefore the energy to separate the quarks increases.

$$V_{q\bar{q}} = -\frac{4}{3} \frac{\alpha_S(r) \hbar c}{r} + k \cdot r \quad (1.2)$$

For $r \rightarrow \infty$, Q^2 strives towards 0, which means that $\alpha_S(Q^2)$ becomes so big that the quarks are “trapped” within the hadrons and cannot be seen as free particles. This is generally referred to as **confinement**. At small Q^2 , perturbative calculations can not be applied. For a decreasing r , on the contrary, the first term in equation 1.2 becomes dominant leading to $\alpha_S \rightarrow 0$ at the limit $r \rightarrow 0$ ($Q^2 \rightarrow \infty$). This is referred to as **asymptotic freedom**, since the quarks move more or less freely and without interaction within hadrons [6].

1.3 The Quark-Gluon Plasma

Apart from the three well-known states of aggregation (solid, fluid and gaseous) there is a fourth one called **plasma**. It can be understood as an ionized gas. Spoken in general terms, heating a gas eliminates its molecular bonds and therefore it splits into its constituents. Further heating will lead to ionization of the particles, so that the gas contains charged particles - positive ions and negative electrons - thus it is considered a plasma. At sufficiently high temperatures or energy densities, QCD predicts a phase transition of confined hadronic matter to a deconfined state within which the confinement of the quarks and gluons has been eliminated, whereby they behave quasi-free. It is called **Quark-Gluon Plasma** (QGP). In the standard Big Bang model the universe went through that phase in the first moment after the Big Bang before it expanded and cooled down sufficiently for quarks and gluons to hadronize into nucleons and other hadrons. In today’s universe the QGP probably only exists in the center of compact stars such as neutron stars or black holes [7].

The only way one can achieve temperatures and densities relevant for strong interactions and creating a QGP is by colliding two large nuclei at high energy. Lead and gold nuclei have been used for such collisions at the Super Proton Synchrotron (SPS) and Large Hadron Collider (LHC) at CERN (Conseil Européen pour la Recherche Nucléaire) and the Relativistic Heavy Ion Collider (RHIC) at the Brookhaven Na-

1.3 The Quark-Gluon Plasma

tional Laboratory (BNL). In the experiments the nuclei are accelerated to ultra-relativistic speeds and slammed into each other while being Lorentz contracted (they appear as disks). They mainly pass each other, but when they do collide a hot volume called a **fireball** is created that behaves like a thermalized system, characterized by a temperature T and a baryochemical potential μ which is the amount of energy needed to add a baryon (such as a proton or a neutron) to the system. This fireball expands and cools down adiabatically and once below a critical temperature T_c , it disintegrates into particles, i.e. it comes to (re-)**hadronisation** - a huge number of mesons and baryons is created, which decouple and leave the fireball during its cooling process tracing a trajectory on the phase diagram of T over the chemical potential μ as can be seen in figure 1.3.

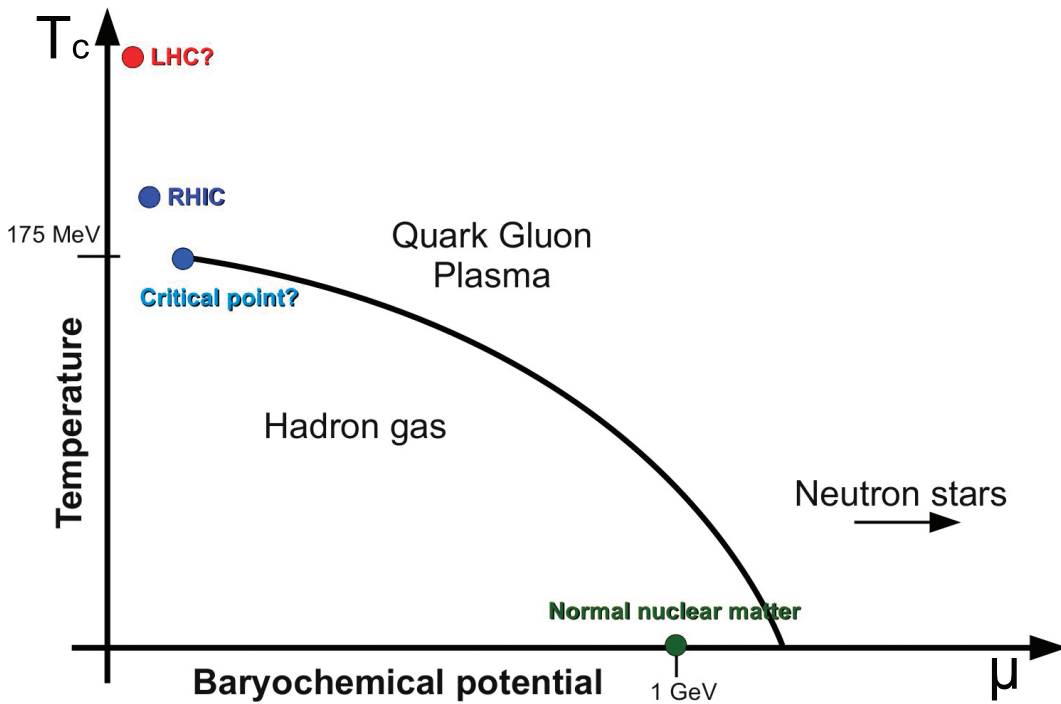


Figure 1.3: The QCD phase diagram: One of the primary goals of the experimental programs at BNL (RHIC) and CERN (LHC) is to produce and study the quark-gluon plasma. The line shows the phase boundaries for the indicated phases. The blue circle depicts the critical point. Temperatures reachable with the two accelerator facilities are indicated [7].

1 Particle Physics

This all happens on a very short time scale of $\approx 10^{-23}$ - 10^{-20} seconds which makes it extremely difficult to identify the signal of the quark-gluon plasma formation. Qualitatively the QGP can be explained with the following two scenarios:

- **1:** Each nucleon in a nucleus occupies ten times more space than its actual size. Squeezing the nucleus to ten times its usual density would lead to an overlap of the nucleons inside. Hence, they would not be individual particles anymore and the quarks and gluons could move boundless in the whole nuclear volume.
- **2:** When increasing the temperature of the nucleus but keeping the nucleon density, at T_c there would be enough energy available to the individual nucleon-nucleon collisions to increase the hadronic density through creation of mesons. Equally, the frequency of interactions would increase so much that it is no longer possible to assign quarks and gluons to a particular nucleon [1].

T_c can be derived by comparing the pressures of the hadronic and the QGP phase at the transition point which leads to $T_c \approx 2 \times 10^{12}$ K or 150 - 180 MeV. With the LHC, temperatures above $3 T_c$ should be reachable and therefore it should be possible to create a QGP, as discussed for example in [8]. The dedicated detector to study all aspects of heavy ion collisions and the properties of the QGP is ALICE.

Probes of the QGP

There are several probes of the conditions of the quark-gluon plasma that can be accessed with the help of the ALICE TRD to be described in detail in chapter 4. These probes are:

- **Quarkonium states ($c\bar{c}$, $b\bar{b}$)**

Heavy flavor particles such as J/Ψ , Ψ' and Υ are supposedly excellent probes for the investigation of the QGP [9]. Firstly, open charm and beauty hadrons should be sensitive to the energy density through the in-medium energy loss of the heavy quarks. Secondly, quarkonium states are expected to dissociate and should therefore be sensitive to the initial temperature of the system [10]. The J/Ψ particle, for example, forms a prominent peak at $M = 3.1$ GeV in

the di-lepton invariant mass spectrum which makes it rather easily observable. It is expected to dissolve much easier in a deconfined medium (i.e. the quark-gluon environment) compared to a hadronic medium. This can be understood as a result of color-screening in the plasma which is analogue to the Debye screening of an electric charge in QED. If the temperatures are high enough, the quarks are screened from each other, the particles disengage and cannot be measured anymore. In case of the J/Ψ , this means that the binding forces between the constituent charm and anticharm quarks would be cut off and the number of J/Ψ particles in the final state should be significantly reduced. This process can be pictured as follows: If the J/Ψ has to pass a hot plasma on its way to a detector, it melts away. In contrast to the neutrons and protons, which “freeze out” again as soon as the temperature decreases, the J/Ψ particles are permanently lost. The reason: While protons and neutrons are only built with the light and numerous up and down quarks, the charm quarks are very rare in a QGP, and it is extremely unlikely that the few bind together again. In 1986 Matsui and Satz predicted this decrease in the number of J/Ψ particles, since the color-screening length is less than the bound state radius of a J/Ψ [11]. Analysis of the data collected by the NA50 collaboration with Pb-Pb collisions at 158 GeV/nucleon shows that J/Ψ is anomalously suppressed in central collisions and the observed pattern can be considered as a strong indication for QGP production [12]. Yet, it needs to be taken into account that at high energies more charm pairs can be produced and charmonium regeneration models predict the production of charmonium bound states through the recombination of the quark and antiquark during hadronization. This would lead to an enhancement of quarkonia at high energies rather than a suppression [13]. This phenomenon is most likely to be present at the high LHC energies.

- **Electrons from open heavy-flavor decays**

Open charm and beauty can be detected in the semi-leptonic decay channel of D and B mesons: $(D, B \rightarrow e^\pm + X)$ [14]. To identify the involved electrons there are two possible methods to be used:

1 Particle Physics

1) Separation of background electrons from the inclusive electron spectrum, i.e. the electrons from heavy flavor decays. This background can be obtained by summing up contributions of electrons from di-electron decays of light neutral mesons, J/Ψ and Υ decays, photon conversion in the detector material or direct radiation. Subtracting those from the total amount of electrons, the contribution from open charm and beauty remains.

2) Isolation and direct measurement of electrons from beauty decays. These electrons are displaced with respect to the primary vertex, i.e. they do not point to the interaction vertex due to the relatively large decay length of B mesons [9].

- **Electromagnetic signals**

Since photons and leptons interact only weakly with a medium they consequently can leave the interaction region without any final state interaction carrying information about the properties of the matter at the time of their production. Direct (thermal) photons are produced in the initial hard parton collisions and provide information about the first moments of the collision. Nonetheless, they are difficult to measure because of the large background of hadronic decays. Production processes can be $q + g \rightarrow \gamma + q$ (Compton scattering) or $q + \bar{q} \rightarrow \gamma + g$ (annihilation) [15]. Di-leptons can equally be used as QGP indicators: Within the plasma a quark-antiquark annihilation can result in the production of a virtual photon, which then decays into a pair of leptons. Production rate and momentum distribution of these pairs is determined by the momentum distribution of quarks and antiquarks in the QGP, which in turn are given by the thermodynamic properties of the plasma. The measurement of those di-leptons can therefore make the plasma's thermodynamic observables accessible. Proving the di-lepton pairs originating from the plasma, however, is difficult due to the fact that at higher masses, the yield of Drell-Yan processes ($q_{h_A} + \bar{q}_{h_B} \rightarrow \gamma^*/Z \rightarrow l + \bar{l}$) from the first collisions most probably exceeds that of thermal di-leptons from a QGP. Additional lepton pairs can originate from hadron-antihadron reactions like $\pi\bar{\pi}$ or the leptonic decay of resonances (ρ, ω, ϕ) [15]. These resonance decays are also an inter-

esting QGP probe, as they are expected to change in the QGP, leading to broadened or shifted resonance masses.

- **Jets**

Another phenomenon that might help reveal the secrets of the quark-gluon plasma is jet quenching. When individual particles collide in a vacuum the debris usually flies out in a pair of jets - narrow cones of particles heading away in opposite directions from the collision point. Particles like pions or kaons detected on one side of the detector are correlated, in terms of total momentum and energy, with particles detected on the opposite side. In case of the heavy ions the jet of particles has to push through the strongly interacting, hot, dense, nuclear matter. The further it has to push, the more energy it loses. One jet from the back-to-back pair might even not escape the fireball at all. Earlier measurements at the BNL and recent measurements of the ATLAS and CMS collaborations at CERN have confirmed that the more head-on the collisions of lead ions, the more unbalanced the energies of the jets streaming out in opposite directions from the collision point get. While one jet may still appear as a narrow cone of particles, the second jet can have a much lower energy, and the cone of particles becomes much more diffused. The imbalance appears when one jet must travel through more QGP to escape the collision area than the other which would make it possible to characterize the medium more precisely [16].

All these probes (except for the jets) require a detector with a high electron identification capability which the TRD is dedicated to (→ chapter 4).

2 The Large Hadron Collider

Located near Geneva/Switzerland at CERN, the European Organization for Nuclear Research, is the **LHC**, at present the largest particle accelerator in the world, designed to collide two particle beams running in opposite directions. This chapter briefly describes the accelerator and gives an outlook on its future upgrade.

With the help of accelerated particles, it was possible since the 1890s to have a deeper look into matter, and thus explore the structure of atoms and their components more accurately. In 1897, the physicist J.J. Thomson used a cathode ray tube to demonstrate that the rays emanating from a heated metal filament were actually particles with negative electric charges [17]. With newer and more powerful accelerators, we now even manage to learn more about the first split second after the Big Bang.

In accelerator physics the so-called **luminosity** is an important parameter since it provides information of how many particles pass through a given area in a certain amount of time. For a storage ring collider like the LHC it is given as

$$L = \frac{N_a N_b n_b f_r}{A} \quad (2.1)$$

with n_b = no. of bunches, $N_{a,b}$ = no. of particles per bunch, f_r = revolution frequency and A = cross-section area of the beam. Using protons with a targeted centre of mass energy of $\sqrt{s} = 14$ TeV per proton pair a luminosity of $L = 10^{34} \text{ cm}^{-2} \text{ s}^{-1}$ could be possible (design values; expected to be reached in 2014). The LHC can also operate as a heavy-ion machine, colliding fully stripped $^{208}\text{Pb}^{82+}$ ions with a centre

2 The Large Hadron Collider

of mass energy of $\sqrt{s_{NN}} = 5.5$ TeV per *nucleon* pair¹ or 1.15 PeV per *nucleus* pair and a peak luminosity of $L = 10^{27} \text{ cm}^{-2} \text{ s}^{-1}$.

After a serious fault in September 2008, which caused the LHC to stop after just nine days of running, proton beams have been circulated successfully again since the end of 2009 with the first recorded proton-proton collisions at an injection energy of 450 GeV per beam. In spring 2010, the first collisions took place between two 3.5 TeV beams (half of the LHC's designed energy). In November 2010, first collisions with heavy ions were recorded. Once circulating beams had been established, they could be accelerated to the full energy of 287 TeV per Pb ion. About 4×10^{14} proton-proton collisions had been taken place until November 2011 when the LHC's 2011 proton run ended to leave space for another month of circulating heavy ions [18]. The operation of the LHC will continue at half energy for protons until the end of 2012, when it goes into a long shutdown to prepare for higher energy starting in 2014. It will presumably run at full energy (pp: 7 TeV per beam) in 2015. The LHC was built into the existing 27 km long tunnel of the **Large Electron Positron collider** (LEP). It has an octagonal shape with eight arcs and eight 528 m long straight sections. Due to the fact that the length of the tunnel is given, the energy of the LHC is maximized by increasing the magnetic field in the dipole magnets, used to guide the particle beams around the ring. It was necessary to use superconducting magnets which operate at a temperature of 1.9 K and make the LHC the largest cryogenic system in the world. A total of 1232 dipole magnets with a nominal dipole field of 8.33 T at a current of 11.8 kA. Since the space in the tunnel is very limited it was impossible to use two separate rings of magnets, wherefore twin bore magnets consisting of two sets of coils and beam pipes within the same mechanical structure and cryostat have been used. Common beam pipes are used close to the four collision points **ATLAS** (A Toroidal LHC Apparatus - point 1), **ALICE** (A Large Ion Collider Experiment - point 2), **CMS** (Compact Muon Solenoid - point 5) and **LHCb** (LHC beauty - point 8) which can be seen in figure 2.1 [19]. The detectors

¹The CM energy of 5.5 TeV per nucleon at an **acceleration energy** of 7 TeV can be derived as follows: lead isotope $^{208}\text{Pb}^{82+}$: $Z = 82$ (atomic/proton number), $N = 126$ (neutron number), $A = 208$ (nucleon/mass number); energy per nucleon: $7 \text{ TeV} \times 82 = 574 \text{ TeV}/208 = 2.76 \text{ TeV/nucleon}$; CM energy: $2 \times 2.76 \text{ TeV} \approx 5.5 \text{ TeV}$

ATLAS and CMS are mainly dedicated to pp physics and intended to analyze the nature of mass, especially finding the Higgs Boson, whereas LHCb should measure CP violation in b-meson systems to better understand the imbalance of matter and antimatter in the universe.

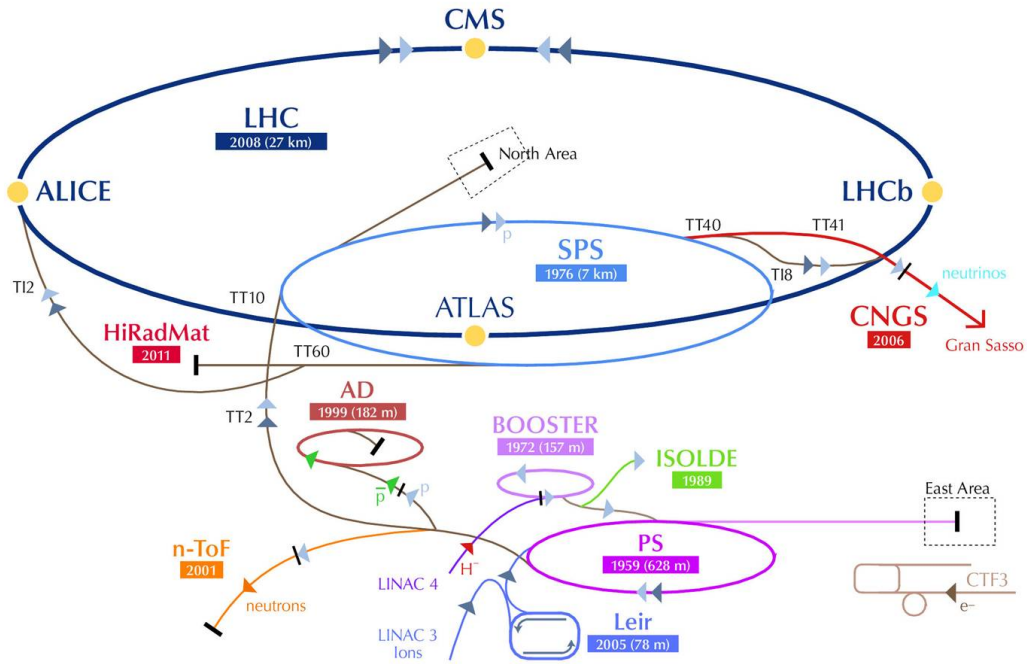


Figure 2.1: The actual (2011) CERN accelerator complex including the four big LHC experiments (ATLAS, CMS, ALICE, LHCb) as well as the Antiproton Decelerator (AD), the ISOLDE (Isotope Separator On-Line) facility, the CNGS (CERN Neutrinos to Gran Sasso) project and the CLIC (Compact Linear Collider Study) test area. [7].

The “Superluminescence” LHC

While the LHC is still setting records such as passing its own maximum integrated luminosity of $\int L dt = 4.9 \text{ fb}^{-1}$, and then breaking the Tevatron² peak luminosity record with $L = 4.67 \times 10^{32} \text{ cm}^{-2}\text{s}^{-1}$, accelerator and detector experts are already

²The Tevatron was the most powerful proton-antiproton synchrotron, located at the Fermi National Accelerator Laboratory (Fermilab), and the second highest energy particle collider in the world after the LHC. The protons and antiprotons were accelerated in a 6.28 km ring to energies of up to 1 TeV. It was shut down in September 2011 after a running period of 28 years [20].

2 The Large Hadron Collider

looking farther into the future and have begun preparatory work for an upgrade which aims at increasing the luminosity of the machine by a factor of 10 (i.e. up to $L = 10^{35} \text{ cm}^{-2}\text{s}^{-1}$), to enhance the chances of finding rare particles [21]. Since the luminosity is the number of particles per unit area per unit time, squeezing more protons into increasingly smaller spaces means an increase of the luminosity, which gives protons a better chance of colliding. Adding up the luminosity over a long period of time provides the integrated luminosity, which is related to the total number of collisions recorded by the detectors. The **super Large Hadron Collider** (sLHC) is the proposed upgrade to the LHC which will be successively extended with several new elements and technical improvements.

In the same manner as now, protons are obtained by removing electrons from hydrogen atoms. They are injected from the LINAC2 (LINear ACcelerator) into the Proton Synchrotron Booster (PSB), from there to the Proton Synchrotron (PS), followed by the SPS, before finally reaching the LHC (figure 2.1). Lead ions enter LINAC3 and the LEIR (Low Energy Ion Ring) before following the same route to maximum acceleration as the protons. Next to the need for better beam characteristics the improvements, as proposed by the sLHC project, are also necessary for reliability of the machines: most of the accelerators are old and operate far from their design parameters and close to hardware limits. For the SPS that means increasing the peak radio frequency (RF) power capability, reducing the impedance of the kickers³ and searching for other possible impedance sources [23]. The proposed SPS+ (Superconducting SPS) shall then provide an injection energy of about 50 GeV to 1 TeV. The PS is foreseen to be replaced by a new PS successor (PS2) with an increased extraction energy up to 50 GeV (from the present 26 GeV). A new 160

³To inject the beam from the SPS into the LHC **kick**ers and **sept**ums are being used. A septum dipole magnet is used to bring the injected beam close to the circulating beam. Then a kicker (a fast pulsing magnet) is fired synchronously with the arrival of the injected beam to deflect it onto the circulating beam path, it basically “stacks” the injected beams one behind the other. At the LHC the septum deflects in the horizontal plane, the kicker in the vertical plane (to fit to the geometry of the tunnels). Extraction is identical, but the process is reversed [22]. The injection from the SPS into the LHC is realized via the two connecting transfer injection lines **TI 2** (length: 2943 meters) and **TI 8** (length: 2694 meters).

MeV linear accelerator (LINAC4) is already being built replacing the LINAC2 to increase the beam emittance out of the PSB by a factor of 2, making an upgrade of the LHC injectors for higher intensity and an increase of the above-mentioned LHC luminosity possible. These modifications shall insure regular delivery of beams to the LHC, reduce its filling time and positively contribute to the overall reliability of the injector complex. A summary of the necessary changes can be seen in figure 2.2. The increased luminosity of the sLHC also demands for upgrades of the experiments (mainly ATLAS and CMS) to deal with the higher collision rates [24].

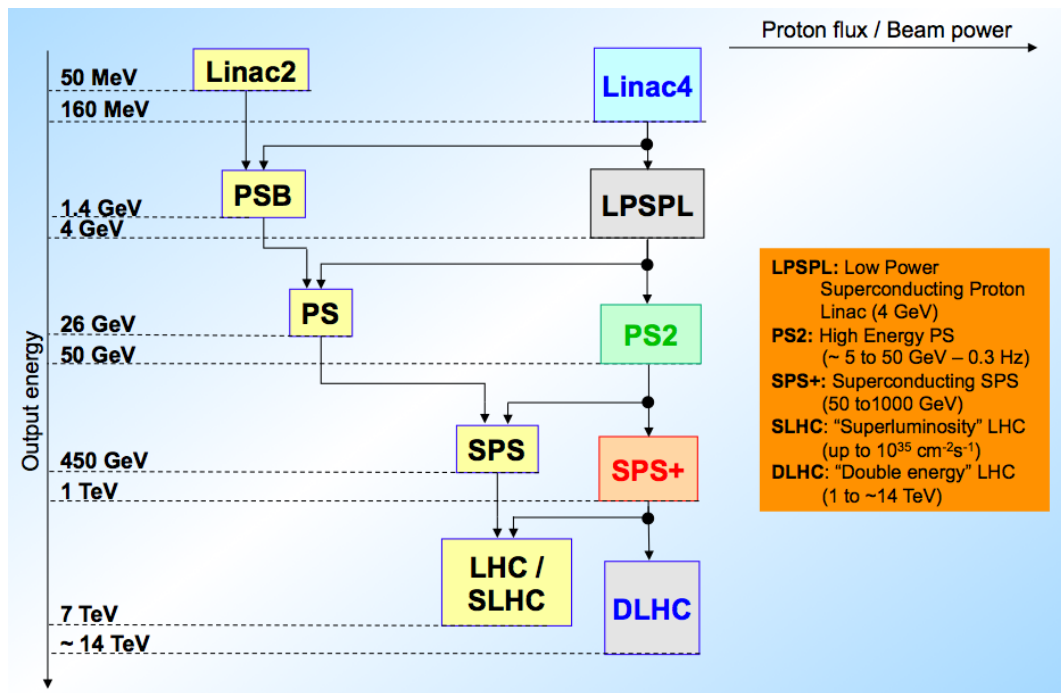


Figure 2.2: Summary of the planned LHC upgrade [25].

3 A Large Ion Collider Experiment

This chapter is dedicated to presenting the ALICE detector.

Its main purpose is the examination of the afore described strongly interacting matter and detecting probes of the quark-gluon plasma. Its sub-detectors can measure and identify a large variety of particles such as pions, kaons, muons, photons, (anti-)protons and electrons (positrons). The experiment investigates a wide range of observables from very low to high transverse momenta ($p_t \approx 100 \text{ MeV}/c - 100 \text{ GeV}/c$) in a low (proton-proton) and very high (lead-lead) particle multiplicity environment. The detectors were designed to deal with up to 8000 particles per unit of pseudo-rapidity $dN_{ch}/d\eta$ ¹. However, more recent studies lowered the expected values of the multiplicity density to 1200 - 2500. Focus is laid on the region close to mid-rapidity where one expects the lowest baryon and highest energy density. Even though ALICE is designed and built to investigate heavy-ion collisions, data is also taken during proton-proton runs to provide reference data and to investigate several QCD topics for which ALICE is complementary to the other LHC experiments. Furthermore, it was used for the commissioning of the detector [26]. The physics requirements and experimental conditions as well as the geometrical limitations - the magnet housing the detector was inherited from the LEP L3 experiment - had set high constraints onto the design of ALICE. Its overall dimensions are $16 \times 16 \times 26 \text{ m}^3$ with a total weight of about 10,000 t. Its central barrel part is located inside the large octagonal shaped L3 solenoid magnet that operates at 0.5 T field strength with a rated current of 30 kA. It covers the pseudo-

¹Rapidity is defined as: $y = \frac{1}{2} \ln\left(\frac{E+p_zc}{E-p_zc}\right)$ (E: energy of the particle, p_z : momentum component along the beam axis). It is often replaced by the pseudo-rapidity: $\eta = -\ln \tan(\Theta/2)$ which matches the rapidity in the $m \rightarrow 0$ limit (Θ = angle from the beam direction)

3 A Large Ion Collider Experiment

rapidity region of $|\eta| \leq 0.9$ (polar angles: $45^\circ - 135^\circ$). Forward detectors providing interaction triggers and event characterization measure particles in the forward and backward region of $-3.4 \leq \eta \leq -1.7, 1.7 \leq \eta \leq 5.1$. This whole setup is followed by a muon spectrometer covering $-4.0 \leq \eta \leq -2.4$. ALICE with all its sub-detectors to be discussed in the following is illustrated in figure 3.1 [27].

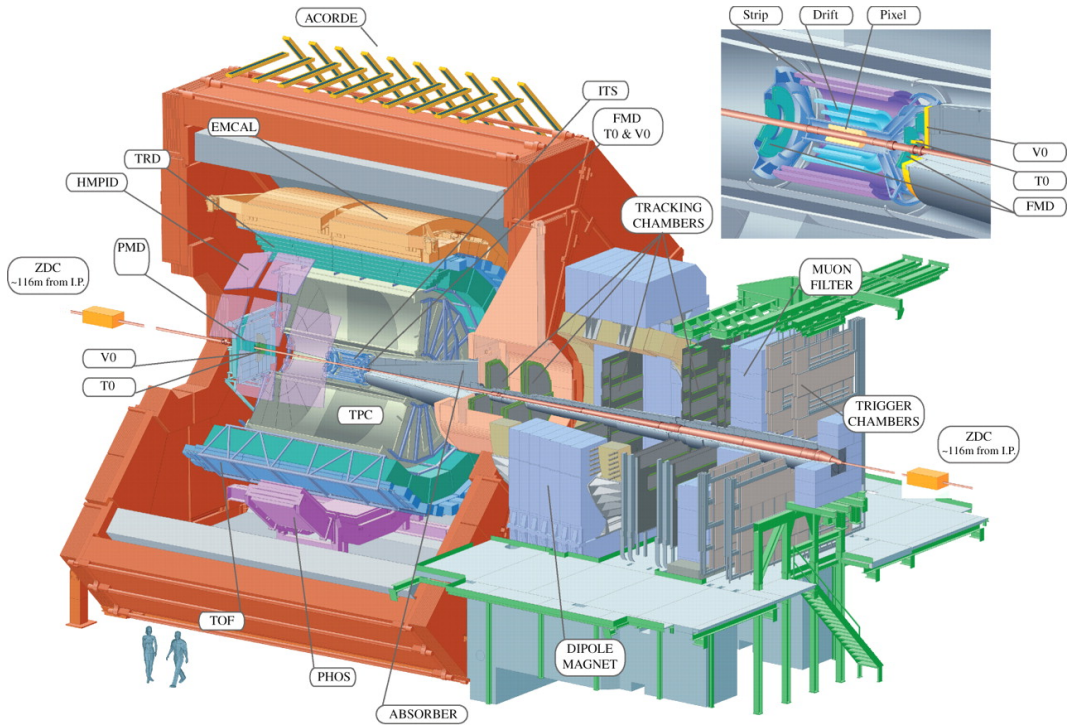


Figure 3.1: The ALICE detector with its main sub-detectors in the CERN/point 2 cavern.

Located inside the red L3 magnet - from the inside out: the Inner Tracking System (ITS; see close-up for details) consisting of two layers of high-resolution silicon pixel (SPD), drift (SDD), and strip (SSD) detectors, having the Forward Multiplicity Detector (FMD), V0 and T0 on its outsides, the Photon Multiplicity Detector (PMD), the cylindrical Time Projection Chamber (TPC), three particle identification arrays of Time Of Flight (TOF), Ring Imaging Cherenkov (HMPID) and Transition Radiation (TRD) detectors, and two electromagnetic calorimeters (PHOS and EMCal). The adjacent forward muon arm consists of absorbers, tracking and triggering chambers and a dipole magnet. An array of scintillators (ACORDE) can be found on top of the L3 [27].

- **The Inner Tracking System - ITS**

The ITS is the part of ALICE that is located closest to the collision point. It is mainly designed to collect data for the secondary vertex reconstruction of heavy flavor and strange particle decays. In addition, it is dedicated to finding and identifying particles with low momenta. Together with the information provided by the Time Projection Chamber its data contribute to the improvement of the momentum and angular resolution. The system consists of six silicon layers that are placed cylindrically around the beam pipe which determines the inner radius of the ITS (≈ 3 cm). The outer radius (≈ 50 cm) is adapted to the track detection with the TPC. The length of the ITS in beam direction is approx. 1 m resulting in an active area of about 7 m^2 [28]. Its detectors are the following:

- Silicon Pixel Detector - SPD

The SPD is the innermost of the ALICE detectors. It consists of two layers of SPD modules located around the beam-pipe at an average distances of 39 mm and 76 mm from the beam axis. It plays an important role in the determination of the position of the primary vertex as well as in the measurement of the impact parameter of secondary tracks originating from the weak decays of heavy flavor particles.

- Silicon Drift Detector - SDD

The two intermediate layers of the ITS are built by the SDD. Their main purpose is to provide dE/dx measurements needed for the ITS particle identification. In addition, they have a very good multitrack capability.

- Silicon Strip Detector - SSD

The two outer layers of the ITS are covered by the SSD. They position particle tracks in two dimensions which is crucial for the matching of the tracks from the TPC to the ITS. Additionally, they also give information about dE/dx to assist particle identification for low-momentum particles [26].

- **Particle Identification - PID**

There are several detectors in the central barrel of ALICE dedicated to identifying particles over a large phase space. They deal with the velocity and momentum of the particles, their invariant mass and also the decay topology. Namely they are:

- The Time Projection Chamber - TPC

The main tracking detector in the central barrel is the TPC. It has the shape of a hollow cylinder with an inner radius of 0.85 m, an outer radius of 2.5 m and a length of 5 m. It is made of a field cage providing a homogenous field along the z-axis filled with 88 m³ of a Ne-CO₂ (90-10) gas mixture at atmospheric pressure. In its axial center lies a high voltage electrode parallel to the end-caps creating two drift regions of 2.5 m each. It is charged to 100 kV providing a drift field of 400 V/cm. Charged particles ionize the gas atoms whose electrons drift to the two end caps in 94 μ s (at normal temperature and pressure) where they are detected by 72 multi-wire proportional chambers (MWPC) with a total of 557568 read-out channels. Even though it is rather slow and produces a high amount of data the TPC has been chosen due to the need for efficient and robust tracking (efficiency larger than 90 %) since it can cope with the highest conceivable charged particle multiplicities predicted [29]. In addition to tracking, the TPC acts as a detector for particle identification, namely it provides information on the flavor composition of the fireball and on its space-time extent at the freeze out. Together with the information provided by the TRD and the ITS it will be used to study for example charm, beauty and vector meson resonances through the measurement of leptonic observables reaching a p_t resolution better than 2.5% for electrons with $p_t \approx 4$ GeV/ c and an energy loss resolution better than 10%. Furthermore, it provides two-track separation with a relative momentum resolution below 5 MeV/ c in the region $p_t < 10$ GeV/ c and a pseudo-rapidity interval of at least $|\eta| \leq 0.9$ [27].

– The Transition Radiation Detector - TRD

The TRD is equally used for tracking in the central region of ALICE improving the p_t resolution at high momenta ($> 1 \text{ GeV}/c$). In addition, it provides a fast trigger for events with high- p_t charged particles. The TRD avails itself of the transition radiation (TR) from electrons with momenta of $1 \text{ GeV}/c \lesssim p_t \lesssim 280$. Since pions are much heavier than electrons, they do not create TR at these momenta and can therefore be separated from the electrons. Together with the specific energy loss in a suitable gas mixture the required pion rejection capability for a clean electron identification can be achieved. The TRD consists of 522 detector modules within 18 supermodules. Each module is built of a radiator to create the TR, a drift chamber, and the read-out electronics having 144 read-out channels in radial direction and either 12 or 16 in the direction of the beam axis. The complete TRD has an active area of approximately 675 m^2 which is divided into approx. 1.16 million read-out channels. The drift chambers are filled with a Xe-CO₂ mixture (85-15), whose gas atoms are being ionized by traversing charged particles. The freed electrons then drift through the 3 cm drift region ($v_d \approx 1.5 \text{ cm}/\mu\text{s} \Rightarrow t_d \approx 2 \mu\text{s}$), are being amplified at its end and the induced electrical signal on the cathode surfaces is read out [26]. The TRD will be discussed in detail in chapter 4.

– Time Of Flight - TOF

The Time Of Flight detector is optimized for the identification of particles with intermediate momenta: below $2.5 \text{ GeV}/c$ for pions and kaons, up to $4 \text{ GeV}/c$ for protons. It covers polar angles between 45° and 135° , i.e. an area of 160 m^2 , in the central barrel, surrounding the TRD. It consists of 18 supermodules with 160,000 individual cells (read-out channels) at a radius close to 4 m. It is an array of Multigap Resistive Plate Chambers providing a time resolution of $\leq 100 \text{ ps}$ [30]. Its time measurement in conjunction with the momentum and track length information from the tracking detectors is used to calculate particle masses. The particle

3 A Large Ion Collider Experiment

identification provided by the TOF detector is crucial for reconstructing open heavy flavor or vector-meson decays - such as as the ϕ meson [27].

– High Momentum Particle Identification - HMPID

The HMPID is enhancing the PID capability of ALICE beyond the momentum range covered by the energy loss measurements with the ITS, TPC and TOF. As the name implies it is dedicated to identifying high-momentum particles which includes pions, kaons and protons with momenta of 1 - 5 GeV/c. The HMPID is a single-arm array of Ring Imaging Cherenkov (RICH) counters that consists of seven modules which are mounted in-between TOF and the L3 magnet accepting 5% of the central barrel phase space. To perform PID the velocity of the particles is calculated via the opening angle of the emitted Cherenkov photon. With this information and the known momentum their masses can be derived [31].

• Electromagnetic Calorimetry

Photons give information about the temperature of the system spanning the range from thermal emission to hard QCD processes. For their measurement special detectors are needed. In ALICE namely the PHOS and the EMCal are dedicated to this task.

– The PHOton Spectrometer - PHOS

PHOS is a small single-arm, high-resolution and high-granularity electromagnetic calorimeter designed for detecting photons and neutral mesons. It consists of five modules and is located at the bottom of the ALICE detector, 4.6 m from the vertex, covering a pseudo-rapidity range of $|\eta| < 0.12$ and azimuthal angle of $\Delta\phi = 100^\circ$. Its main requirements are to provide information about the initial phase of a heavy-ion collision regarding its thermal and dynamical properties making use of low- p_t direct photons and to give more insight into jet-quenching as a probe of deconfinement studied via the measurement of high- p_t π_0 -mesons and gamma-jet correlations [26].

- The ElectroMagnetic Calorimeter - EMCal

The second electromagnetic calorimeter is the EMCal, a Pb-scintillator sampling calorimeter with longitudinal wavelength-shifting fibers, read-out via avalanche photo diodes covering a geometrical acceptance of $|\eta| < 0.7$ and $\Delta\phi = 107^\circ$. It is optimized for the measurement of jet production rates and fragmentation functions in conjunction with the charged particle tracking of the other central detectors. It measures the energy of photons and electrons with transverse momenta up to 100 GeV/c and additionally provides a fast trigger on the L1 level (explained in chapter 8) for photons, electrons and jets [27].

- **Muon Spectrometer**

The dimuon forward spectrometer is optimized for the detection of heavy quark decay products from J/Ψ , Ψ' (charmonium states), Υ , Υ' and Υ'' (bottomonium states). Its mass resolution is sufficient to separate all mass-states via their decays in the $\mu^+\mu^-$ -channel. Its acceptance covers the pseudo-rapidity region of $-4 \leq \eta \leq -2.5$ and the resonances can be detected down to zero transverse momentum. Located after the L3 magnet, the spectrometer consists of a front absorber to suppress all particles except muons, a tracking system (MCH) made of 10 cathode pad/strip chambers, a trigger system (MTR) designed to select events with, e.g. heavy quark resonance decay candidates, and a dipole magnet positioned at about 7 m from the interaction point. A schema of the spectrometer can be seen in figure 3.2.

- **Main Trigger and Forward Detectors**

For event selection and measurement of global reaction features ALICE has a number of small and specialized detector systems [30]. Namely they are:

- V0

The V0 detector is consistent of two arrays (V0A and V0C) of segmented scintillator counters. With its ability to provide minimum bias and further centrality triggers the V0 is one of the detectors giving input to the TRD pre-trigger system (\rightarrow chapter 8). In addition, it contributes

3 A Large Ion Collider Experiment

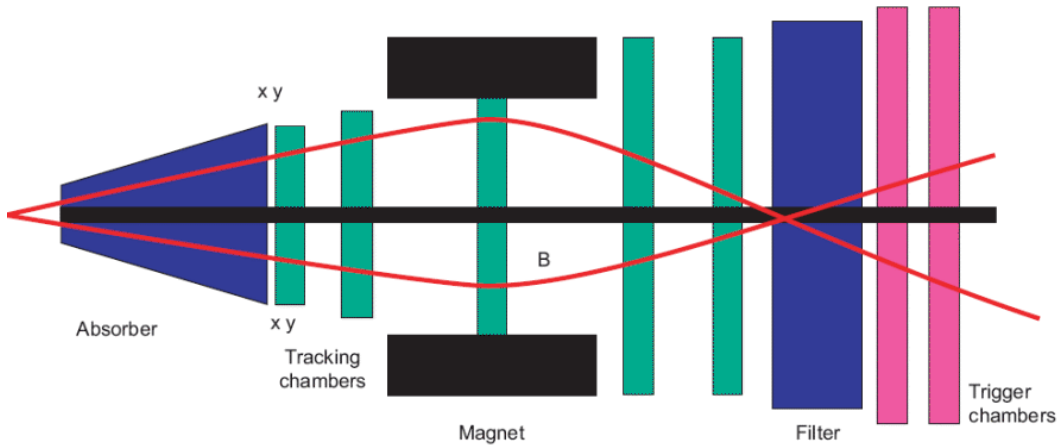


Figure 3.2: The basic principle of the forward muon spectrometer is shown: an absorber to filter everything but the muons, a set of tracking chambers before, inside and after the magnet and a set of trigger chambers [27].

to luminosity measurements, providing a precision of about 10% in p-p collisions.

- T0

Two sets of 12 Cherenkov counters (fine mesh photomultipliers with fused silicon radiator) are built around the beam pipe creating the T0 detector. It measures the event time with very good precision of < 25 ps. Furthermore, it generates an L0 trigger (see chapter 8 for details) and a start time for the TOF detector, it can measure the vertex position with a precision of ± 15 mm and is capable of providing a contribution to the pre-trigger prior to L0 [26].

- A COsmic Ray DETector for ALICE - ACORDE

ACORDE is located on top of the L3 magnet triggering on cosmic rays for calibration and alignment purposes as well as detecting single atmospheric muons and multi-muon events to study high energy cosmic rays. It is arranged as an array of 60 large plastic scintillator counters.

- Forward Multiplicity Detector - FMD

The FMD is the primary detector providing information about multiplicity distributions of charged particles over a wide kinematical range

- pseudo-rapidity coverage: $1.7 < |\eta| < 5.1$ corresponding to an angular interval of about 0.75° to 21° . It counts charged particles in rings of silicon strip detectors located at three different positions along the beam pipe. Additionally, its measurements are used to study the elliptic flow and multiplicity fluctuations.
- The Photon Multiplicity Detector - PMD
The PMD consists of two planes of gas proportional counters and is designed to measure the multiplicity and spatial distribution of photons event-by-event in the $2.3 < \eta < 3.7$ region.
- The Zero Degree Calorimeters - ZDC
The ZDCs - two sets of two compact calorimeters each - are located about 116 m from the interaction region in both directions along the beam line. They are designed to detect non-interacting nucleons (“spectators”). By measuring their energy carried in the forward direction the number of participant nucleons, which is the observable most directly related to the geometry of A-A collisions, can be estimated. One set of ZDCs detects spectator neutrons, the other one protons since they are spatially separated from each other by the LHC beam line [27].

4 Transition Radiation Detector

As this thesis' work is dedicated to the operation of the Transition Radiation Detector, a more detailed description of it is given in this chapter. The physics behind transition radiation is shortly explained, followed by a presentation of the detector layout, its main purpose and contribution to the ALICE experiment.

4.1 Transition Radiation

When charged particles traverse the boundary between two media with different dielectric constants ϵ_1 and ϵ_2 , there is the possibility that **transition radiation** (TR) is emitted. This can be pictured as follows: assuming the particle moves in vacuum (ϵ_1), a mirror charge is created due to polarization when it approaches another medium (ϵ_2). Charge and mirror charge form an electric dipole whose field strength changes with the particle getting closer to the boundary. This time dependent dipole field vanishes when the particle enters the second medium and causes a photon to be emitted, since the particle has to lose this energy difference. This mirror charge model is illustrated in figure 4.1 [32].

The total energy E_{tot} of this radiation is given by

$$E_{tot} = \frac{1}{3} \alpha \hbar \omega_p \gamma \quad (4.1)$$

$$\omega_p = \sqrt{\frac{4\pi\alpha Z N_e \rho}{A m_e}} \approx 28.8 \sqrt{\rho \frac{Z}{A}} \text{ eV} \quad (4.2)$$

ω_p : plasma frequency, α : fine-structure constant, Z : atomic number, N_e : number of electrons, ρ : density of the material, A : atomic weight, m_e : electron mass [33]. Equation 4.1 shows that it increases with the relativistic Lorentz-factor $\gamma = E/mc^2$

4 Transition Radiation Detector

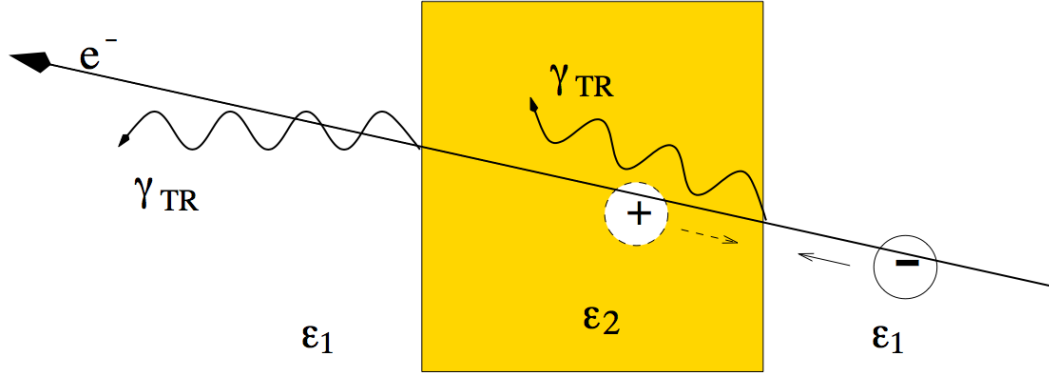


Figure 4.1: Illustration of the mirror charge model for the creation of **transition radiation**.

A charged particle produces a mirror charge when passing the boundary between two media of different dielectric constants ϵ_1 and ϵ_2 . These two opposing charges build an oscillating dipole which radiates a photon γ and the [32].

of the particle. Due to this dependency of the energy loss of the particle on γ , particles with large γ (high energy and low mass) such as electrons (positrons) give off more photons, than particles with a small γ (low energy and/or high mass) such as pions. For particles with $\gamma \gtrsim 1000$ the emission probability is non-eligible anymore which is given for electrons with momenta around and above 1 GeV/c. TR photons are emitted with a sharp maximum at a small angle $\Theta \propto 1/\gamma$ which means that they stay very close to the particle track. For ultrarelativistic particles ($\gamma \gg 1$) the typical energy of a TR photon lies in the keV region (\rightarrow X-ray) as can be calculated with

$$\langle \hbar\omega \rangle \approx \frac{1}{4} \hbar\omega_p \gamma. \quad (4.3)$$

The energy spectrum of TR photons absorbed in a Si detector is plotted in figure 4.2 which shows that the average photon energy E_γ is about 10 keV. Following equation 4.3 the number of photons emitted by an electron per boundary transition can be approximated as [34]

$$n_0 \approx \frac{E_{tot}}{\langle \hbar\omega \rangle} \approx \alpha \approx \frac{1}{137}. \quad (4.4)$$

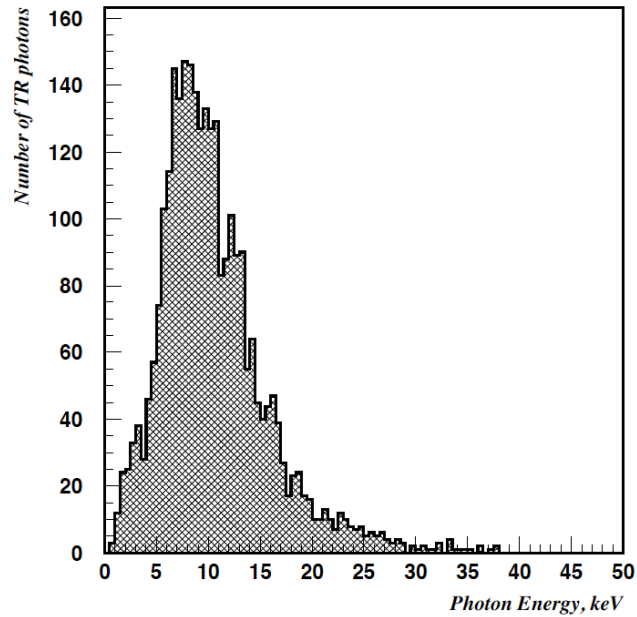


Figure 4.2: Spectrum of TR photons absorbed by a Si detector from electrons with $p = 30$ GeV/ c and an emission angle of $\Theta = 90^\circ$. The mean detected TR photon energy is $E_\gamma \approx 10$ keV [35].

4.2 Detectors

The effect of transition radiation can be used for particle identification at highly relativistic energies where Cherenkov radiation and ionization do not apply sufficiently anymore. In high momentum ranges, particularly electrons can be distinguished from other charged particles since their γ is greater than 1000 already for $p \approx 0.5$ GeV/ c , whereas, for example, a pion reaches this Lorentz-factor at $p \approx 100$ GeV/ c due to its higher mass ($\gamma = p/mv$).

The number of emitted photons per boundary transition is only of the order of $\alpha = 1/137$ as was shown in equation 4.4. Therefore, the **radiator** of a **Transition Radiation Detector** (TRD) where the TR is being created, should be consistent of a material with many boundaries, like a stack of a few 100 foils. However, interference effects in multi-layer radiators have to be considered, since they lead to a saturation of the X-ray yield for particles above certain Lorentz-factors. Taking both limitations into account (γ sufficiently high for TR production, yet below the

4 Transition Radiation Detector

saturation limit), more than one TR photon can be emitted for $\gamma \gtrsim 2000$ which is the case for an electron momentum of $p \approx 1 \text{ GeV}/c$. Since pions only reach this γ for $p \approx 280 \text{ GeV}/c$, this interval leads to the best electron identification results. Furthermore, the radiator material should have a very low atomic number Z to avoid the photon to be reabsorbed before leaving the radiator. This is due to the fact that the cross section σ of an interaction between a photon and a target atom is a function of Z and the photon energy. It can be approximated by $\sigma \propto Z^5 E_\gamma^{-3.5}$ (photoionization) [36]. Next to these physical, there are also geometrical and mechanical constraints to the choice of the radiator. Gravitation makes it almost impossible to guarantee the uniform separation of the foils, wherefore the use of regular stacks of foils is excluded. In addition, the radiator needs to support the entrance window (serving as the drift electrode) of the read-out chamber it is attached to.

The ALICE TRD

Following these requirements it has been decided to use a multi-layer as shown in figure 4.3 structure for the radiators of the ALICE TRD [37].

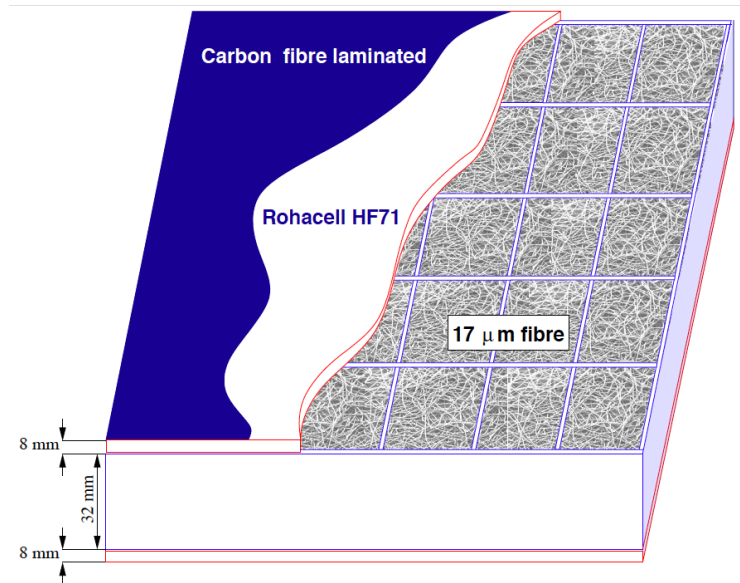


Figure 4.3: Design of the TRD radiator [38]. It consists of a 32 mm stack of polypropylene fibre mats enclosed by two 8 mm Rohacell[©] foam sheets surrounded by a lamination of 0.1 mm carbon fibre sheets.

This “sandwich” consists of 8 mm Rohacell[®] foam covered with 100 μm carbon fibre laminate and is filled with thin (17 μm), irregular polypropylene fibre mats. Sheets of aluminum-coated mylar foil cover the sandwich serving as a gas shield and electrode at the same time.

Since the energy of the TR photons lies in the X-ray region the detection device has to be sensitive for $3 \leq E_\gamma \leq 30$ keV. **Multi-wire proportional chambers** (MWPC) extended with a drift region serve this purpose suitably. It is favorable to fill these gaseous detectors with a gas of high atomic number Z to keep the absorption length as short as possible since the intensity of X-rays passing matter decreases exponentially with the distance covered. **Xenon** with $Z = 54$ has the best absorption efficiency with an absorption length of about 10 mm for typical TR energies around 10 keV which lead to the choice of a Xe-rich gas mixture for the ALICE TRD. In addition, materials with high Z have the highest specific ionization which is important for the detection of the initial charged particle. Entering the gas together with its associated photon, both particles ionize the gas creating electron-ion pairs. If an electric field is applied, the charged particles drift towards the electrodes (electrons to anode, ions to cathode). With a sufficiently high field the primary electrons are accelerated until at some point their energy is high enough to ionize the gas and produce secondary electron-ion pairs. This leads to an avalanche process and amplification of the initial charge. This amplification is known as the **gas gain**. The applied anode voltage is chosen such that the signal is proportional to the original number of electrons produced. A high maximum gas amplification factor ($5 \cdot 10^3 - 1 \cdot 10^4$) to match the noise level of the electronics is needed to improve the position resolution due to larger values of the signal-to-noise ratio (S/N). However, there are not only electron-ion pairs produced in the avalanche process but also UV photons from excited gas molecules (photoelectric effect). Some of these photons can be energetic enough to ionize the gas themselves and produce photo electrons resulting in another avalanche which then may cause a **break down** of the counting gas. Adding an organic “quencher” to the noble gas, avoids having this problem. The molecules of a quenching gas have a large number of rotational and vibrational modes to dissipate the excess energy by elastic collisions or dissociation. Usually,

4 Transition Radiation Detector

these quenchers are CH_4 , C_2H_6 , iC_4H_{10} or alcohol vapors. However, polymerization under irradiation can cause material aging, and flammable gases are not allowed in underground experiments, wherefore CO_2 - equally having the above described characteristics - is the gas of choice in environments such as the LHC. Since different gases have different electron mobilities μ [$\text{cm}^2 \text{V}^{-1} \text{s}^{-1}$], the quencher additionally plays an important role for the drift velocity $v_d = \mu E$ (E : electric field applied). All these requirements and limitations lead to the choice of CO_2 as a quencher for the TRD [37].

In general, an MWPC is a plane of proportional counters. It consists of a set of thin, parallel, equidistant anode wires, symmetrically sandwiched between two cathode planes. The anode wires have a positive potential with respect to the cathode planes to create the necessary electric field. The above described avalanche process happens near the anode wires producing a negative signal that can be measured. The positive ions from the avalanche process drifting towards the cathode are responsible for the actual signal: a mirror charge is induced on the cathode plane creating the signal to be readout. Dividing this plane into single read-out **pads**, helps to determine the location of where the avalanche process is created. A separation orthogonal to the anode wires leads to determination of the anode wire at which the avalanche occurred (z-coordinate) and the position along this wire (y-coordinate) as can be seen in figure 4.4 [37].

The electrode to the drift field, having a potential of about -2100 V, is provided by the aluminum-coated foil of the radiator. The drift chambers must be operated in the proportional region where the gain is known to be an exponential function of the voltage applied. The drift field is terminated after 3 cm ($E = 2100 \text{ V}/3 \text{ cm} = 700 \text{ V/cm}$) by a grounded plane of cathode wires. This plane separates the drift from the amplification region which is 2 x 3.5 mm long ending at the grounded cathode plane. In between the cathode wires and cathode pads (copper stripes) lies the anode wire grid with a potential of 1530 V, its distance from the cathodes chosen for best charge sharing between neighboring pads.

The read-out electronics is mounted on the back panel of each chamber. This back panel is a 20 mm honeycomb carbon-fibre sandwich supporting the pad planes [39].

A schematic of a TRD chamber can be seen in figure 4.5.

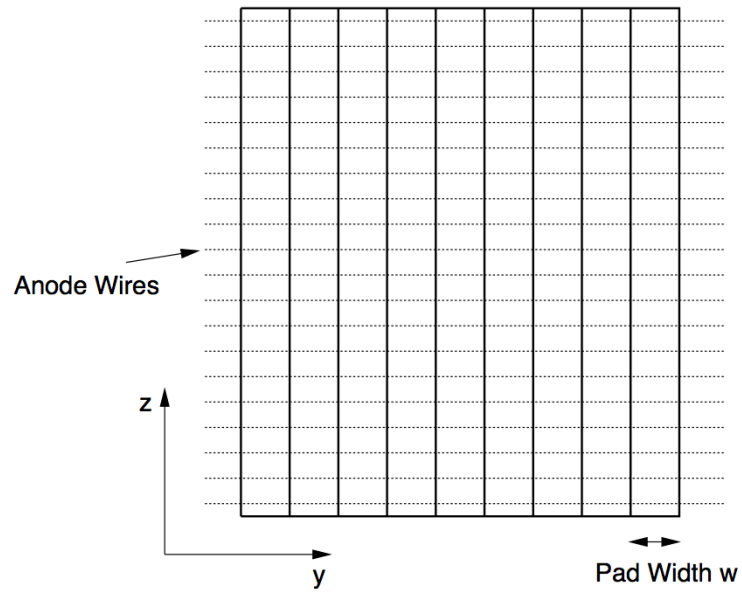


Figure 4.4: Pad geometry of an MWPC [37]. The cathode plane is divided into cathode pads, orientated orthogonal to the anode wires.

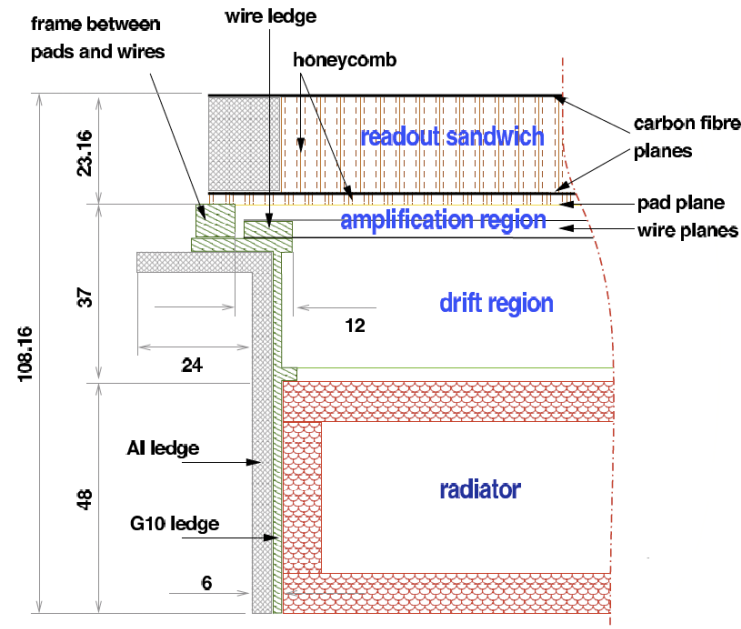


Figure 4.5: Schematic of a TRD read-out chamber [39]

4 Transition Radiation Detector

Each chamber has 96 - 128 **Multi Chip Modules** (MCM) of which one reads out the signals induced on 18 pads. A chamber has 144 pads in direction of the amplification wires ($r\phi$) and either 12 or 16 rows of these pads in z direction. The pads have a typical area of 6 cm^2 covering a total active area of about 675 m^2 with 1.16×10^6 read-out channels. The MCMs are grouped in six to eight **Read Out Boards** (ROB) per chamber and are controllable via a **Detector Control System** (DCS) board.

The fully assembled TRD will comprise 522 chambers within 18 supermodules. Three supermodules have only 24 instead of 30 chambers because the central stack is left out to minimize the amount of material in-front of the PHOS detector in order to lower the photon conversion rate [37]. At the time of this thesis, 13 supermodules with a total of 384 chambers are installed in the TRD setup. A schematic of the modular TRD design can be found in figure 4.6.

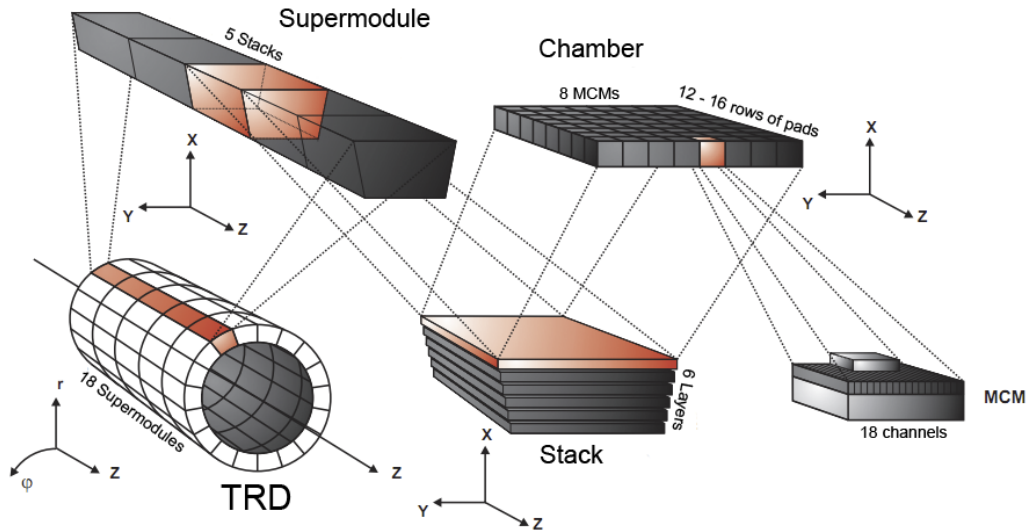


Figure 4.6: Modular design of the TRD. When fully assembled it will consist of 18 supermodules with five (SM 13, 14, 15 only four) stacks of six chambers each. This makes a total of 522 chambers for the entire TRD. Each chamber consists of 12 - 16 rows of pads each with 8 multi-chip modules (MCMs). Each MCM has 18 read-out channels making it a total of 1.16×10^6 .

Since pions in the momentum range of $1 \text{ GeV}/c \leq p \leq 280 \text{ GeV}/c$ do not create TR, the electron cluster at the beginning of the drift region is specific to electrons and therefore used to separate them from the pions. This is the first effect making it possible to distinguish between the signals of the two particles. Secondly, pions are heavier, wherefore their specific energy loss is smaller than for electrons with the same momentum. The average pulse height spectrum of electrons and pions with a momentum of $2 \text{ GeV}/c$ as a function of the drift time can be seen in figure 4.7 (test beam data).

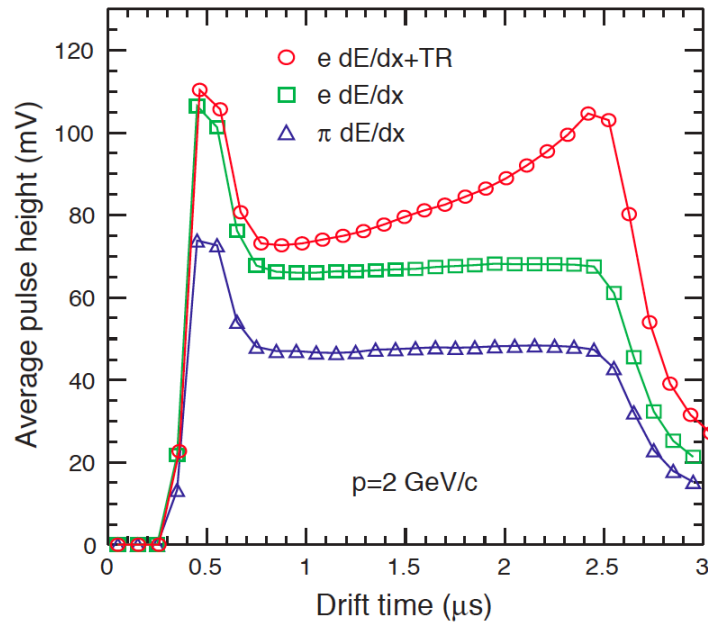


Figure 4.7: Spectrum of the average pulse height vs. drift time for pions (blue triangles), electrons (green squares) and electrons+TR photons (red circles) - test beam data. At later drift times there is a significant increase in the average pulse height for electrons, due to the preferential absorption of the TR near the entrance of the drift chamber [27].

One notices a first peak created by the initial particle track which comes from the electrons on both sides of the anode wire grid, followed by a plateau from when the electrons from the drift area reach the amplification region. The pulse height drops off afterwards when the clusters from the end of the drift volume have reached the anodes. For electrons there is a significant second peak, though, which is caused by

4 Transition Radiation Detector

the TR photons that are preferably absorbed at the entrance of the gas volume. The TRD is mainly designed to provide electron identification for momenta between 1 GeV/ c and 280 GeV/ c by using the amplitude and shape of this pulse height spectrum to separate e^- from pions. In addition, it is used as a trigger for high p_t electrons, charged particles and electron pairs due to its fast tracking ability. A third task is the enhancement of the momentum resolution of ALICE by providing additional points to the particle tracks reconstructed with the information from ITS and TPC. Since the TRD is surrounding the TPC, the effect of the magnetic field on the curvature of the particle trajectory is higher than inside the TPC. At the time of the design of the TRD the electron identification efficiency was anticipated to be $\epsilon_e \approx 90\%$ for momenta above 1 GeV/ c in central Pb-Pb collisions, having a pion efficiency ϵ_π better than 1%. This means that the pion rejection capability should be of the order of 100 - not more than one in 100 pions misidentified as an electron. These high requirements have to be met in order to be able to access the light vector mesons (ρ, ω, ϕ) as well as the high-mass part of the dilepton continuum and jets [26]. Based on recently recorded data, the electron efficiency was indeed found to be above 90% for $p_t > 3$ GeV/ c [40]. Another demand on the TRD is to provide a high position and momentum resolution ($\sigma_y \lesssim 400 \mu\text{m}$, $\sigma_\phi \lesssim 1^\circ$ and $\delta p_t/p_t \approx 2.5 - 3\%$) to match to the TPC even at highest track densities but still have a very low material budget in order not to disturb the measurements through absorption or multiple scattering [26]. These resolutions are dependent on the signal-to-noise ratio and measurements have shown that the TRD meets these requirements at a ratio of about 40 [41].

5 The TRD Gas System

In this chapter the TRD gas system is explained, giving a general overview, introducing its main modules, their purpose, layout and functionality, as well as describing the high demands that are made on the system. The work of this thesis was dedicated to the surveillance, control, maintenance, operation, improvement and further development of the system as will be discussed afterwards.

5.1 Overview

The total gas volume of the TRD when fully equipped (18 supermodules, 522 chambers) amounts to 26.1 m^3 plus an additional 2.5 m^3 in the storage buffers and piping, filled with Xe-CO₂, the gas mixture that best meets the physics requirements as described in chapter 4. This gas has to be mixed, stored, distributed and circulated through the TRD which is ensured by the TRD **gas system**. It is a sophisticated setup of many different modules, such as:

- Mixer module
- Distribution module
- Pump module
- Exhaust module
- Analysis module
- Purifier module
- Membrane module

5 The TRD Gas System

- Recovery module.

Figure 5.1 shows the locations of the main modules of the TRD gas system on the ALICE site at CERN/point 2. They will be explained in the following sections.

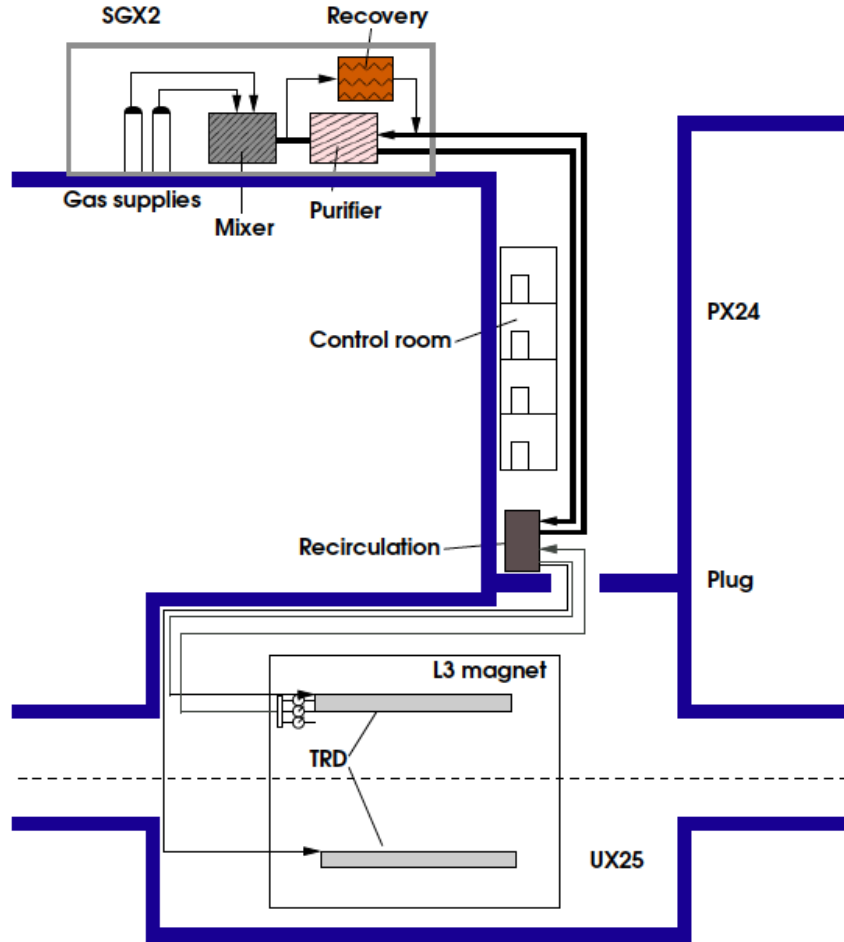


Figure 5.1: Schematic of the TRD gas system. From the mixer unit on the surface the Xe-CO₂ mixture is sent to the plug just above the ALICE cavern to be distributed into the 18 TRD supermodules. With the help of the pump module (equally in the plug) the return gas from the detector is compressed and pumped back to the surface gas building where it is recycled with the help of the purifiers. The loop pressure regulation is performed by acting on the suction speed of the compressor; this reaction mechanism is driven by the pressure sensor located at the detector [37].

There are different running modes for procedures like purging, filling, running, recuperation etc., which the gas system can be operated in. The operational requirements are defined by the needs of the detector. Before adding new supermodules to the common gas loop, after having installed them in the TRD setup, they have to be purged with CO₂ to remove all traces of air that had entered during transportation and storage. For this operation already integrated supermodules are disconnected from the gas loop and the system is put into “**purge mode**” to insert CO₂ at a high flow while venting out the excess gas. Once roughly five SM volumes (one volume $\approx 1.5 \text{ m}^3$) have been flushed through, the procedure is stopped and the next step taken: The system is put into a closed loop operation where no more gas is vented out and the “**fill mode**” is applied. Its purpose is to inject xenon at a high flow. While the Xe flushes in, excess CO₂ is removed with the help of the membrane module (as will be explained in chapter 5.4). To fine-tune the gas mixture after the previous two operations or, in general, when an exact amount of gas needs to be added to readjust the percentages of the gas components, the system can be run in “**direct mode**”. As soon as the intended mixture is obtained, the system is put into “**run mode**”, where the gas is circulated in a closed loop and fresh gas only added to compensate for leaks. The closed loop operation is mandatory in order not to waste any high-cost xenon.

Another crucial factor to be taken into account when operating the gas system is the light construction of the TRD modules having the aim of narrowing down multiple electron scattering and photon absorption in the material. This mechanical limitation dictates the maximum differential pressure in the TRD chambers to be lower than 2 mbar. Additionally, electrostatic distortions due to deformation of the enclosing drift and pad electrodes need to be avoided which limits the operational pressure even further down to 1 mbar above atmospheric pressure and asks for a precise control of the pressure in the supermodules. However, overall uniformity of the pressure is complicated by xenon’s high density of 5.58 g/l: the weight of the gas induces a high hydrostatic pressure gradient of 2.5 mbar over the 7.36 m total height of the TRD which means $\Delta \approx 0.4 \text{ mbar}$ per vertical chamber (1200 mm) [37]. Therefore, a segmentation of the gas distribution into 14 individual circuits was

5 The TRD Gas System

necessary. The three highest (sectors 03, 04, 05) and the three lowest (sectors 12, 13, 14) supermodules lie (almost) on the same height level, hence they are grouped together. A schematic of the TRD in the $r\phi$ -plane showing the pressure regulation segmentation can be found in figure 5.2.

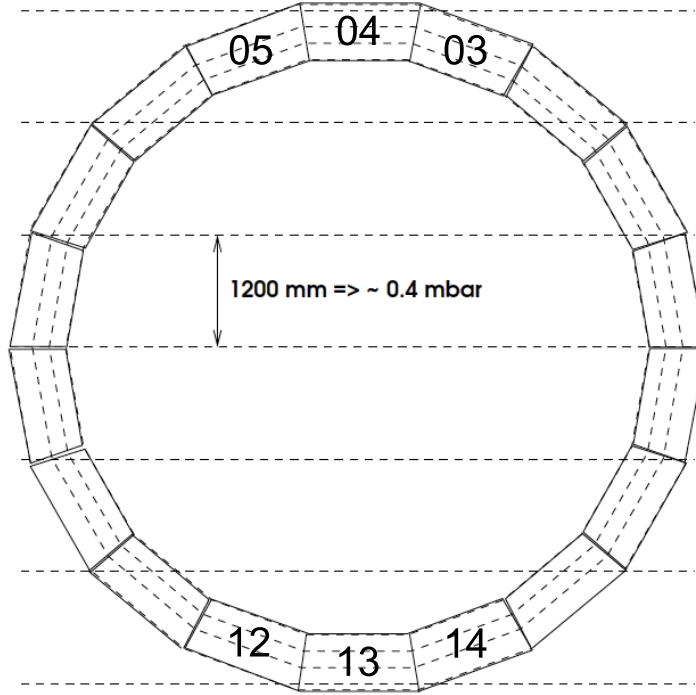


Figure 5.2: Pressure regulation segmented into 14 individually controllable sections [37]. Sectors 03, 04, 05 as well as 12, 13, 14 are grouped as one section each, since they basically lie on the same height level.

To realize a uniform flow over the 7.36 m avoiding at the same time the need for individual flow regulation a huge pressure drop (100 mbar) from the gas supply to the chambers is needed to make the hydrostatic differences of the sectors negligible. Following the Darcy-Weisbach equation [36]

$$\Delta p = f \cdot \frac{L}{D} \cdot \frac{\rho V^2}{2} \text{ [kg/ms}^2\text{]} \quad (5.1)$$

(f: dimensionless flow coefficient, L: pipe length, D: pipe diameter, ρ : density [kg/m³], V: mean flow velocity [m/s]) this goal is achieved with the help of 4 mm thin inlet lines of equal length. A SM has three inlet lines with one line serving a set of ten chambers (one layer back, one layer forth in the z direction). Each super-

module is equipped with a three-fold manifold that merges its three outlet lines into one 16 mm line. A pressure sensor is placed at the outlet of each sub-circuit where the regulation is done. The outlet lines of the 14 segments are brought together before a strong pump input in the supply plug where a second regulation step is performed. A detailed explanation of the modules and processes involved in serving the supermodules is given in chapter 5.2.

The afore described requirements make it unavoidable to observe and control the gas system continuously which is done with the help of the **Gas Control System** (GCS) developed by the CERN IT/CO group. It is based on Programmable Logic Controllers (PLC) allowing for actions like pressure and flow regulation, analog/pneumatic valve control, gas mixing, analysis, circulation etc. Furthermore, they can read analog/digital values, react to alarms and publish information to a user interface where the provided data is logged and the main operation of the gas system performed. With the help of configuration files, so-called recipes, specific for each module, information is loaded into the PLC for determination of set points, limits, regulation parameters etc [42]. The software making it possible for an operator to use the GCS is laid focus on in chapter 5.5.

The backup system

For ultimate protection of the detector in case of a system failure/malfunctioning of the pressure regulation, a backup system is installed. Each SM is equipped with a two-way safety **bubbler** connected to the supermodule's manifold as displayed in figure 5.3. If the differential pressure inside a SM becomes higher than 1.3 mbar compared to atmospheric pressure, excess gas will bubble out through the mineral oil (paraffine) the bubbler is filled with. If the pressure falls below atmospheric pressure, the oil will rise inside the bubbler. To prevent air from entering the system a permanent flow of N₂ circulates the system to an exhaust and passes by the outlet of the bubbler. If the pressure inside the SM falls below roughly -1.3 mbar, this N₂ instead of air will be sucked in. In addition to their safety purpose, one can use the bubblers as pressure monitors indicating the differential pressure inside the SM by the height level of the oil (1 cm \approx 1 mbar).

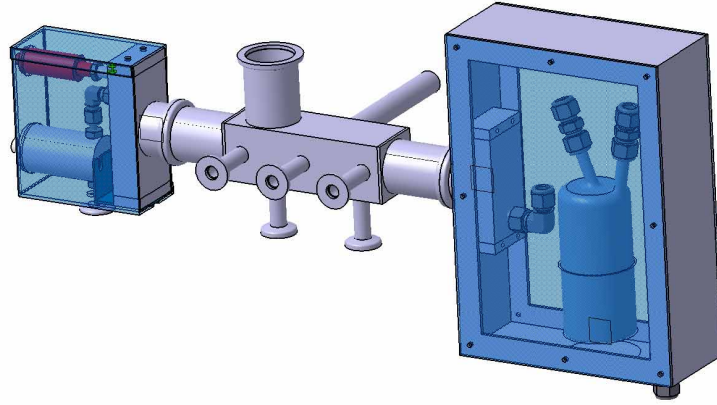


Figure 5.3: A TRD manifold (middle) with bubbler (right) and pressure sensor unit (left).

5.2 The Main Modules

As briefly introduced, the gas system comprises several modules for fulfilling different tasks such as mixing, distributing, circulating, analyzing, purifying and ensuring stable conditions within the detector. These modules can be operated as an ensemble following the commands of the mode the gas system is currently running in. Yet, it is also possible to control them individually, isolated from the other components. Explanations to the different modules are given in this section.

The mixing unit

Before circulating the gas through the TRD chambers, the gas system mixes the gas components (Xe and CO₂) in the appropriate proportions. These “primary” gases are stored in gas bottles located in a surface building. Each gas has a dual supply system to allow for an automatic switch-over to a second bottle when the first becomes empty.

The flow of the components is constantly monitored by a process flow control computer calculating the percentages entering the system while mass-flow controllers

(MFC) ensure the right amount. The use of a high-cost gas component makes closed loop circulation mandatory. This means, that no gas is exhausted and the mixing unit only injects to compensate for leaks or when gas is extracted for cleaning purposes. The mixing unit can be operated in different running modes depending on the needs at hand.

- **Purge:** Putting the module into purge mode is necessary when, for example the detector gas needs to be replaced by a purge gas to clean the operational mixture or to add new supermodules to the system (as already described). If required, this process can be stopped automatically after a certain amount of gas has been injected.
- **Fill:** This mode is used to fill the detector with its operational gas mixture. The ratios between the primary gases are regulated by the mixing unit and the flow is rather high. This operation can equally be stopped automatically depending on the user's requirements.
- **Direct:** When gas is put into the system in "direct" mode, the ratios are not controlled but the injection flows are set to a constant value.
- **Run:** When the gas system is in "run", the mixing unit only reacts and injects gas to compensate for losses through leaks. The system assumes that the present mixture in the detector is good and only regulates the ratio of the additional gas.
- **Stop:** When stopped, the mixer is in a stable state without any gas flow [43].

Figure 5.4 shows the schematic of a mixing unit as used for the TRD gas system.

The distribution module

The mixer sends the input gas to the so-called distribution module which comprises 14 racks to supply the individual circuits described before. It can be operated either as an ensemble or the racks individually. Each rack is split further into three input channels per connected sector serving the three inlet lines. The flow into the channels is adjusted with the help of input Pressure Control Valves (PCV) or "pressure regulators" which are self-contained valves with pressure controlling/regulating/reducing

5 The TRD Gas System

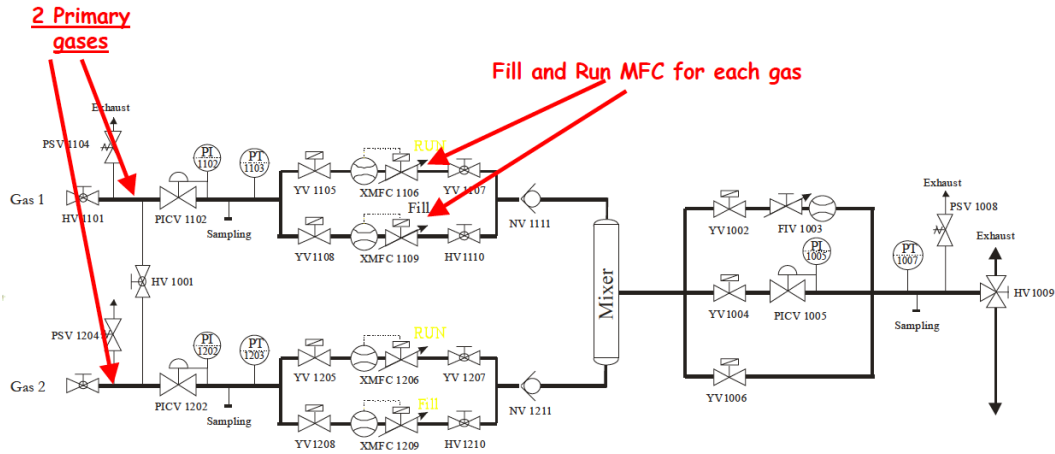


Figure 5.4: Schematic of the mixer module in the TRD gas system. The amount of the two primary gases (Xe-CO₂) is regulated through Mass Flow Controllers (MFC). Each gas type has two MFCs: one for the purge/fill/direct and one for the run mode.

possibility. A PCV automatically cuts off the gas flow at a certain (manually set) outlet pressure, ensuring stable (and safe) flows into the supermodules despite the different pressures on its input side.

The main components of a PCV are a pressure regulating element (valve), a loading element (spring connected to the valve) and a screw to manually set the spring force. In general, the spring holds the valve open. However, when the outlet pressure overcomes the spring setting, the valve starts to close. The pressure on the output side acts on one side of a membrane that is mechanically connected to the valve, “transmitting” the outlet pressure to the area underneath the spring which is located on the other side of the membrane. The more the pressure on the output side increases, the more the valve is closed. I.e., if the load flow decreases, the regulator flow must decrease also or if the load flow increases, the regulator flow must increase in order to keep the controlled pressure from decreasing due to a shortage of gas in the pressure system. An example of a PCV can be found in figure 5.5. The pressure regulation within a SM is done for each circuit individually on its outlet line where the channels are brought back together. Further downstream, all 14 output lines from the sectors are collected into one line leaving the experimental area to be

recirculated [43].

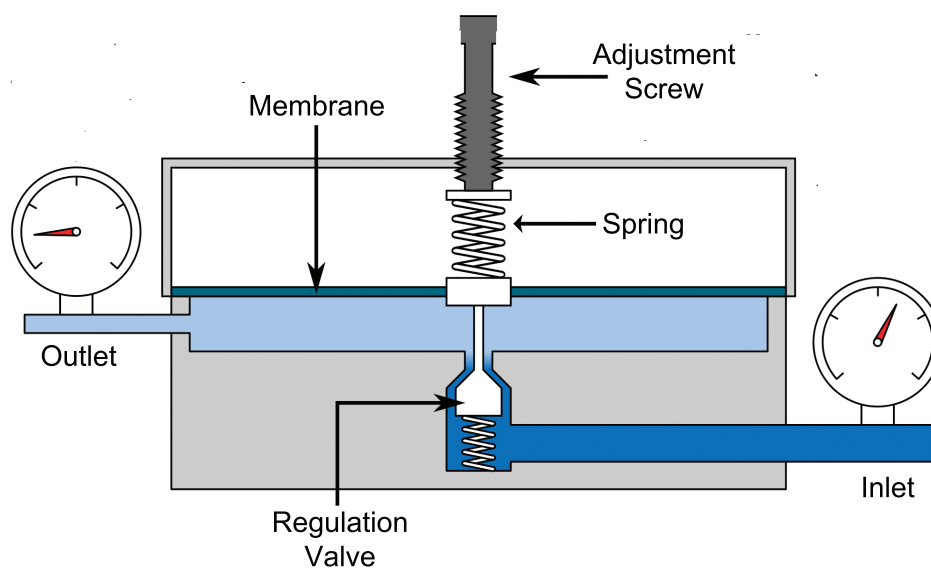


Figure 5.5: Principle of a pressure control valve [36] similar to the ones used in the TRD gas system. The spring keeps the valve open until the outlet pressure overcomes its setting which is when the valve begins to close to keep the output pressure constant.

The distribution module can be operated in three different option modes:

- Run: This mode brings the module into its nominal state, distributing the mixture into the channels with controlled pressure regulation for all the racks that are put into “auto”, and allowing any excluded racks to still be operated manually.
- Common purge: The purpose of this mode is to globally purge all the racks that are set to “auto” via the main input.
- Individual purge: A rack can be purged individually while the others are kept in normal running mode.

The pump module

With the help of the pump module consisting of two strong compressors the return gas from the detector is compressed above atmospheric pressure and pumped back to the surface gas building. It can be found in three different states:

5 The TRD Gas System

- Stop: If the pump is in this state, no gas is circulated; it is fail safe.
- Starting: When the pump is starting, the pressure is stabilized by regulating around the nominal pressure set point.
- Run: In “run” the gas is circulated and the pressure regulated around the nominal value set by the operator.

The exhaust module

In the case of the TRD gas system which usually runs in a closed loop, the name “exhaust module” is rather misleading, since no gas is vented out (in nominal running mode). This module mainly is a high-pressure buffer (located after the pump module) filled with about 1 m^3 gas at approx. 1 bar “overpressure” compared to atmospheric pressure that assures stable conditions within the detector modules. It delivers gas to (or accepts from) the detector in case of an increase (decrease) of the atmospheric pressure when the *mixer* module is in “run” mode. The buffer’s pressure is regulated with the help of an MFC. Since it is a “slave” to the mixer’s running mode, no regulation is done when the mixer is stopped but the MFC is prevented from venting out any gas as it can when the mixer is set to “purging” [43].

Since the quality of the gas mixture is a crucial factor for the physics requirements of the TRD, special attention is given to its analysis in the following chapter. The influences of gas impurities on the detector performance are pointed out, demonstrating the need for an intense, continuous surveillance, followed by a description of the devices supporting this important task.

5.3 Analysis Of The Gas

Influence of impurities on the detector performance

Due to air leaks, air diffusion and outgassing by some of the detector’s assembly materials, impurities such as oxygen and water as well as argon and nitrogen build up in the detector during normal operation. This decreases the efficiency of the detector, necessitating the contamination levels to be monitored and controlled continuously.

5.3 Analysis Of The Gas

O₂ and H₂O are used as early indicators of leaks since both gases can be measured nonstop with the help of two devices directly connected to the circulation loop. Average values of these two contaminants indicating no leaks are: O₂ < 1 ppm and H₂O < 100 ppm. The elimination of these two components is very important since electron attachment to the molecules of these contaminants through capture mechanisms negatively affects the high operation efficiency of the TRD. Attachment on H₂O alone is insignificant, but already small amounts (several hundred ppm) can double the attachment coefficient on O₂ [44]. A mechanism to explain the process is the resonance capture or “Bloch-Bradbury mechanism”:



where I is either O₂ or H₂O and S the quencher CO₂¹. The magnitude of attachment depends on the amount and type of the quencher in the operational gas mixture as well as on the lifetime of the excited state. Thus, the number of electrons that can be measured with the TRD and therefore the corresponding pulse height decreases exponentially as a function of the drift time t in case of attachment:

$$N(t) = N(0) \cdot e^{-A \cdot t} \quad (5.4)$$

where A is the attachment rate. Since the drift length in the TRD chambers is only 3 cm and the applied drift field high, the drift time is rather short, wherefore the attachment does not cause a severe reduction of the detector efficiency up to a few hundred ppm of O₂, as can be seen in figure 5.6 [44].

Another gas that has a huge effect on the detector performance is **SF₆** (sulphur hexafluoride). SF₆ is a very heavy gas with a high cross section for electron attachment even for low-energy electrons. While electron attachment to oxygen only causes a small signal loss even up to a few hundred ppm, a contamination with SF₆ on the ppb level can already decrease the pulse height by a large factor as is shown in figure 5.7.

¹In addition, the (vibrationally) excited state I^{-*} could decay by emitting an electron which would not lead to a signal loss.

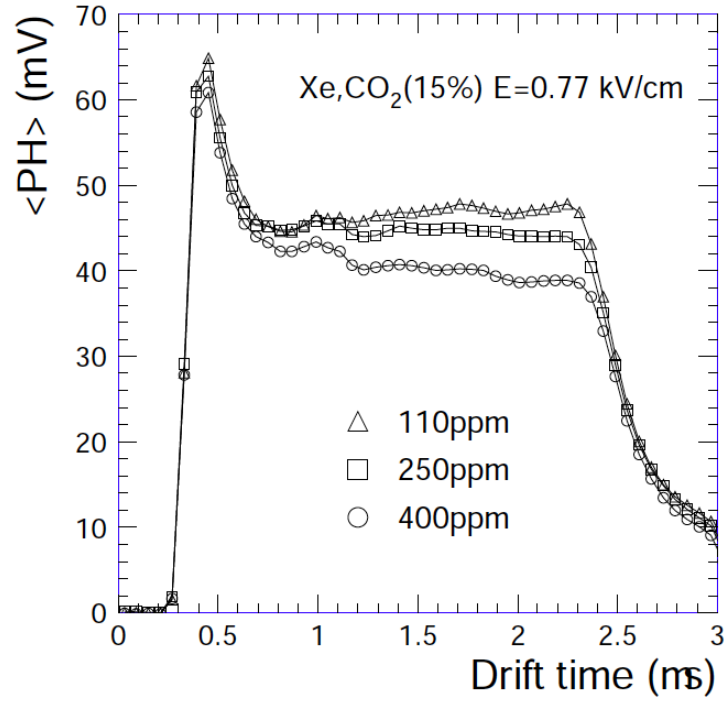


Figure 5.6: Pulse height spectrum for a drift field of 770 V/cm for different amounts of O_2 in the TRD operating gas [44].

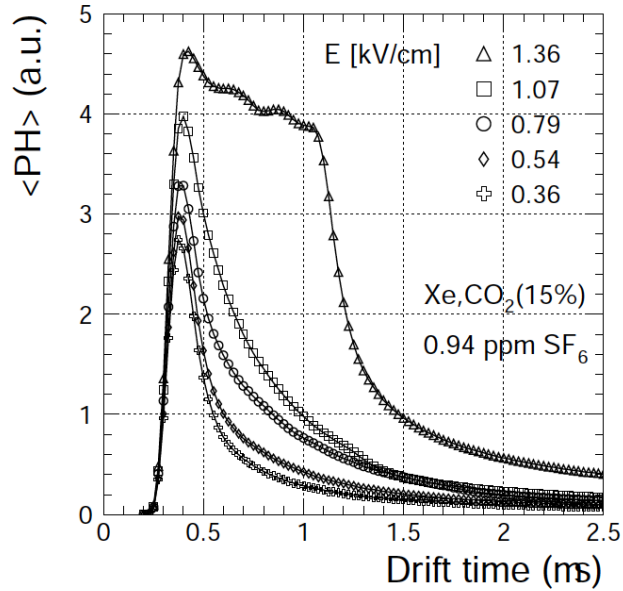


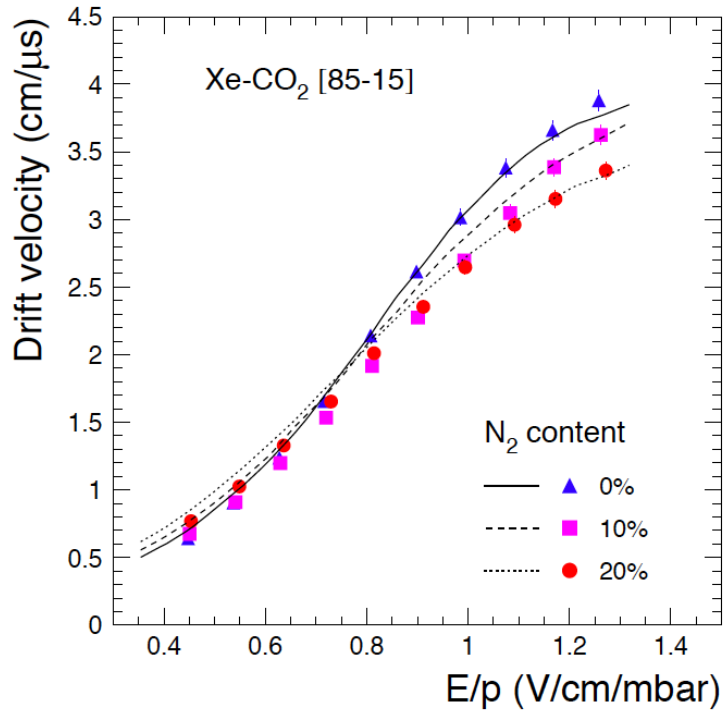
Figure 5.7: Pulse height spectrum for different drift voltages in the TRD operating gas with an SF_6 contamination of 0.94 ppm [44].

While the electron attachment was under investigation [44], SF₆ was found to be present in some xenon supplies which is why each new xenon bottle is now investigated carefully. Furthermore, the TOF detector uses SF₆ in its operating gas mixture, wherefore the air in the ALICE cavern has to be analyzed every so often, to make sure that no SF₆ is present which could enter the TRD through leaks.

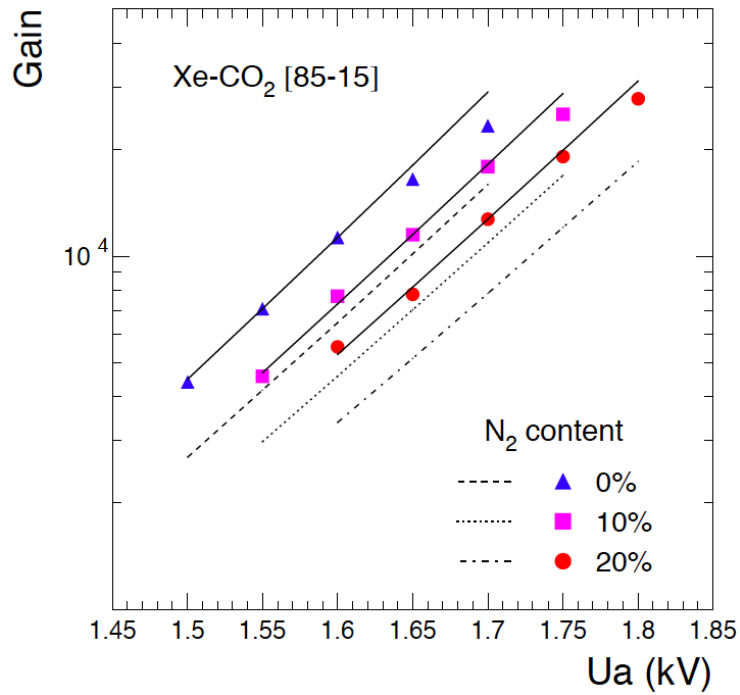
Earlier studies [45] have revealed that **nitrogen** in the TRDs operating gas mixture has an influence on the drift velocity and gain and therefore the detector performance. N₂ entering the TRD through air leaks can not be removed easily from the gas and accumulates over the running period. Since the drift velocity tends to saturate at lower values with an increasing amount of N₂, an adjustment of the drift voltages becomes necessary to keep the drift velocity constant. Similar adjustments become mandatory for the anode voltages to keep the gas gain at its high level. The results for Xe-CO₂ [85-15] with N₂ pollutions up to 20% can be seen in figure 5.8. They have shown a tolerable dependence of v_{drift} and gain on the nitrogen concentration at intermediate fields < 800 V/cm. Under 20% the differences can be compensated for with the help of drift and anode voltage adaptations [46]. In order to adjust the voltages accordingly, it is mandatory to monitor the N₂ amount constantly.

Impurities of **argon** in the operating gas mixture equally influence the detection qualities of the TRD since it has a higher absorption length than xenon for the typical TR photon energies in the range of 3 - 15 keV as can be seen in figure 5.9. This would lead to a lower interaction probability for transition radiation. Furthermore, it affects the electron identification due to its lower Fermi plateau² and therefore the less favorable ionization energy loss dE/dx compared to Xe.

²The Fermi plateau is a range of high energies, where the energy loss of a particle traversing a medium no longer increases with increasing particle energy. Up to this plateau, the energy loss of a traversing particle increases logarithmically with its energy [36].



(a) v_{drift} in Xe-CO₂ with N₂ additions as a function of the drift field.



(b) Gain in Xe-CO₂ with N₂ additions as a function of the anode voltage

Figure 5.8: Simulated impacts of N₂ on the operation of the TRD regarding the drift velocity and gain. The results show that a few percent of N₂ in the mixture can be tolerated [46].

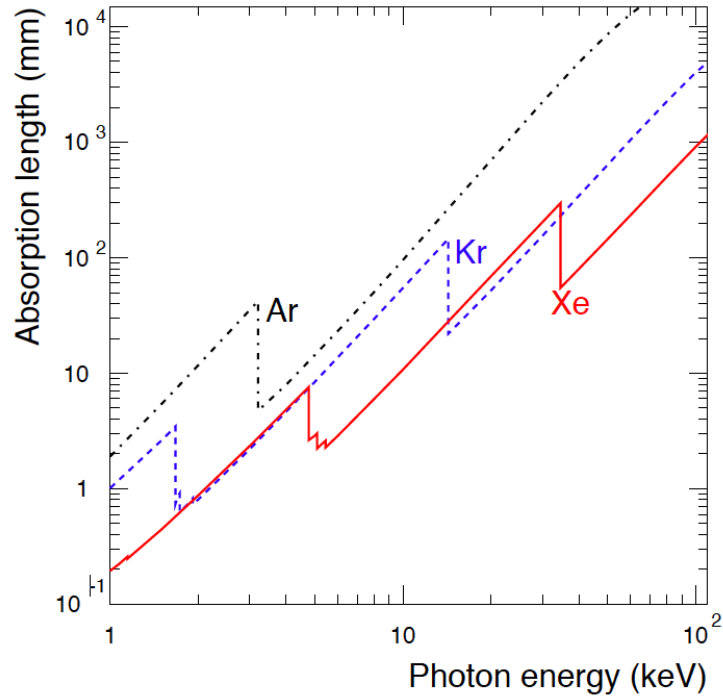
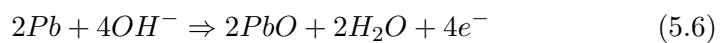
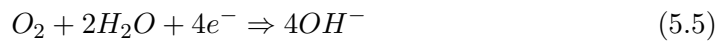


Figure 5.9: Absorption length as a function of the photon energy for argon, krypton and xenon [47].

Gas analysis devices and methods

- **Oxygen** is constantly measured using a **galvanic fuel cell** as can be seen in figure 5.10. It operates in a similar manner to a regular battery in which a voltage is produced from an electrochemical reaction. In the case of the O_2 analyzer, however, the reaction is regulated by the presence of oxygen. A sensor produces a voltage signal relative to the oxygen concentration of the gas stream which happens as follows: A chemical reaction between the metallic cathode (gold-plated) and anode (lead) and the electrolyte occurs when the so-called fuel (potassium hydroxide) in the cell comes into contact with oxygen entering through the semi-permeable membrane at the cell's end. O_2 is reduced by electrons which are supplied by the simultaneous oxidation of the anode.



5 The TRD Gas System

The current of electrons produced is directly proportional to the concentration (partial pressure) of oxygen present.

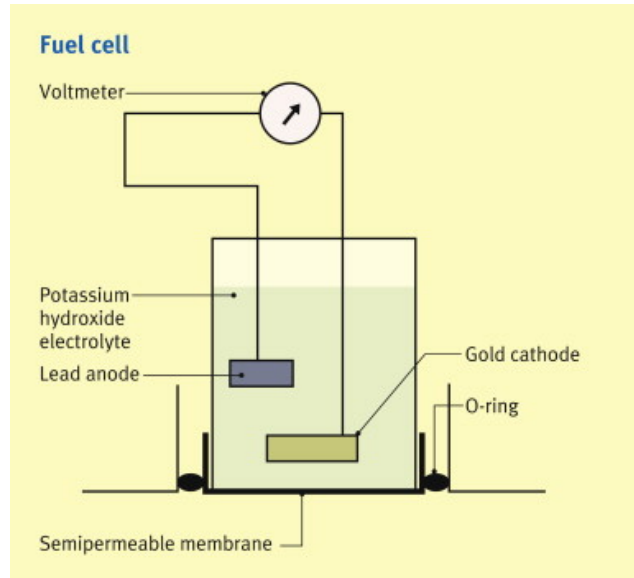


Figure 5.10: A galvanic fuel cell. The flow of electrons from anode to cathode via the external circuit results in a measurable current proportional to the partial pressure of oxygen [48].

- **Water** is kept under surveillance with the help of an **aluminum oxide moisture sensor**. It has two metal layers that form the electrodes of a capacitor. Basically, an aluminum probe is chemically treated to form a thin porous coating of aluminum oxide which is then coated with a layer of gold that is conductive and permeable to moisture. These two layers form anode and cathode (see figure 5.11 for reference). The water molecules adsorbed in the pores cause a change in the dielectric constant of the sensor and their amount is directly proportional to the moisture content of the gas stream. Furthermore, this absorption changes the capacitance of the sensor which can then be measured and converted to the moisture value [49].
- **CO₂** is monitored with a **Thermal Conductivity Detector (TCD)** in order to maintain the right ratio of Xe-CO₂. The TCD measures the thermal conductivity of the binary gas mixture and compares it to the value of pure CO₂ which the device was calibrated with. The produced 4 - 20 mA signal is

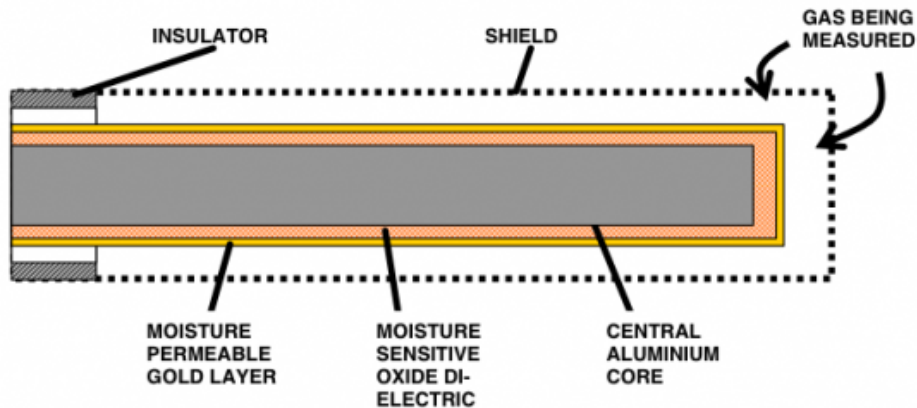


Figure 5.11: Principle of an aluminum oxide sensor with a gold layer and aluminum probe forming the anode and cathode [49]

proportional to the concentration of CO_2 in the TRD gas. Each TRD super-module is analyzed individually. In order to do so each electric valve opens for a few minutes to let gas into the analysis loop while the other loops stay closed. This gas sample is analyzed and sent back into the TRD circulation loop before the next valve opens. Controlling and monitoring of all the processes can be performed remotely through the GCS UI. Another helpful tool to keep track of the gas composition is the drift velocity and gain monitor “GOOFIE” which will be discussed in detail in chapter 6. All three detectors and the GOOFIE are installed in the same analysis module connected to the TRD circulation loop which makes a constant observation possible.

- The most common device used to analyze a gas with respect to all its components is a **gas chromatograph** (GC). It can separate the different constituents, given that they are gaseous or can be vaporized without decomposition (boiling point up to 400°), which can then be detected with an appropriate detecting device. Generally in gas chromatography there are so-called mobile and stationary phases. The mobile phase is a carrier gas such as helium that is sent through a wound curved capillary tube (“column”). This column is made of quartz glass lined with a defined stationary phase (often viscous polyorganosiloxanes) and housed in a temperature controlled oven. The carrier gas transports the inserted sample substance, its components staying in the

5 The TRD Gas System

stationary phase of the column for a different amount of time, depending on the polarity and vapor pressure of the individual gas molecules. A detector then measures the time ("retention time") at the exit of the column which can be graphically displayed together with the amount of gas and compared to standard substances. The detector used is TCD. It consists of a thermostated metal block with two identically structured cells. The sample gas flows through one of these cells while the other (measuring) cell is permanently flushed by a pure gas that is used for comparison. Both cells contain a heating wire ("filament") which is heated to a higher temperature than the surrounding detector block, so that continuously heat goes from the heating wires through the surrounding gas to the detector block. This flow is dependent on the thermal conductivity and thus of the composition of the gas. Changes in the composition of the sample gas therefore cause temperature changes in the measuring cell and thus a change in electrical resistance in the heating wires. Since measuring and reference cell are connected to form a Wheatstone bridge circuit, the temperature differences of the heating wires can be measured and recorded as voltage difference. The recorded signal is proportional to the concentration of the sample. The outlet of the GC's separation column is connected to one of the measurement cells. As a reference gas, the carrier for the chromatographic separation is used and sent through the other measuring cell. Manual gas chromatographies are performed frequently, mainly to keep track of the nitrogen and argon contamination in the TRD gas but also as a reference measurement for the percentages of CO₂ and xenon [36].

To detect SF₆ contamination an **Electron Capture Detector** (ECD) is used since SF₆ has a high electron capture cross section. This device uses a radioactive β electron source (⁶³Ni) to measure the degree of electron capture. The simplified principle of operation of an ECD is as follows: the βe^- ionize the make-up gas (N₂ in our case). Thermal electrons are then collected at an electrode through application of an electrical field. The decrease of the detector current due to the removal of the thermal electrons by recombination within electro-capturing components of the gas gives a signal. The area under

the peak is proportional to the electrons captured. The ECD is one of the most sensitive gas chromatography detectors tracing components down to the ppb-level [36].

Due to the afore discussed influences of the gas impurities on the detector performance, the TRD needs purification of the operating gas mixture. For elimination of contaminants such as water and oxygen but also CO₂ this is easily possible by passing the gas flow through dedicated purifiers and semi-permeable membranes without having to stop the operation. Argon and nitrogen, on the other hand, are not as easy to remove and require a more sophisticated procedure (cryogenic distillation). All devices and methods involved in the cleaning of the TRD gas are described in the adjacent section.

5.4 Gas Purification

The Purifier Module - O₂ and H₂O removal

Oxygen and water can be filtered out directly within the gas loop by cartridges filled with activated copper. The principle of operation of these purifiers is as follows: The copper is oxidized by the oxygen molecules present in the gas stream, forming a copper oxide and thus removing the oxygen molecules from the gas flow:



A configuration of two purifiers in parallel lets the gas run through one purification cylinder while the second one regenerates and goes into stand-by mode afterwards. For regeneration the purifier cartridge is gradually heated to 200° while flushed with an Ar-H₂(7%) mixture (Noxal) which leads to the chemical reduction of copper oxide to copper:



A schematic of the purifier module used for the TRD can be found in figure 5.12.

5 The TRD Gas System

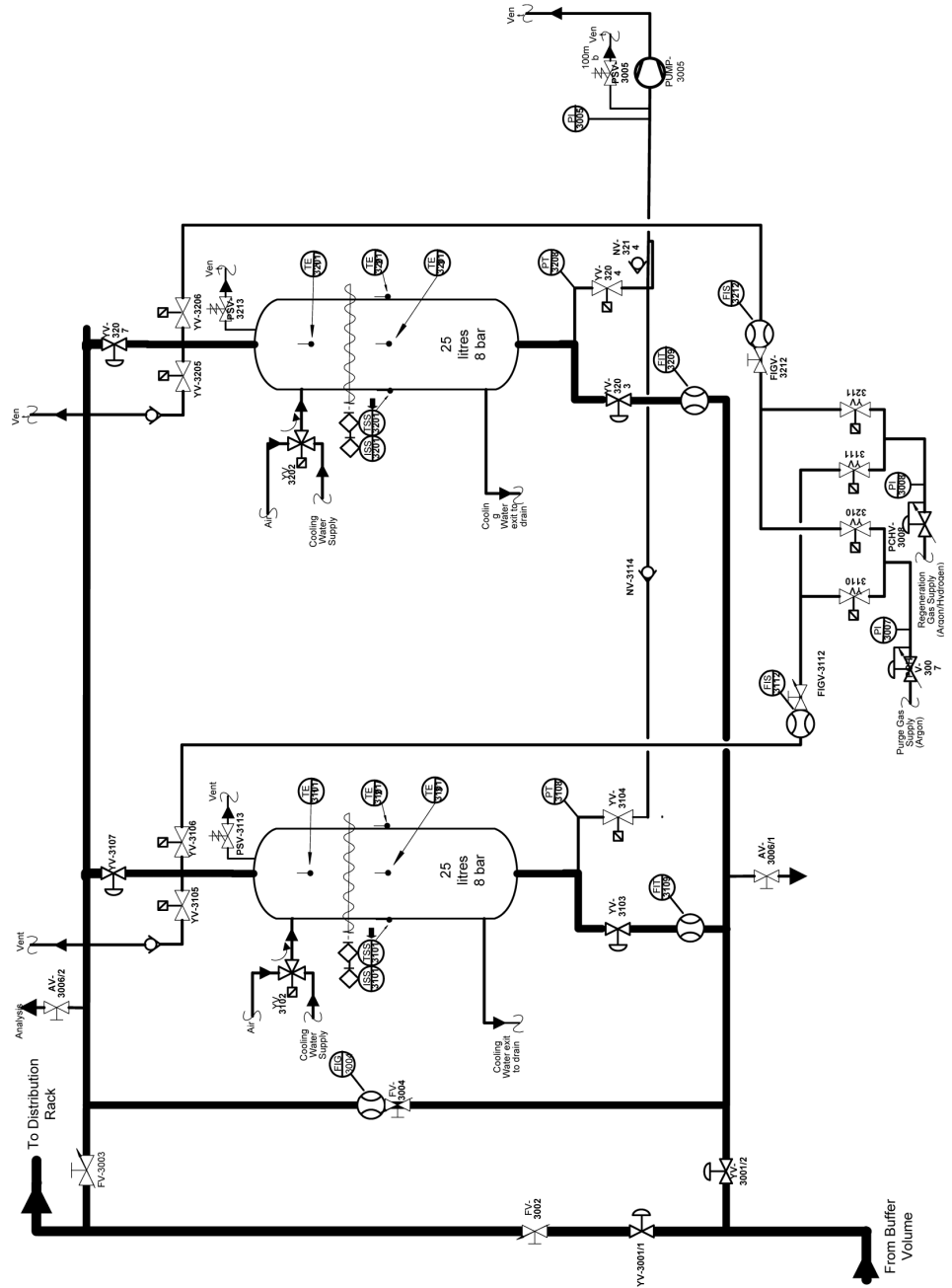


Figure 5.12: Twin column purifier module with inline regeneration [42].

The Membranes - CO₂ removal

Whenever new supermodules are inserted into the circulation loop of the TRD gas system, additional xenon is needed. Since the supermodules had been flushed with pure CO₂ to eliminate all traces of air that had entered during transportation and storage, this excess CO₂ has to be removed during the Xe filling process. For this purpose, semi-permeable membranes that can separate CO₂ from the rest of the gas are part of the gas system. They are also operated before the yearly cleaning via cryogenic distillation with a recovery plant (see next section) to remove impurities that could not be removed during the running period (N₂, argon). The membranes, as can be seen in figure 5.13, consist of bundles of capillary tubes of a porous material called polyamide [45].

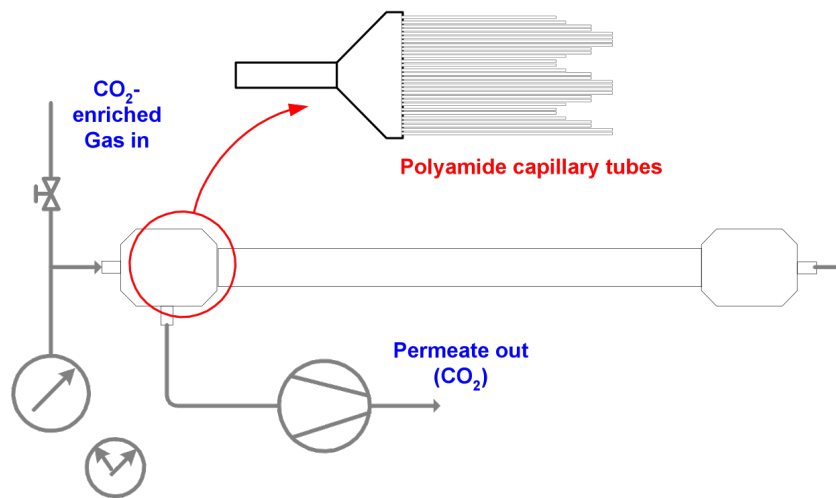


Figure 5.13: Schematic setup and principle of operation of membranes consisting of capillary tubes of polyamide.

They make use of the principle that certain gases permeate more rapidly than others, the rate determined by the size of the gas molecule, its solubility in the polyamide and the operating conditions of the separation. The gas mixture can therefore be separated into two streams of more and less permeable components. CO₂ is a rather fast gas (small molecule size) that permeates easier through the membrane than the slow (big) xenon molecules. For the TRD a system of two membranes in series (→ two stages) is used as can be seen in figure 5.14. This is to ensure that xenon

5 The TRD Gas System

that has permeated out with the CO₂ stream after one step of separation is not lost but can be recovered. Therefore, the permeate from the first stage is compressed and sent to the second membrane where the CO₂ is again separated from the permeated Xe and exhausted, while the xenon is circulated back into the system or sent to the recovery plant depending on the reason for the CO₂ removal.

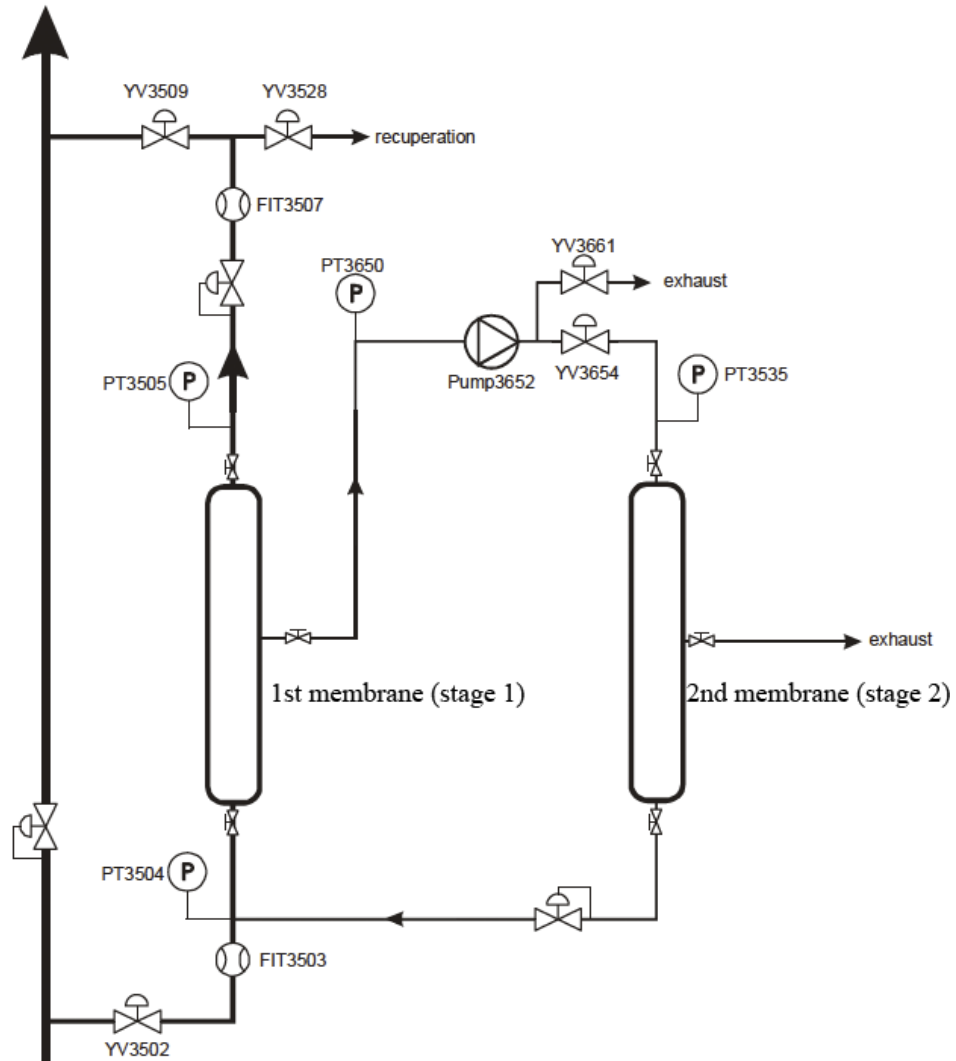


Figure 5.14: Schematic of the 2-stage membrane module used for CO₂ removal in the TRD [42].

The Cryogenic Plant - N₂ and Ar removal

As described before, oxygen and water entering the detector with air through small leaks or outgassed by some of the materials of the TRD are filtered out by the

purifiers and CO₂ can be separated from the gas with the membranes. Nitrogen and argon impurities on the other hand cannot be removed with these devices. Therefore the TRD gas circuit is equipped with a system to separate the precious xenon from the unwanted components Ar and N₂. The effect of especially the nitrogen (since argon enters to a lesser extent) on the detector performance determines the periodicity of applying the cleaning procedure. However, it is unavoidable to lose a certain amount of xenon during the operation, hence these two arguments have to be deliberated about carefully. Given that the cleaned xenon can be transferred into bottles to be then re-used as the primary supply, it is mandatory that its quality (purity) is as high as the original gas. For the TRD the cleaning and recuperation is carried out with the help of a **recovery plant** which regenerates the gas by **cryogenic distillation**. The principle relies on the fact that xenon has the highest freezing point of all the components in the mixture as shown in table 5.1. It freezes out already when the other components are still vaporous and can thus be removed by venting them out. Traces of CO₂ that might freeze together with the xenon are tolerable since it is part of the operating gas mixture.

gas	T _{freez} [C°]	T _{boil} [C°]
N ₂	-209.86	-195.79
Ar	-189.19	-185.7
Xe	-111.7	-108.12
CO ₂	-78	(subl.)

Table 5.1: Freezing and boiling points of the components contained in the TRD gas mixture.

The process of cryogenic distillation mainly consists of the following five steps: compression, cooling/distillation, pumping, heating, recirculation or recuperation of the xenon. The separation plant that is now used for the ALICE TRD had initially been built by Air Liquide in 1987 for the electromagnetic calorimeter of the ALEPH experiment [50]. A schematic of the device can be found in figure 5.15. The cooling system of this plant works with liquid nitrogen (LN₂) which makes it possible to cool down the injected gas to temperatures of about -170 C°. At temperatures this low, both the CO₂ and the xenon freeze out while the non-condensable gases - nitrogen

5 The TRD Gas System

and argon - remain in the gas phase and can be pumped out. The remaining solids, freed from impurities to a certain extent, are progressively warmed up and either recirculated for further cleaning (repetition of the distillation procedure) or compressed into a storage cylinder. By ensuring sufficient, continuous cooling a large amount of gas can be injected into the plant's volume which is able to hold up to 15 bars of pressure.

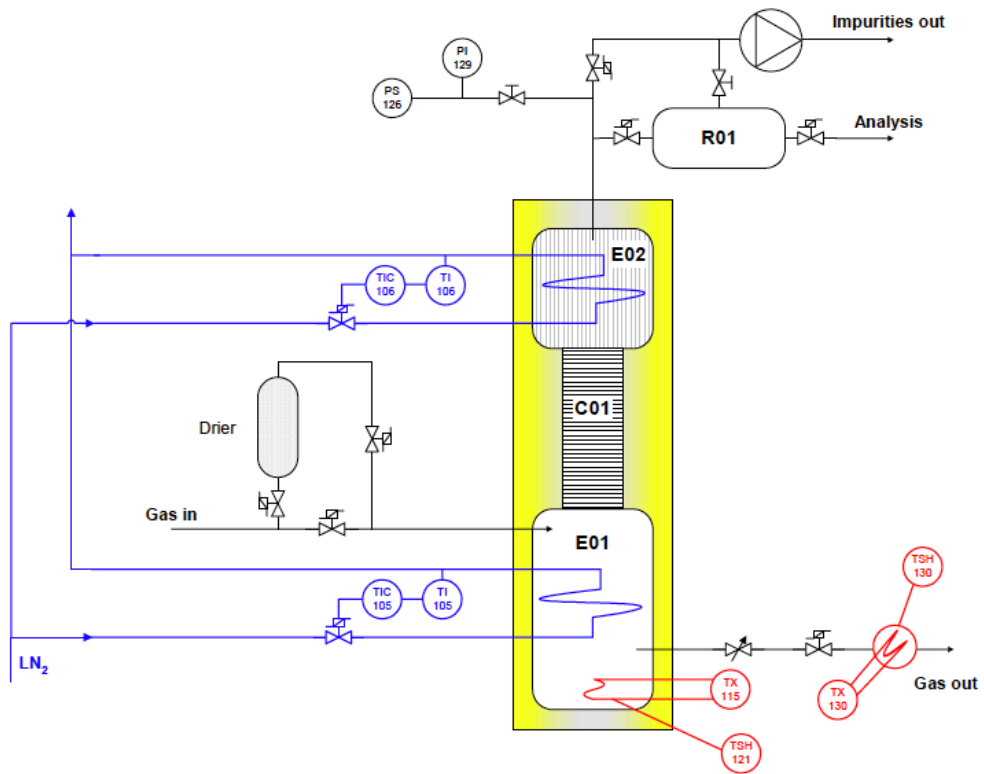


Figure 5.15: The recovery plant as designed for the ALEPH experiment. It consists of a 100 l distillation column divided into three compartments (E01, E02, C01), a sample volume R01, a LN₂ cooling circuit with temperature regulation, provisions for heating up the bottom of the column, and several pneumatic and manual valves for the operation of the plant [45].

5.5 Surveillance And Control Software

As mentioned in chapter 5.1, the TRD as part of one of the four LHC experiments, is provided with a unique control system - the GCS - consistent of supervision and process control layers for its gas systems. In addition, the software running the GCS has an interface to provide information to the Detector Control System (DCS) of the ALICE experiment and its sub-detectors such as the overall status and all the data concerning the gas system. Control is not possible from non-GCS systems, though, which means that from the ALICE DCS it is only possible to monitor the gas system. Each sub-system is responsible for its own gas user interface and the integration into the main DCS. Therefore, a UI (see figure 5.16) with the appropriate data point connections and displays has been developed as part of this thesis to make it possible for a common user to observe the gas system.

The GCS expert user interface for monitoring and controlling the system is provided by CERN's Industrial Controls and Engineering (EN-ICE) group. Each function of the gas system is integrated into its own logical module run by a PLC which provides the possibility to regulate the above described devices according to set points, reacting to alarms, executing user commands etc. The user interface allows the operator to change the state of the whole gas system or to act on single components. It also provides logging of the various data points into a data base for inspection of trends. Furthermore, a set of configuration files (so-called recipes), editable by the gas expert, provide the human-machine interface between the user and the PLC. Figure 5.17 shows the panel of the mixer unit as an example of the present TRD gas system UI. The distribution, pump, purifier, exhaust, analysis and membrane module as well as the overall gas system have similar GUIs.

5 The TRD Gas System

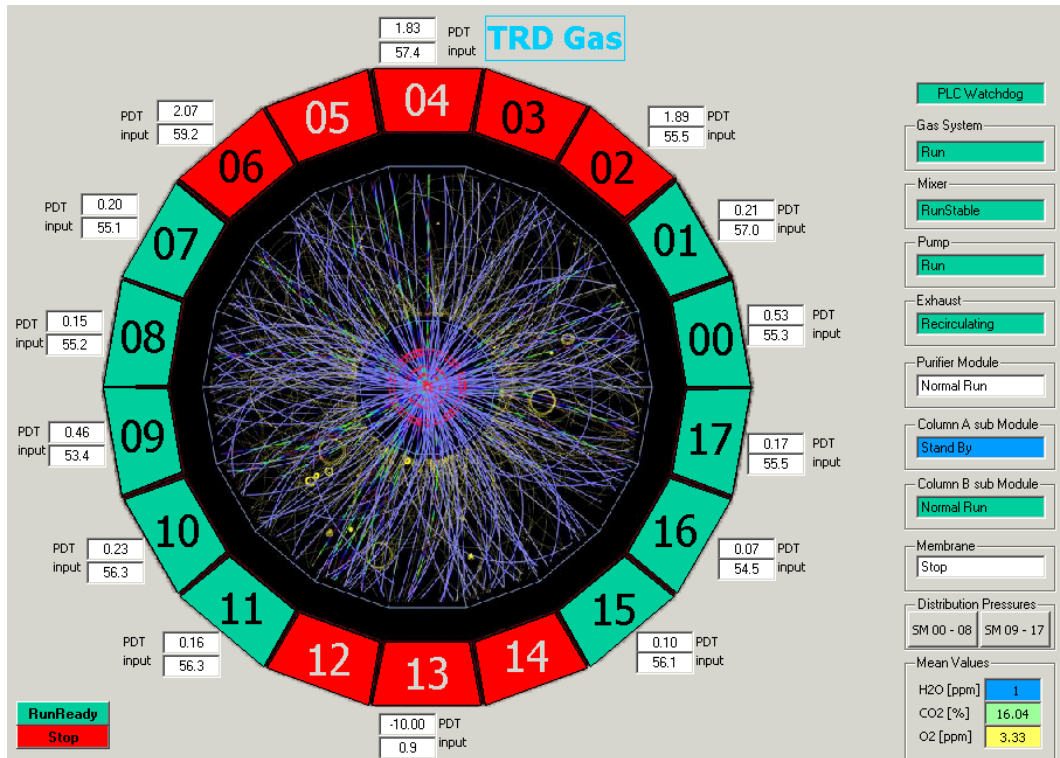


Figure 5.16: The PVSS-based UI as it is integrated into the TRDs main DCS. Here, the data can only be displayed, but not controlled. Nonetheless it is possible to get informed about alarms, follow the trends of the different data points provided by the GCS and also to archive this information.

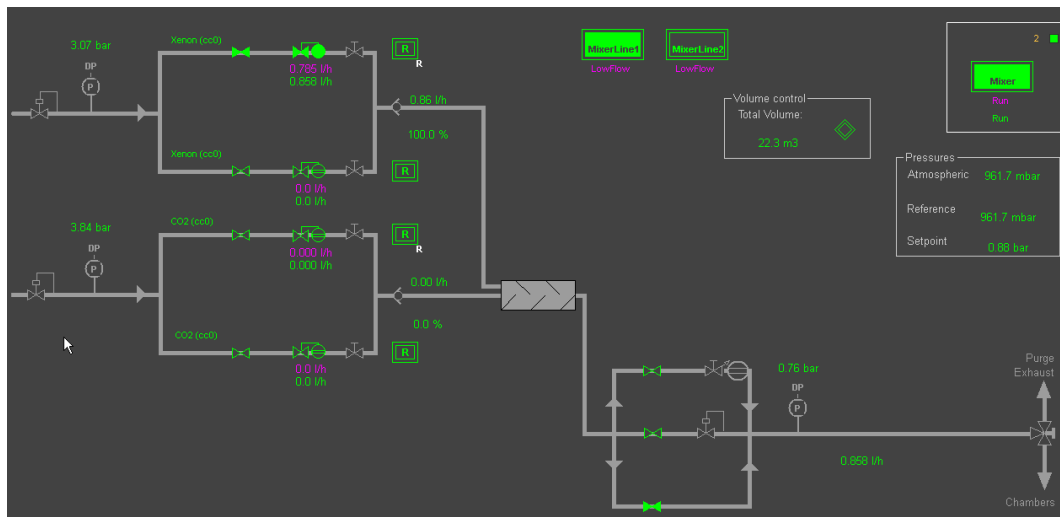


Figure 5.17: GCS-provided UI of the mixer module of the TRD gas system.

5.6 Operating, Maintaining, Upgrading

This section is dedicated to the incurring tasks when aiming at the achievement of a smooth operation of the gas system and therefore the successful running of the TRD. Furthermore, it discusses improvements and upgrades that have been carried out as part of this work.

Test of the xenon supplies for purity

With the help of the GC/ECD each new xenon supply is tested for purity with respect to SF₆. Figure 5.18 shows the chromatogram of several injection samples from a xenon supply that was analyzed in 2009. After calibration of the device with pure SF₆ the amount of SF₆ in the xenon supply was found to be approx. 21 ppb.

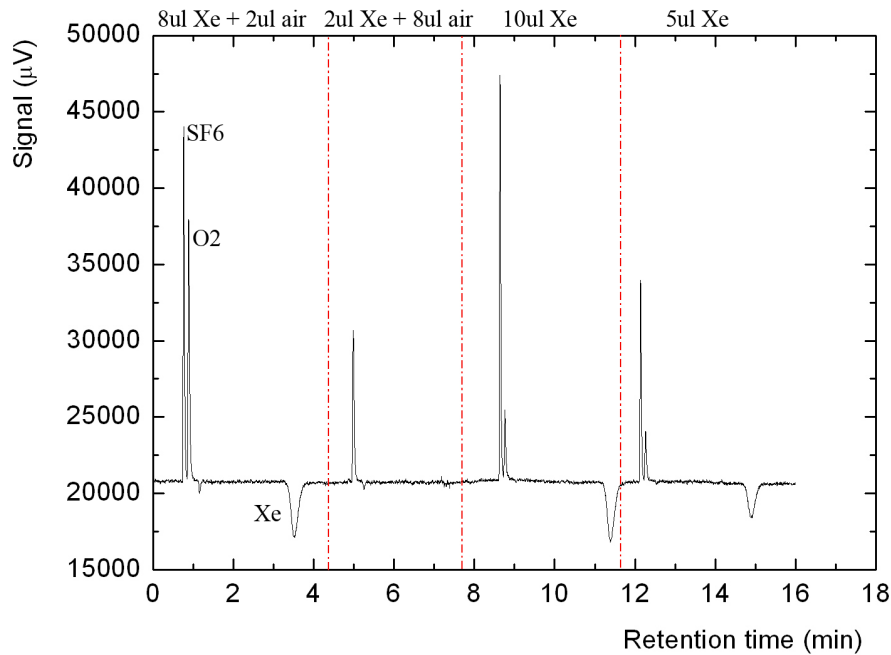


Figure 5.18: Chromatograms of an SF₆-contaminated Xe supply

A second analysis procedure was undertaken afterwards using ⁵⁵Fe pulse height measurements. For this purpose a small monitor detector with the same electrical field configuration as the TRD drift chambers had been developed earlier. In principle,

5 The TRD Gas System

a collimated ^{55}Fe source radiating x-rays is placed in front of the entrance window. The photons are absorbed mainly at the beginning of the drift region, while the cluster of primary electrons drifts along the drift region but becomes attached at some point over this distance. It was found that the SF_6 contamination of the xenon lead indeed to a pulse height decrease. Using $A = p \cdot p_I \cdot C_I$ to determine the attachment rate, where C_I is the attachment coefficient of the impurity I (here: SF_6), p the gas pressure and p_I the concentration of the impurity responsible for the attachment, known as the partial pressure. Inserting A into equation 5.4 the signal loss was found to be $< 5\%$ ($N/N(0) < 0.95$) and therefore acceptable. Similar analysis and measurements have been carried out with all the xenon supplies as well as several samples from the ALICE cavern.

Purifiers: CO_2 trapping

Until October 2010 the regeneration of the purifier columns had been done manually whenever the H_2O contamination exceeded 100 ppm but without additional action or considerations. It was then discovered through jumps in the drift velocity that each time the operating cartridge is swapped the amount of CO_2 in the operating gas decreased by a certain value as can be seen in figure 5.19. This was due to the fact that next to the contaminants to be removed intentionally, mainly CO_2 is trapped in the cartridge cylinder and material, and was vented out when the cartridge is saturated (before the regeneration process). Therefore it had been decided to inject this amount of CO_2 (manually) directly into the gas system before each regeneration. This operation has led to a stabilization of the gas composition and therefore the drift velocity within the TRD.

Membranes

- Operation in 2008

In September 2008 the efficiency and readiness of the membranes was first tested with a premixed Xe-CO_2 (80-20) gas mixture. This test revealed that after the second stage of separation there was only 0.01 % CO_2 left in the gas that was sent to the recovery plant. On the other hand the gas chromatographies after the operation showed the following: the gas that went into the

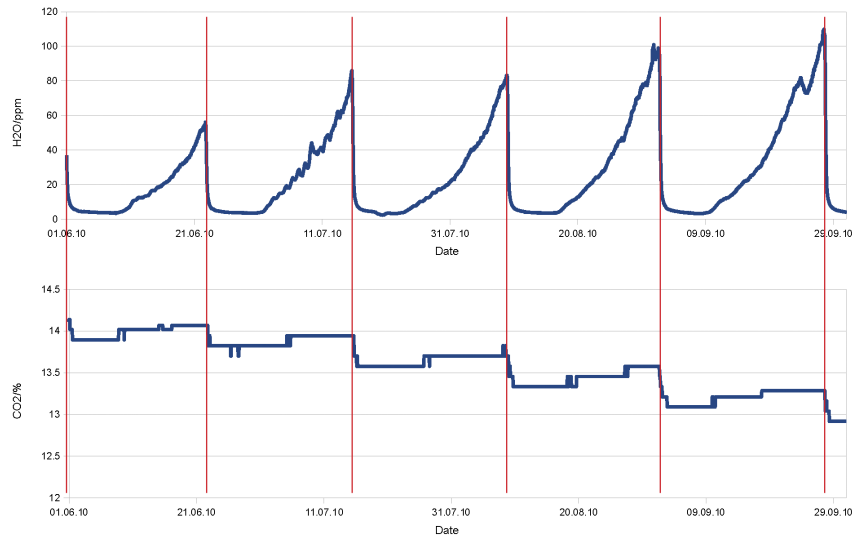


Figure 5.19: Erratic decrease of the CO₂ content due to the swapping of the purifier cartridges. (Swaps indicated with red lines.)

second stage after the first separation step contained approx. 27% of xenon. This value decreased to 2.4% after the second step (see table 5.2). An estimation lead to the conclusion that roughly 0.5 m³ of xenon would be lost after cleaning the fully assembled TRD which lies within the limits set by the TRD collaboration.

membrane stage	signal CO ₂ [μ V]	signal Xe [μ V]	signal N ₂ [μ V]	amount [μ l]	CO ₂ [%]	Xe [%]	N ₂ [%]	FRest [%]
1 st to 2 nd	30.52	15.0	0.19	123.1	72.41	26.97	0.11	0.51
2 nd exhaust	29.44	0.96	0.0	88.6	97.04	2.40	0	0.56
2 nd recup.	0.004	54.74	0.0	121.7	0.01	99.59	0	0.40

Table 5.2: Gas chromatography results of the operation of the TRD membrane module.

- SM insertions

From beginning of 2009 until the beginning of 2012 nine supermodules have been added to the TRD. Each time a new supermodule was inserted and ready for implementing into the gas loop the membranes had to be operated. This is due to the fact that the supermodules are flushed with and therefore full

5 The TRD Gas System

of CO₂ to ensure complete removal of any traces of air. This operation is performed following adjacent steps:

1. The input and output valves to and from the SM to be implemented are opened.
2. The mixer module is set to injecting pure xenon into the system.
3. The membranes remove CO₂ while the fresh xenon enters with a flow of ≈ 300 l/h.
4. The gas mixture is observed with frequent chromatographies until the desired composition is reached.
5. The membranes are stopped and the system put back into normal operation mode.
6. Eventual fine readjustment of the gas composition is done with the help of the mixer unit where the flows and ratios of Xe and CO₂ can be set accordingly.

The efficiency of the membranes was verified and remained equally good all throughout these operations.

- Argon accident in 2011

At the beginning of 2011 a large gas leak, resulting in huge argon intake, led to the decision to regenerate the full volume of the TRD gas. For this cleaning process (removal of Ar) the cryogenic plant (see previous chapter for details) was used. Before and during the operation of this device the gas had to be separated from the CO₂ for which the above described membrane operation sequence had to be performed. The only difference this time lay in the fact that the xenon was not circulated back into the loop but sent into the cryogenic plant for further cleaning. After about one week of operation the xenon had been completely separated from the CO₂ and pumped into the distillation device for further processing.

Cryogenic plant

- Frequency of operation

As mentioned earlier, the frequency of operation of the cryogenic plant is determined by the maximum tolerable concentration of N_2 concerning the detector's performance and the amount of xenon-loss per operated process. Simulations of the influence of nitrogen in the TRD Xe-CO₂-mixture on gain and drift velocity (as had been shown in figure 5.8) have revealed that a small amount of N_2 is acceptable and its influence can be compensated for by readjusting the voltages applied to the detector.

In 2002 [45] it was assumed that the main potential sources of leaks in the TRD are the gas connections between the chambers and the leak rate was extrapolated to $L \approx 0.05$ l/h which would amount to about 250 l/xenon per ALICE cycle (8 months). Estimations of the evolution of the N_2 concentration in the TRD gas mixture for a leak rate five times higher than expected gave a value of $N_2 \approx 4.5\%$ in this period. Recent experimental data have lead to an even better result. Within a period of eight months (April - December 2011) the N_2 had increased from 0.6% to only 2% (compare figure 5.20) resulting in the estimation that 4.5% nitrogen in the TRD gas would not be reached before the end of 2012.

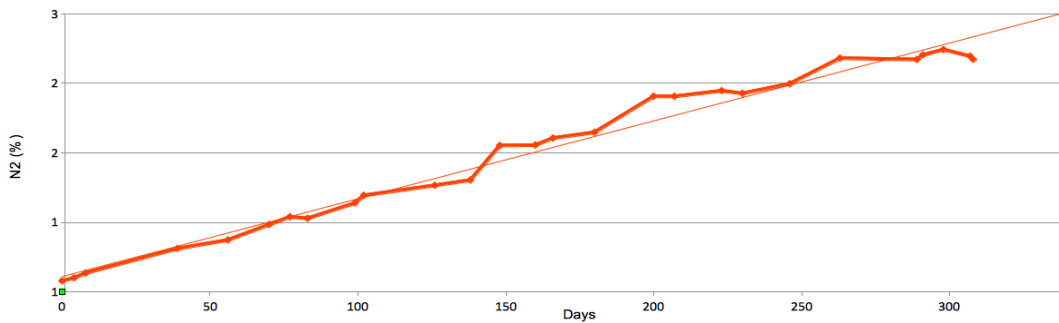


Figure 5.20: Increase of nitrogen in the TRD gas mixture over a period of eight month (April - December 2011).

In 2008 the ALEPH plant was tested with a Xe-CO₂ mixture to determine its functionality and efficiency. As previously described the xenon loss in the preliminary process of CO₂ removal amounted to 2.4% (i.e. approx. 0.5 m³

5 The TRD Gas System

for fully assembled TRD). On the other hand, there was no Xe lost during the cryogenic distillation and the N₂ removal efficiency was better than 99% (less than 1% of nitrogen left in the gas, see table 5.3).

CO ₂ signal	Xe signal	N ₂ signal	total	CO ₂	Xe	N ₂
1.035 μ V	59.66 μ V	0.3425 μ V	136.1 μ l	2.22 %	97.05 %	0.49 %

Table 5.3: Gas chromatography of the recuperated gas after a full distillation process.

Taking all these factors into account it was decided to go through the distillation of the full TRD gas volume once per year.

- Argon intake in 2011

In February 2011 it was discovered that under certain circumstances the TRD gas system was losing gas. Through intense investigations a significant intake of argon was detected but unfortunately the source of argon only found when there was already 6.6% Ar in the gas mixture which happened within seven weeks as can be seen in figure 5.21.

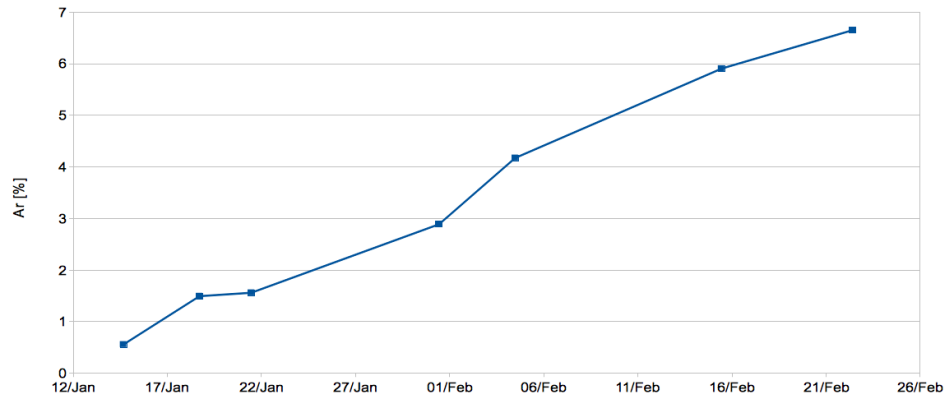


Figure 5.21: Increase of argon as a function of time caused by a faulty pressure regulator.

Data taken from analysis with the gas chromatograph.

The cause of the argon intake was found to be a faulty pressure regulator in the mixer module. Those low pressure reducing valves can be pressurized on one side to extend their dynamic range. This is done hydraulically with the help of another gas, in this case argon. Together with the N₂ accumulated over the previous year, the TRD gas mixture became Xe-CO₂-Ar-N₂ [80.1-11.2-6.6-2.2 %].

5.6 Operating, Maintaining, Upgrading

The resulting pion rejection degrades by $> 40\%$ due to a lower TR absorption and Fermi plateau (see figure 5.22). Since neither the purifiers nor the membranes are capable of removing the argon, it was decided to cryogenically regenerate the gas. The regenerating procedure including the membrane operation had to be done in two similar steps to be able to cope with the large volume of gas ($\approx 18 \text{ m}^3$). After half the gas of the TRD was taken out (and replaced by CO_2 in the same motion) the cryogenic plant was stopped, the gaseous components - namely argon and nitrogen - pumped out, the device heated up and the clean xenon compressed into a cylinder. In the regenerated gas, only 0.008% Ar and 0.065% N_2 remained which proved the outstanding functionality of the cryogenic plant. When all the xenon was pumped out, the whole process was started a second time with the remaining gas resulting in a gas purity of 0.1% Ar and 0.7% N_2 . The regenerated xenon was then recirculated back into the system (with the help of the membranes removing the CO_2). To avoid another similar incident this pressure regulator has been removed from the TRD gas system, since it was obsolete in any case.

- Proposals for improving the recovery plant

The whole process of cleaning the TRD gas was done manually and needed careful supervision throughout the complete operation of about two weeks which made it a very time consuming and tedious task. Therefore, a plan was subsequently developed to improve the procedure by having certain steps performed automatically. A schematic of the recovery plant with the upgrade proposals can be found in figure 5.23. The most helpful task to be automated is the monitoring and control of the pressures in the plant (P1) and at the inlet to the compressor that pumps the clean gas out into the storage cylinders (P2). A PLC would drive the heating of the plant, switching it on when $P1 < 5 \text{ bar}$ and off for $P1 > 8 \text{ bar}$. Another PLC would control the compressor according to its constructional working range, switching it on for $P2 > 1 \text{ bar}$ and off if P2 goes lower than 0.7 bar . This way both working steps would be executed depending on each other, to keep the conditions stable and to minimize the risk of too high/low pressures. As described above the recuperation of the

5 The TRD Gas System

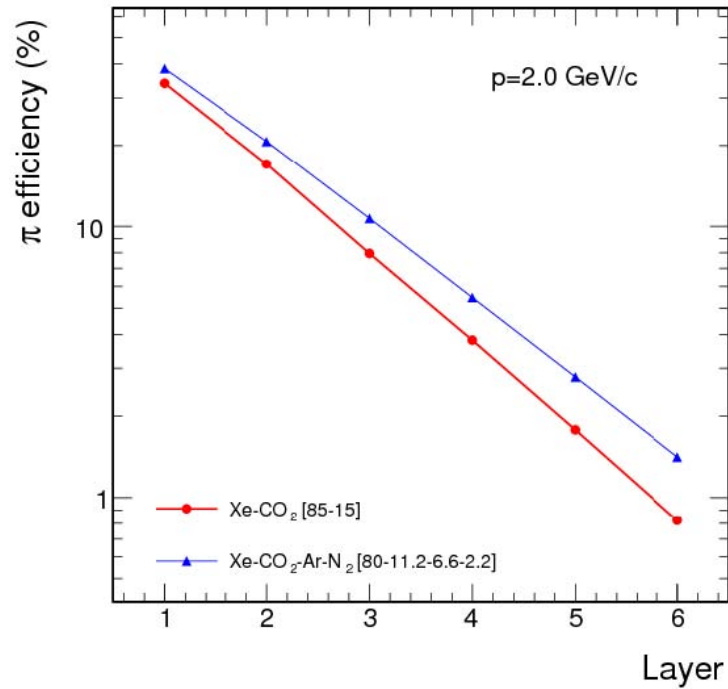


Figure 5.22: Simulation of the impact of the N₂ and Ar contamination in the TRD gas on its pion rejection (per supermodule layer) [51].

clean gas had to be done in two steps since one storage cylinder could not hold the total amount of gas from the TRD. This led to interrupting the whole procedure, pumping out the vaporous contaminants, heating the plant up and compressing the xenon into the first bottle. Afterwards the whole device had to be cooled down again to continue with the procedure. Filling of two bottles (or three when the TRD is fully equipped) at the same time would result in the advantage of not having to stop midterm and the ability to carry out the operation continuously, minimizing the risk of losing gas and accelerating the process. Another very crucial point is to have a continuous liquid nitrogen flow to ensure stable (cold!) conditions in order to not risk the re-gasification and therefore (re)mixing of the contaminants with the xenon. Until now, the tanks had to be exchanged about every three days depending on the ambient conditions. Thus, a connection to the already-present LN₂ tanks in the Point 2 area needs to be installed. Lastly it was proposed to add a pressure sensor and balances (S1, S2) to measure the amount of Xe in the bottles, since the

volume could only be estimated by watching the pressure in the cryogenic plant itself. Equally, it would be best if the weight could be read-out and thereby monitored with the help of a PLC. At present, the cryogenic line for nonstop cooling has been realized, the additional upgrade is a pending task.

Leak hunting, detecting and fixing

As has already been pointed out several times, it is very crucial for the smooth operation of the TRD to avoid any kind of leak through which impurities could enter the gas. First indicators are always the oxygen and water levels in the system. An increase of these two components is a strong indicator of air intake somewhere in the system. When a leak is suspected, actions need to be taken immediately. There are several ways to locate a leak as close as possible, which is not an easy task in a gas system as big as the TRD's. The first step is always to close down the area in which the leak could be. For this, the gas system needs to be segmented step-by-step, parts of it isolated and pressure tests undertaken until anomalies (pressure loss) are found. If a leak is present in one of the supermodules there is always a prominent peak in the O₂ analysis spectrum making it possible to identify the leaky sector. To confirm that the leak is located correctly, the problematic SM is disconnected from the gas loop, put under a higher pressure than normal and all valves to and from it closed. Then the pressure behavior is observed very closely. If a pressure drop is noticed, one can confirm that the SM is losing gas and needs to be investigated as quickly and as intensely as possible. In the better cases, the leak is located in one of the external gas connections that can be accessed rather easily. To pinpoint the leak, either a leak hunting device ("sniffer") or gas detection spray ("bubble gas") is made use of. A sniffer is a portable, electronic gas leak detector based on the principle of thermal conductivity. With this rather small device, even locations that are hard to reach can be tested in a one-hand operation. An audio signal helps with the localization of leaks. The sensitivity is automatically set to the leak rate, with the peak values measured and displayed on a screen. It is sensitive to gases like He, CH₄, CO₂, Xe and Ar. Bubble gas is made of extremely sensitive water-thin liquids that can be sprayed onto a potential leak area. Large gas leaks produce bubbles, while small gas leaks cause foaming. Faulty gaskets, pipes or connections have to be

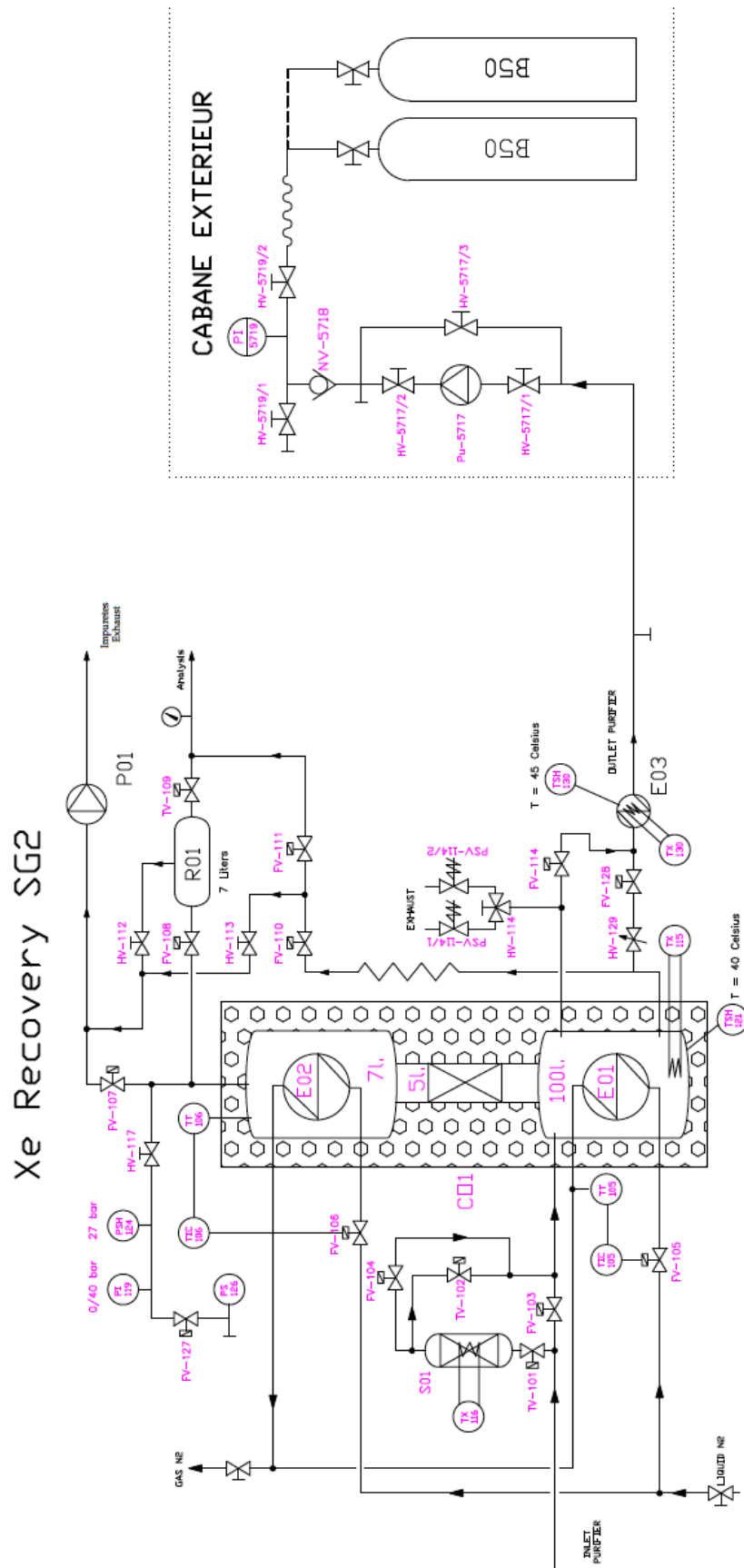


Figure 5.23: A schematic of the recovery plant as it is presently installed in the TRD gas circuit.

replaced or simply tightened, if possible. However, if the leak cannot be traced on the outside of the SM and instead seems to be located inside the chambers, there is effectively no means of repairing it during the running period. The option that remains is to wait until the big winter shutdown where the leaky SM could eventually be taken out of the TRD to be disassembled, tested, fixed and reassembled on the surface³. To ensure that an SM is as tight as possible, intensive tests are carried out on the surface (see next section) before the SM is inserted into the TRD setup in the ALICE cavern.

A similar procedure (segmentation of the system) can be applied for all other parts of the gas system that are in overpressure. The situation becomes more difficult when a problem occurs in the low pressure part (around the pump module), since the sniffer cannot be used there. Pressurizing minimizes the area in which the leak might be but the exact location is hard to find. Therefore, all one can do is tighten/exchange parts that might be the cause of the leak (trial and error).

TRD Surface Testing

Whenever a new supermodule arrives at point 2/CERN it has to be tested for integration readiness before adding it to the already installed TRD supermodules in the ALICE cavern. Each SM undergoes tests of its electronics, gas tightness, high-voltage distribution and cooling. The gas leak tightness measurement of the supermodules is one of the most important tests to be performed to minimize the loss of Xe during operation. For this purpose a test stand has been developed and upgraded as part of this thesis to have the surface testing as close to the experiment's conditions as possible. Each supermodule has three gas inlets (layers 0, 2, and 4). The gas flows through the layer until it reaches the end of the SM where it is redirected to the next upper layer and flows back to the outlet (layers 1, 3 and 5). Each inlet is equipped with its own gas supply to have a uniform circulation of the gas flow. Therefore, similarly to the distribution in the ALICE cavern, the premixed gas from the gas supply battery sitting close to the test stand is split into

³In the beginning of 2008 two of the supermodules had internal gas leaks that were only discovered after they had already been inserted into the TRD setup wherefore it was operated under Ar-CO₂ during this data-taking period (cosmics) until these two supermodules could be fixed.

5 The TRD Gas System

three lines, each connected to a mass flowmeter for individual control. Furthermore, the setup is equipped with a safety bubbler (additional to the one connected to the supermodule) to prevent excessive pressure build up within the chamber and secondly to prevent air intake when running the compressor for “underpressure” (compared to atmospheric pressure) creation. All outlets of the SM come together in the above described manifold which has one exhaust line connected to the safety bubbler, where the excessive gas is vented out, and a second exhaust connected to an oxygen analyzer (“Orbisphere”) which can measure the O₂ content with an accuracy down to a few ppm. A schematic of the whole setup can be found in figure 5.24.

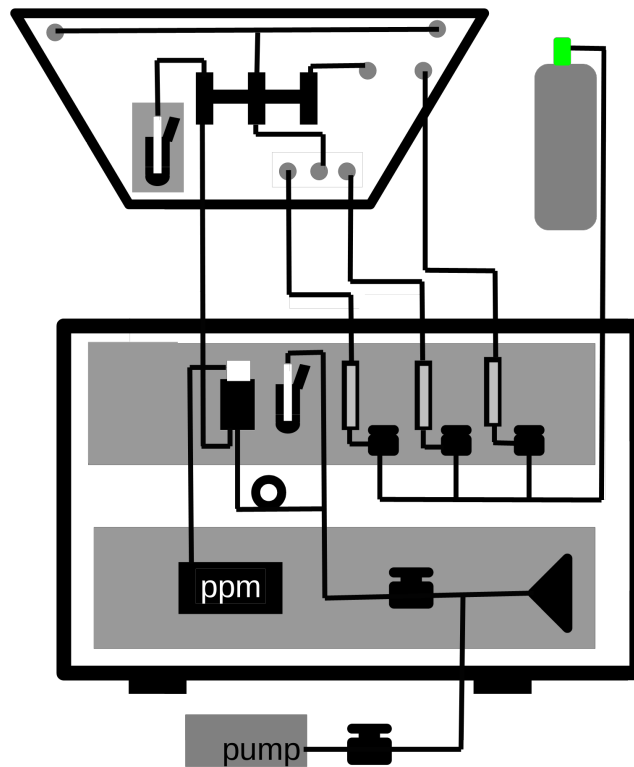


Figure 5.24: Schematic of the clean room test stand with a SM (upper left) and the gas supply (upper right). It is equipped with an oxygen analyzer (“ppm”), three mass flow controllers, a safety bubbler, a compressor (“pump”) and a fan (triangle).

The leak rate is calculated with the help of the O₂ content measured with the Orbisphere since the oxygen content in the counting gas is a measure for leaks within the supermodule. Separate tests at over- and underpressure of about ± 1 mbar

5.6 Operating, Maintaining, Upgrading

allow for the distinction of diffusive and high resistivity viscous leaks. The average leak conductance per chamber should be less than 3 NI/bar·h (NI: norm liter; 273 K, 1.013 bar) which is the limit set by the cost of xenon⁴. For these tests the supermodules are flushed with an Ar-CO₂ gas mixture while the pressure is regulated by a compressor and a fan. An example plot from one of the first supermodules can be found in figure 5.25 where the O₂ contamination [ppm] and temperature [C°] are plotted over time. The conductance evaluates via the following formulae:

$$\frac{F_{leak}}{F_{gas}} = \frac{O_2^{ppm}}{O_2^{air}} \quad (5.9)$$

$$C = \frac{F_{leak}}{p_{diff}} \quad (5.10)$$

$$= \frac{p_{atm}}{p_{diff}} \cdot F_{gas} \cdot \frac{O_2^{SM}}{O_2^{air}} \quad (5.11)$$

$$= \frac{O_2^{SM} \cdot 5 \cdot F_{gas} \cdot p_{atm}}{p_{diff} \cdot 1000000} \quad (5.12)$$

with

- F_{leak} : leak mass flow; F_{gas} : gas mass flow [l/h]
- p_{atm} : atmospheric pressure; p_{diff} : differential pressure in the SM [mbar]
- O_2^{SM} : oxygen content in the SM [ppm]; O_2^{air} : oxygen content in air [%]

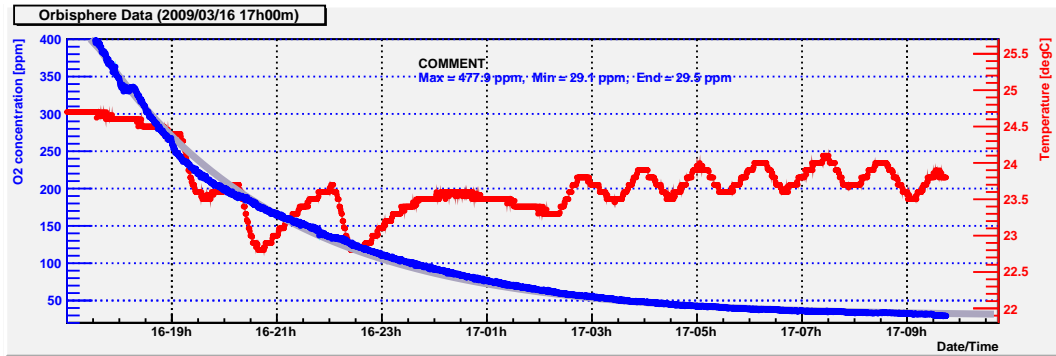


Figure 5.25: Data taken from an Orbisphere measurement. The O₂ contamination [ppm] as well as the temperature [°C] are plotted over time.

⁴For reference: 1 NI/bar·h corresponds to a leakage of 1 ml per hour at a differential pressure of 1 mbar under normal conditions.

Pressure sensor read-out

To monitor the pressure inside the SMs a software application for the pressure sensor read-out has been developed with the help of LabView[®] as part of this thesis. For this purpose a so-called **LogicBox** developed at the university of Heidelberg was used as an interface to the pressure sensors. This device is a universal control and data acquisition system with an FPGA base card and additional digital and analog I/O cards. It is built out of several directly usable modules (LogicPool), which can be freely connected for the desired purpose. The corresponding functions of the FPGA are realized with the help of a basic set of logical interconnections (LookUp Tables - LUT) and storage elements (flip-flops, registers). The actual configuration happens through switches whose respective positions are stored in the memory (RAM). The LogicBox is therefore a handy tool for signal processing. Each module has a certain number of inputs and outputs which can be connected unrestrained but then needs a specific connection list to ensure the correct data flow and processing. Several I/O submodules such as discriminators, comparators, ADCs, DACs etc. then provide the possibility of further signal processing. To assign the connections and functions to the corresponding inputs/outputs an initialization process has to be carried out at start-up, preferably with the help of a graphical programming tool (LabView in this case) to connect to an external computer via a USB interface. Subsequently, certain parameters of the modules can be set and read-out, modules controlled, and the measurement process started. The FPGA base card used is a "DL706" with a NIM/4 SU form factor, USB 2.0 interface (USB-to-serial) and a Xilinx XC3S400 FPGA (Spartan-3). The I/O interface card tailored to the FPGA is a so-called "SU 719" with a two-channel pressure meter connection as needed for the purpose at hand. The two sensors (one measuring the absolute, one the differential pressure) housed in the afore mentioned pressure sensor box provide analog output signals of 4 - 20 mA which are then digitized via this ADC. To obtain the current pressure value measured by the sensors the actual counts of the corresponding ADC channel are converted by using the appropriate calibration for this individual sensor. The general logic as realized with LabView can be found in figure 5.26. Figure 5.27 shows the actual logic developed for the specific purpose of operating the TRD pressure

sensors and figure 5.28 an example plot of a pressure measurement.

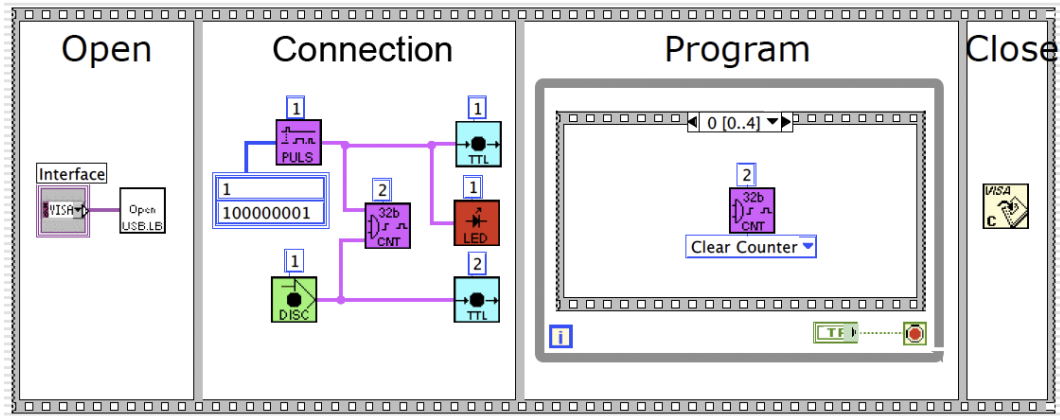


Figure 5.26: A block diagram of the logic for operating the LogicBox as realized with LabView: Step 1 - opening of the port, Step 2 - connecting and initializing, Step 3 - sequence control (parameter setting, data read-out and displaying), Step 4 - closing of the port [52].

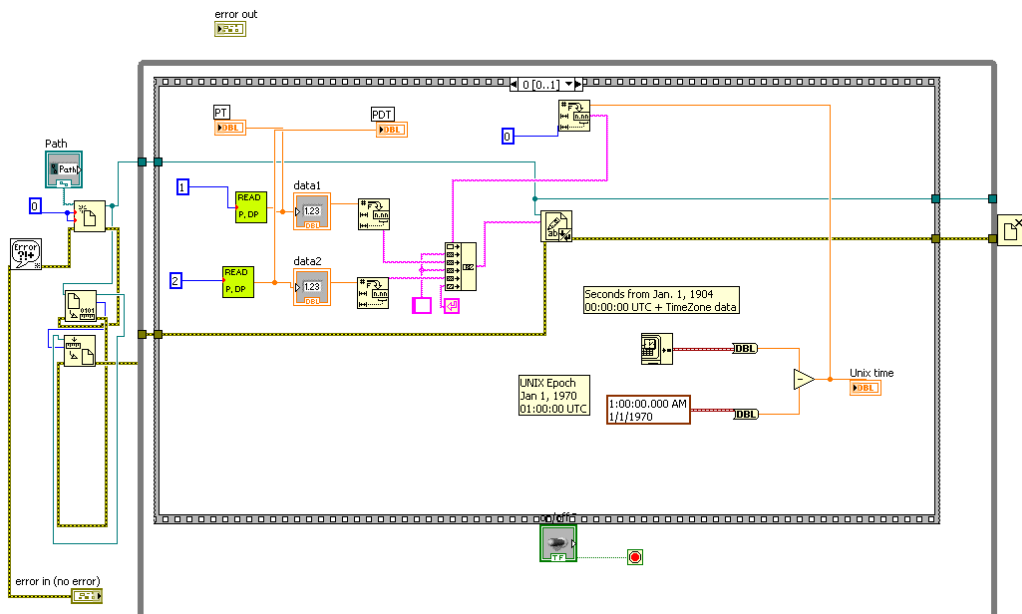


Figure 5.27: Block diagram of the specific logic developed for the read-out of the pressure sensors in the gas testing surface setup at CERN.

5 The TRD Gas System

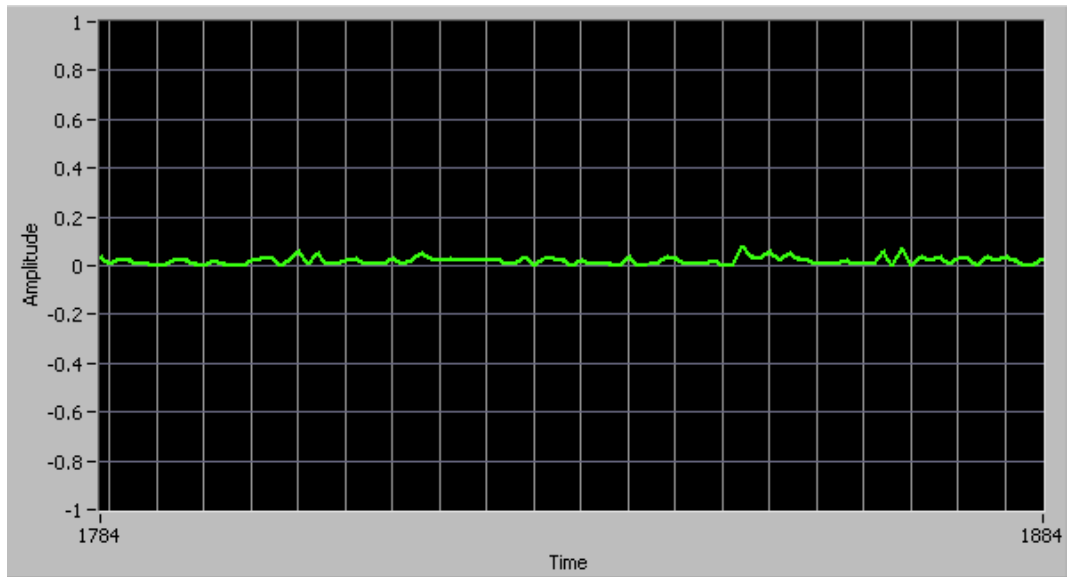


Figure 5.28: Pressure read-out display of one of the pressure sensors connected to a supermodule. The graphic shows the differential pressure [mbar] over time [sec].

Surface Storage

Since supermodules that have arrived at CERN, have been tested for functionality and are ready to be implemented into the TRD setup, usually cannot be inserted immediately, they must be stored on the surface for some time. To keep the oxygen intake as low as possible the supermodules should be kept under a low gas flow throughout the whole period of storage. For this purpose an argon (100%) supply setup has been designed and built to which up to three supermodules can be connected at the same time. Each distribution has an individual flow and pressure control similar to the test stand described earlier.

6 GOOFIE - A gas quality monitor

Gas quality monitors named GOOFIE are used for surveillance of the electron drift velocity, gain and gas properties of the TRD and TPC. The first part of this chapter gives an explanation of the importance of having such devices, briefly discusses the physics related to their operation and describes the layout and functionality. The second part is dedicated to incidents that occurred during the commissioning phase and while operating the devices together with the applied solutions, improvements and upgrades that have been carried out.

6.1 Motivation

It is mandatory to continuously monitor and control the gain and drift velocity of high resolution gaseous detectors such as the ALICE TRD and TPC to ensure their required performance. These two parameters are very closely related to the gas properties such as its components and their composition, its purity, the temperature and pressure (density), but equally the electric and magnetic fields. Another important factor is the gas composition. Due to several reasons like contamination by water or air (oxygen, nitrogen, argon) a shift of the percentages of the gas components might occur and thus affect the quality of the detector performance. Since gaseous detectors such as the TRD and TPC use high-cost gases as part of their mixtures, it is obligatory to recirculate the gas in a closed loop as described in chapter 5. This means that no gas is vented out and an accumulation of contaminants, coming from for example air diffusion or leaks, is unavoidable. As previously described, O_2 (and H_2O) can be mainly removed by the purification system, thus their contamination is expected to be less than 5 ppm (100 ppm). However, N_2 and

6 GOOFIE - A gas quality monitor

Ar impurities can not be eliminated during the data taking period and build up over time, affecting the particle identification capability of the detectors. Thus, an online gas surveillance system should be present. For this purpose, gas monitors of the **GOOFIE** type (Gas prOportional cOunter For drIfting Electrons) have been installed into the ALICE TRD and TPC gas systems to follow the conditions within the detector and be able to react accordingly. The principle of operation of these monitors is based on the measurement of the drift time difference of electrons at two known distances from a so-called pick-up counter. These electrons are produced by α -particles which ionize the detector gas along their path. This type of drift monitor has been implemented in many experiments before (NA49 [53], HADES [54], STAR [55]). Parts of the GOOFIE used for the ALICE TRD had initially been built at the Max-Planck-Institute for physics in Munich for the STAR Forward TPC and the main hardware modifications were applied and tested successfully with an Ar-CO₂ gas mixture at the University of Frankfurt/Main [56]. Afterwards, it was installed into the TRD gas system at CERN. The monitor integrated into the ALICE TPC gas system is equally an improved version of a device developed at MPI Munich [57], [58], [59]. Except for geometrical differences - mainly the size - due to the different requirements of TRD and TPC both drift velocity monitors have very similar hard- and software specifications.

6.2 Theoretical Basics

Charged particles (with mass m) moving in an electric and magnetic field are driven by the Lorentz force and can be described by the following equation of motion:

$$m\dot{\mathbf{v}} = q(\mathbf{E} + \mathbf{v} \times \mathbf{B}). \quad (6.1)$$

However, electrons that are subject to uniform fields in detector gases do not follow this resulting spiral motion. They move along straight lines on a scale of their mean free path between two interactions with the gas molecules that randomize their microscopic motion. Therefore, their equation of motion becomes

$$m\dot{\mathbf{v}} = q\mathbf{E} + e(\mathbf{v} \times \mathbf{B}) - \frac{m}{\tau}\mathbf{v}, \quad (6.2)$$

6.3 Layout And Principle Of Operation

where τ is the mean time between two collisions. There is no B-field present in the GOOFIE ($\mathbf{B} = 0$) and for $t \gg \tau$ the particle's velocity becomes constant ($\dot{\mathbf{v}} = 0$). Therefore, one can simplify to

$$0 = e\mathbf{E} - \frac{m}{\tau} \mathbf{v} \quad (6.3)$$

$$\Rightarrow \mathbf{v} = \frac{e}{m} \tau \mathbf{E}. \quad (6.4)$$

With the mean free path λ and the absolute velocity¹ v_e of the electrons, τ becomes $\tau = \lambda/v_e$. Since λ is dependent on the particle density $n \approx pV/RT$ (ideal gas law) and cross section σ of the gas ($\lambda = 1/n\sigma$) one gets

$$\mathbf{v} = \frac{e}{m} \frac{\lambda}{v_e} \mathbf{E}. \quad (6.5)$$

Therefore, the drift velocity of the electrons results from the dynamical equilibrium between the acceleration in the drift field and the energy loss due to the interactions with the gas molecules. One finds

$$\mathbf{v} \propto \frac{1}{n} E \Rightarrow \mathbf{v} \propto \frac{T}{p} E, \quad (6.6)$$

showing the dependency of the (drift) velocity on temperature, pressure and field strength [36], [56].

6.3 Layout And Principle Of Operation

A schematic of the TRD GOOFIE setup can be found in figure 6.1 and will be described in the following.

α -particles with an energy of 5.486 MeV emitted by an Americium source² ($^{241}_{95}\text{Am}$) with an average activity of 90 kBq are used to ionize the gas within the GOOFIE. Two of these sources are placed in front of a proportional counter each having a well-defined distance from each other. The emitted α -particles are detected by these

¹The electric field accelerates the electrons, while collisions with the gas molecules decelerate them, leading to a constant ("absolute") drift velocity.

²This isotope is preferred against, e.g. ^{226}Ra because it emits five times more α -particles and relatively little γ -radiation.

6 GOOFIE - A gas quality monitor

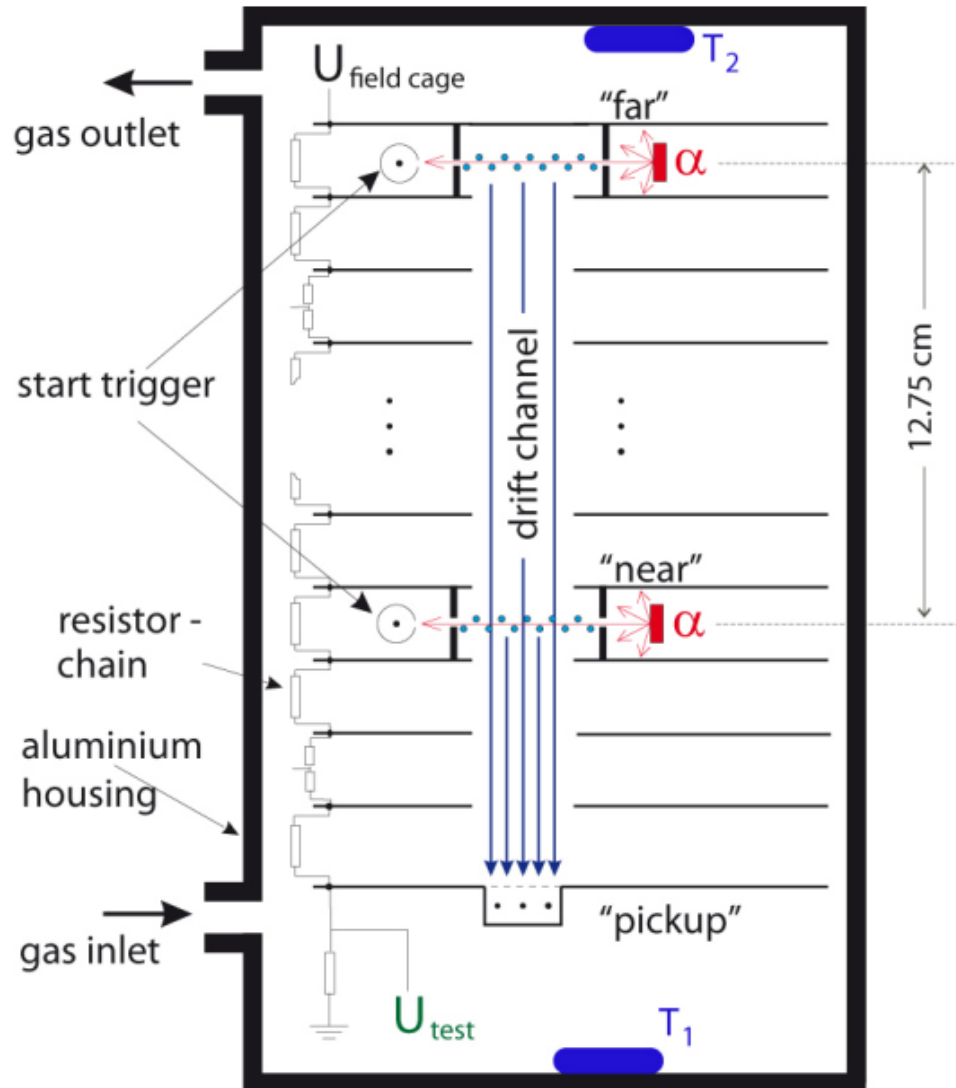


Figure 6.1: Schematic of the TRD GOOFIE [60]. A stainless steel vessel houses a field cage together with two α -sources for gas ionization, two trigger counters, a pick-up detector and two PT-100 sensors for the temperature measurement (T_1 , T_2).

6.3 Layout And Principle Of Operation

counters which create a start signal each while the electrons from the gas ionization begin to drift towards a pick-up counter at the end of the drift channel to which an electric field in upward direction is applied. When the electrons arrive at the pick-up counter a stop signal is generated giving two time values t_{near} and t_{far} for the electrons from the nearer and farther source. The difference between these two gives the drift time of the electrons. Since the distance L_{drift} between the two sources is known, the drift velocity in the homogenous field can be derived:

$$t_{drift} = t_{far} - t_{near}; \quad v_{drift} = L_{drift}/t_{drift}. \quad (6.7)$$

It was decided to use two signals in order to minimize systematic errors, since the time which elapses between the generation and the detection of the electrons in the start counters is the same for both sources. Secondly, with this method the measurement is limited to the drift channel where the electric field is the most homogenous [54]. Also, the positioning of the trigger counters (i.e. distance from the α -source) is very important and has therefore been investigated in great detail. Since the TRD GOOFIE was to be operated with Xe-CO₂ (85-15), it was necessary to distinguish the distance between the sources for this gas mixture. Due to the high density of xenon, the range of the α -particles is highly reduced compared to the less dense gases former GOOFIE devices had been operated with.

The TPC GOOFIE, on the other hand, operates with Ne-CO₂ (90-10) and had to be adapted to this mixture. Thus, the Bragg peaks³ produced by α -particles in Xe-CO₂ and Ne-CO₂ were simulated and the optimal distances calculated accordingly [56], [58]:

$$d_{TRD} \approx 25 \text{ mm}, \quad d_{TPC} \approx 40 \text{ mm}. \quad (6.8)$$

The **field cage** of the TRD GOOFIE is operated at a field strength of 11300 V which corresponds to ca. 700 V/cm, since the total length of the field cage is 16.15 cm (see below). This was initially decided to be the optimal ratio between the maximum voltage applicable and the expected monitor resolution. Furthermore (and

³A charged particle traveling through matter loses energy while ionizing atoms of the material along its path. Looking at the stopping power with respect to the path length a prominent peak occurs just before the particle stops due to total energy loss - the Bragg Peak. The trigger counters thus need to be placed shortly before the Bragg peak in order to maximize its efficiency.

6 GOOFIE - A gas quality monitor

very important), this is the field strength of the TRD itself. The TPC GOOFIE is intended to use the same working field of 400 V/cm as the TPC itself. Since its field cage has a total length of 24.7 cm, this corresponds to 10000V. However, there are only 8500 V applied at the moment due to a change in the TPC's gas mixture as will be explained below. The field cage is housed in a cylindric, gas-tight device, equipped with a gas in- and outlet directly connected to the detector's gas loop (as was explained in chapter 5). In case of the TRD GOOFIE it consists of 19 circular stainless steel plates with a diameter of 75 mm, stacked equidistantly with 8 mm between two plates. The drift channel for the electrons is created by a 10 mm hole in the middle of each plate. With a plate thickness of 0.5 mm the field cage length thus amounts to 16.15 cm. The individual plates are connected with a resistor chain of 2.7 M Ω resistors, ensuring the uniformity of the working field. Additionally, the first plate ("plate 0") is connected to ground with a resistance of 10 M Ω creating a voltage drop (U_{test}) initially intended to measure, monitor and adjust the field cage high voltage more precise than with the analogue voltmeter of the power supply. Since the plate with the pick-up detector is considered as plate 0 the two α -sources are placed between plate 3/4 ("near") and 18/19. ("far"). Hence, the distance between the two is $L_{drift}^{TRD} = \mathbf{12.75\text{ cm}}$. The field cage of the TPC GOOFIE comprises 30 parallel plates, wherefore its resistor chain is composed of 29 resistors and the distance between the two α -sources is $L_{drift}^{TPC} = \mathbf{20.4\text{ cm}}$.

The field cages are supplied by "Heinzinger" power supplies. Unfortunately, this type of device has the disadvantage of creating a significant noise due to the AC component remaining in the supplying voltage which has to be accounted for in the rest of the setup. Since the trigger counters are connected directly to the resistor chain of the GOOFIE, it was necessary to minimize this AC component by adding an external passive RC filter [57]. However, this causes a potential drop which has to be added to the desired voltage in the field cage and set accordingly at the power supply.

The **trigger counters** are small copper cylinders with a slid serving as an entrance for the α -particles and a thick gold-coated tungsten anode wire inside. The counters are connected to the resistor chain of the field cage to provide them with the

6.3 Layout And Principle Of Operation

necessary voltage of about 750 V. A schematic of one of the trigger counters within the resistor chain can be found in figure 6.2.

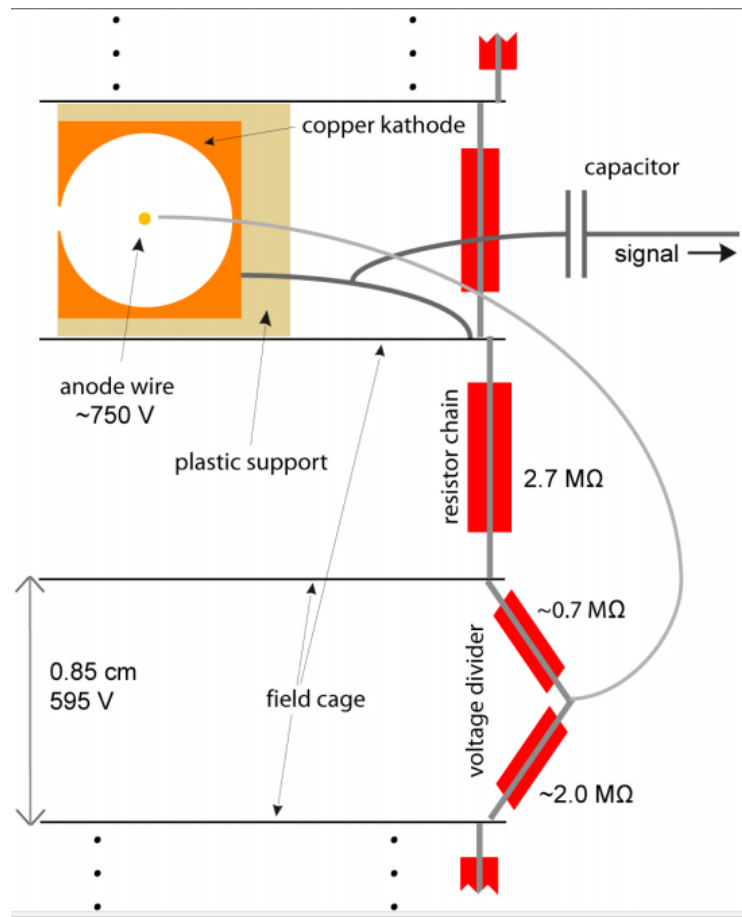


Figure 6.2: Schematic of a trigger counter in the GOOFIE field cage [56]

Providing the counters with the necessary voltage is realized by bringing them to the same potential as the neighboring field cage plate. The signal is then decoupled with the help of a capacitor. Two suitable voltage dividers ($0.68 + 2.02 \text{ M}\Omega$ each) replaced two normal resistors of the resistor chain (one per counter) making it possible to apply the 750 V to the anode wire (relative to the potential of the plate). This modification, instead of using an external power supply, was necessary to increase the stability but equally causes one small disadvantage: It limits the measurements to a certain drift field strength since the power supply of the trigger counters are coupled to it and needed modification if another voltage would be used [56].

6 GOOFIE - A gas quality monitor

The **pick-up detector** consists of two wire planes (cathode and anode) followed by a copper cathode pad where the induced signal is readout. The cathode and anode plane have a distance of 2.75 mm, and between anode wires and cathode pad is a gap of 1.7 mm. The six anode wires are divided into a center group with two wires of $0.25\ \mu\text{m}$ and two outer groups with two wires of $0.75\ \mu\text{m}$ each. After simulations [57], [58] these different diameters and the whole configuration of the pick-up detector had been found to help obtaining a uniform gain and electron arrival time. The cathode wires share the same potential as plate 0, the six anode wires are connected to $U_{TRD}^{pick-up} = 965\ \text{V}$ and $U_{TPC}^{pick-up} = 1200\ \text{V}$ and the signal is decoupled via a copper pad. A schematic of a pick-up detector can be found in picture 6.3.

In addition the GOOFIE devices are equipped with two PT100 sensors each - one at the top, one at the bottom of the housing - to monitor the enclosed gas temperature. Equally, a pressure sensor is installed. These three additional values are needed to normalize the drift velocity and gain to be independent of ambient changes (see chapter 6.4 for details).

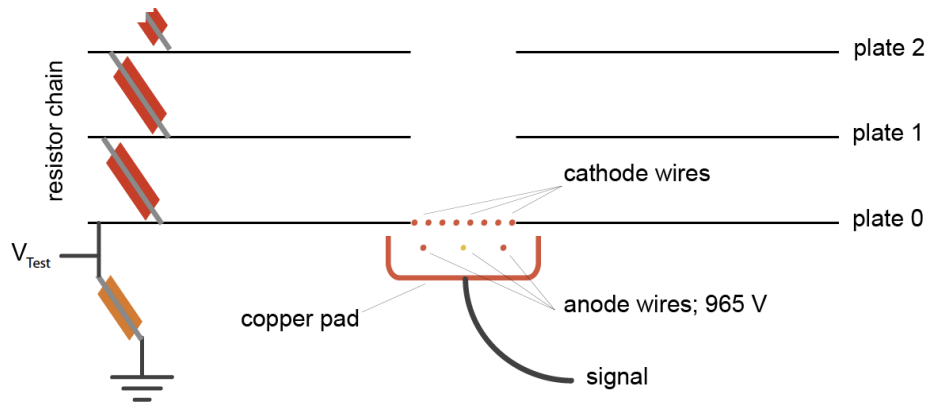


Figure 6.3: Schematic of a pick-up counter in the GOOFIE [56]

6.4 Data acquisition and analysis

Signal processing and data acquisition

The signals generated by the GOOFIE device are processed by a read-out board working with an **ALice TPC Read Out** chip (ALTRO) [61]. This board provides three signal input channels to receive the two trigger signals (near and far) and the pick-up pulses. These analogue signals are amplified and shaped by a charge-sensitive PASA (Pre-Amplifier ShAper). An ADC built-in the ALTRO chip converts the produced pulses into a digital stream and an FPGA implements the trigger logic and the data processing chain [57]. This **GOOFIE board** is powered by two DC power supplies, delivering +5 volts for analog and digital circuit respectively [58]. It is connected to a PC running the Linux operating system through a USB port. The ambient measurements (temperature, pressure, voltages) are retrieved by a National Instruments[©] board, equally connected to the “Linux PC” (via a conventional PCI card (Peripheral Component Interconnect)). Suitable software on this machine provides the possibility to either display the signals directly or to process them further with an online application and write the data into a file [57], [58]. All the collected data (GOOFIE and ambience) is not only stored locally but can also be retrieved by DCS. For this purpose, a DIM server (Distributed Information Management) interfaces between the Linux PC and PVSS. Figure 6.4 displays the whole signal processing and data read-out chain of the GOOFIE .

6 GOOFIE - A gas quality monitor

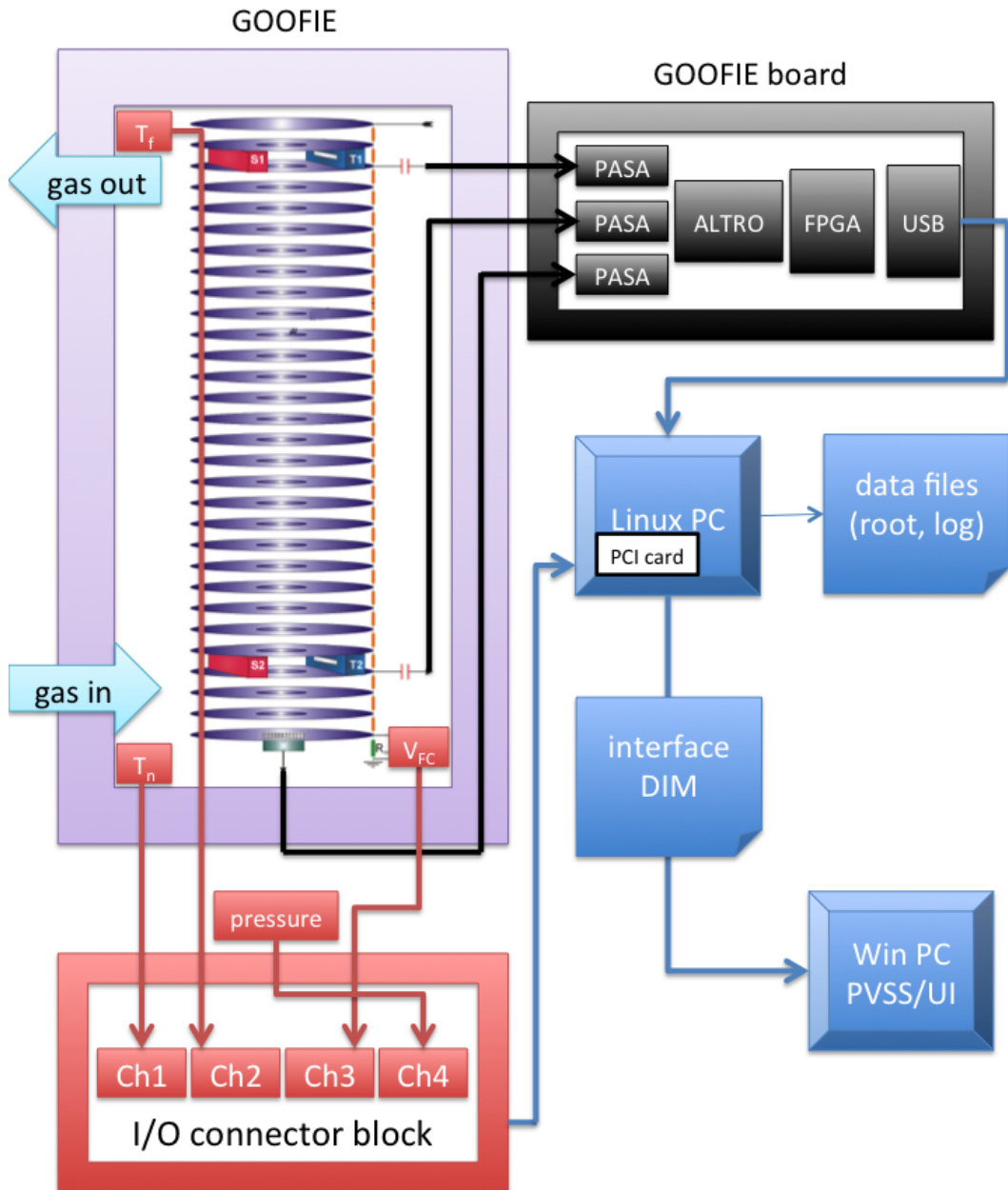


Figure 6.4: The data acquisition setup. The information from the near, far and pickup counters is processed by the GOOFIE board and sent to a “Linux PC”. The ambient measurements such as near/far temperature (T_n , T_f), pressure and field cage voltage (V_{FC}) are retrieved by a PCI DAQ board.

Data analysis

Theoretically, one event is enough to calculate the **drift velocity** since the drift time is defined and the drift length fixed. Yet, to reach higher precision an integrated signal from the sum over many events is used: 2500 events form one “pack” of data. By adding the 2500 events average values for the near and far event peak positions are retrieved (“integrated signal peak”). The drift velocity is then derived as follows: the two peaks per pack retrieved from the signals of the near and the far detector are plotted in a histogram (ADC count vs. time) as can be seen in figure 6.5 and then Gauss-fitted to find the most probable value. The distance between these two values gives the time difference between the far and the near trigger. Following equation 6.7 the drift velocity can thus be derived. For the **gain calculations** the area underneath the peaks is obtained by integrating the time bins in an extended range around the peak positions that have been found with a Landau-fit. The resulting data, normalized to the number of events contributing to these peaks, is proportional to the gas gain.

Since the **ambient conditions** influence the drift velocity and gas gain the measurements have to be corrected for temperature, pressure and the drift field voltage. Assuming the precise knowledge of p and T, the drift velocity (and equally the gain) can be corrected as follows:

$$v_{d,corr} = v_{d,meas} - A \cdot \left(\frac{p}{T} - \left\langle \frac{p}{T} \right\rangle \right) \quad (6.9)$$

where A is the slope of the linear function $f(x) = A \cdot x + B$ fitted to the correlation of v_d vs. $\rho = T/p$. Using a normalized density ρ_N ($T_N = T/\langle T \rangle$, $p_N = p/\langle p \rangle$) the drift velocity becomes:

$$v_{d,corr,N} = v_{d,meas} - A_N \cdot \left(\frac{p_N}{T_N} - 1 \right) \quad (6.10)$$

with A_N being the slope to v_d vs. ρ_N . Formula 6.10 would imply an overall uniform and constant drift field which cannot be guaranteed, though. Therefore, also variations of the voltage need to be taken into account. The correlation between v_d is still linear for small ΔU ($\Rightarrow U_N = U/\langle U \rangle$), which finally leads to the applied formula [58]:

$$v_{d,corr,N} = v_{d,meas} - A_{NU} \cdot \left(\frac{p_N}{T_N \cdot U_N} - 1 \right). \quad (6.11)$$

6 GOOFIE - A gas quality monitor

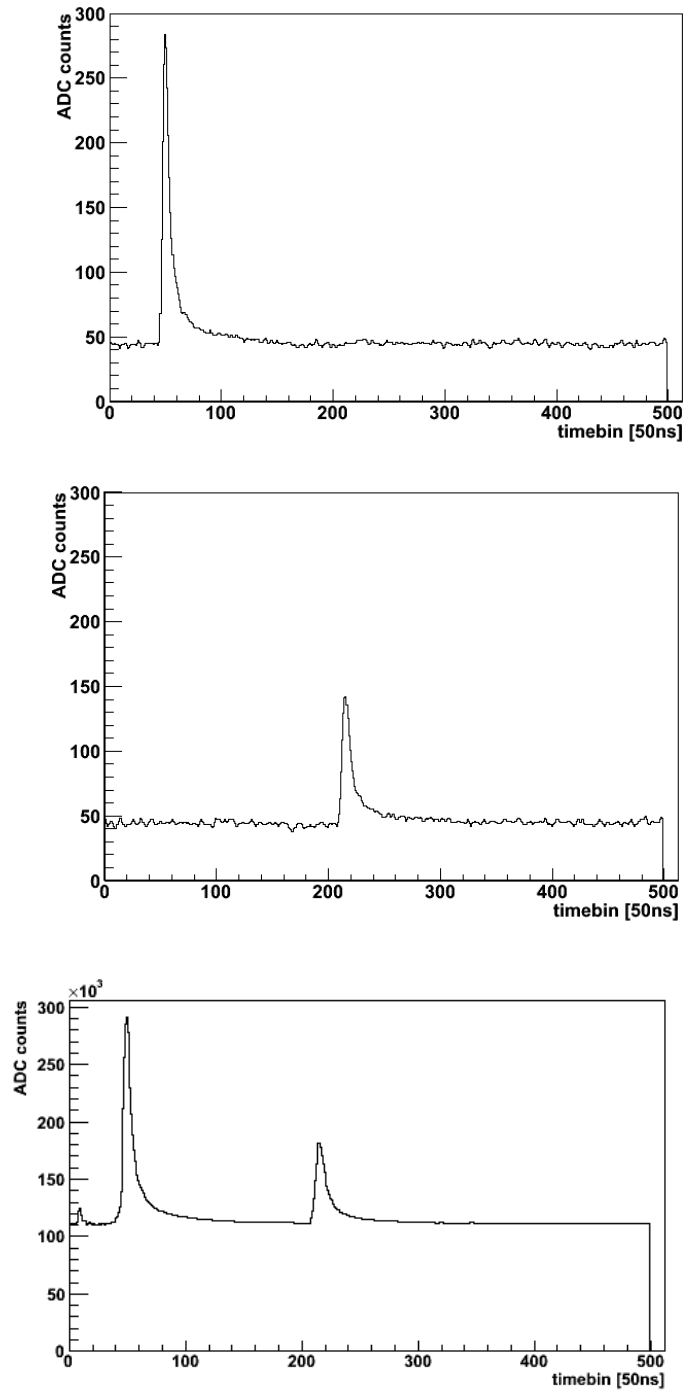


Figure 6.5: Plots of a single near (top) and far (middle) event and the sum over 2500 events from both (bottom) [62].

6.5 Maintenance, Modifications, Upgrades

The plot of simulated drift velocity data in Xe-CO₂ (85-15) against the normalized gas density and drift voltage is shown in figure 6.6. It revealed a slope and therefore a correction factor of $A_{NU} = - 2.49$ [56].

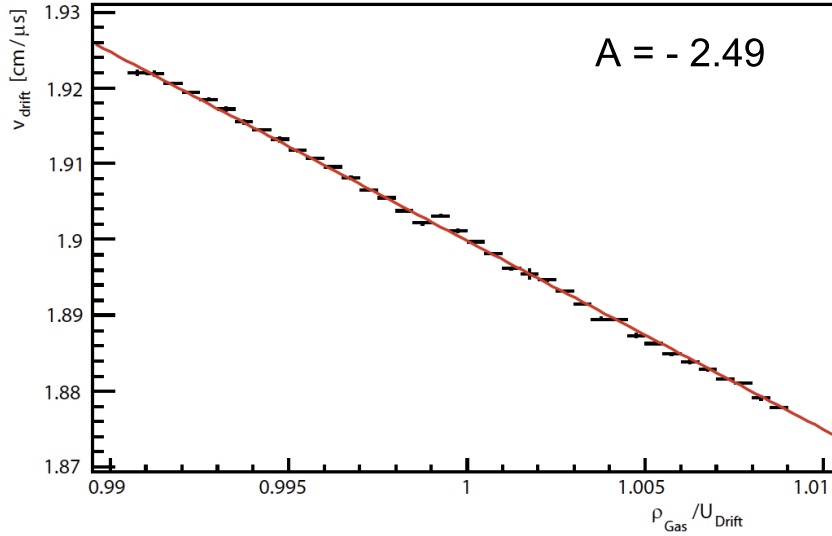


Figure 6.6: Drift velocity in Xe-CO₂ plotted against the normalized gas density and drift cage voltage $\rho_{Gas}/U_{drift} \approx \frac{p_n}{T_n \cdot U_n}$ [56].

6.5 Maintenance, Modifications, Upgrades

Since the TRD GOOFIE had initially been built for the STAR FTPC [55] and its main hardware modifications at the University of Frankfurt were only tested with an Ar-CO₂ gas mixture [56], it had to be further developed to meet the specific requirements of the TRD such as gas mixture, drift field, precision of the drift velocity and gain, etc. The incidents that occurred during the commissioning phase and while operating the device together with the applied solutions are presented in the following. In addition, the existing hard- and software had been subject to upgrades which will equally be discussed. For a better overview and structuring the section is divided into a “hardware” and a “software” part.

Hardware

- Drift field strength

Since the GOOFIE devices are very sensitive, and discharges inside the housing could lead to serious damage, the strength of the drift field has to be chosen very carefully, yet still meeting the detector's requirements as close as possible. In case of the TRD GOOFIE the total length of the field cage is 16.15 cm. To achieve a drift field strength similar to the TRD (≈ 700 V/cm) the GOOFIE drift voltage had to be set accordingly. As described above, $U_d \approx 11300$ V plus the voltage drop of 600 V at the filter box was therefore necessary. The TPC GOOFIE used to run with a drift voltage of $U_d \approx 9900$ V, corresponding to the 400 V/cm in the TPC. However, since the operating gas was changed to Ne-CO₂ (90-10) instead of the ternary gas mixture Ne-CO₂-N₂ (90-10-5), the gain at the trigger detectors is higher nitrogen which is why they would discharge at 400 V/cm. One would have to replace the resistors to the detectors in order to keep this high field (see discussion in 6.3). Since it is not yet fully clear, whether this mixture remains or whether the N₂ is re-added at some point, the field strength of the GOOFIE had to be adjusted accordingly and was lowered to 8500 V + 300 V, corresponding to a field of 345 V/cm.

- Tuning of the pick-up HV

Since no GOOFIE had ever run with Xe-CO₂ the pick-up high voltage for the TRD GOOFIE was an unknown parameter which had to be tuned slowly for finding the right setting. A voltage of $U \approx 960$ V was found to give the best signal-to-noise ratio.

- Noise

As mentioned before, a commercial PCI board (NI-6220) is used for the read-out of the PT-100 sensors inside the aluminum cylinder of the GOOFIE as well as the pressure sensor connected to the gas analysis line and the HV power supply. The sensors are connected to an I/O connector block acting as an interface to the PCI board which is installed in the Linux PC. In the commissioning phase of the GOOFIE integration into the TRD system it was

found that all of the four channels (two temperatures, one pressure, one voltage) showed a high amount of noise. After several tests of the hardware and software it was concluded that the most likely cause of the noise were the (rather aged) cables, wherefore they were replaced by new ones. Yet, this did not change the situation and the noise was still present. Further investigations of the connected hardware lead to the discovery, that the pressure sensor's resistor box whose schematics can be found in figure 6.7, had a broken resistor inside. Since simply replacing this resistor was not an easy task and to be on the safe side in case of other internal problems, it was decided to built and install a completely new box, which solved the noise issues for all channels of the NI-board.

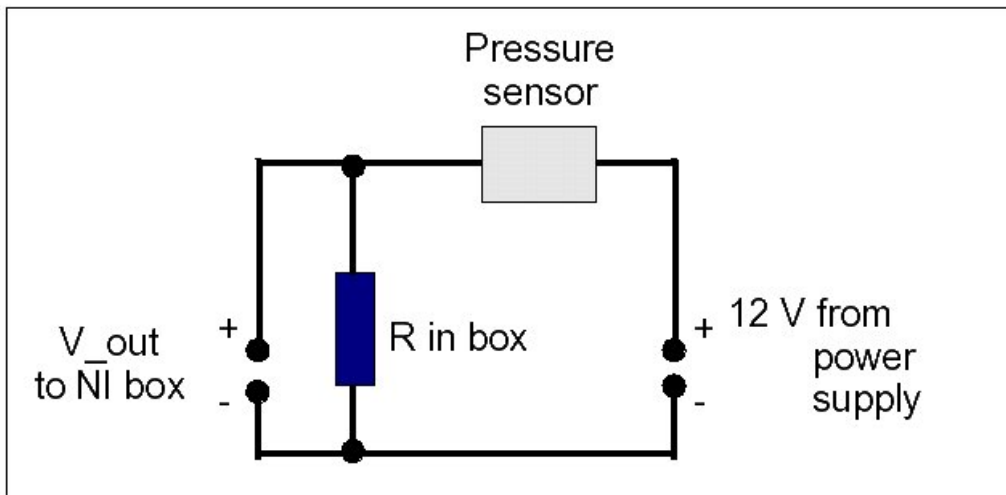


Figure 6.7: Resistor box connected to the pressure sensor.

- Calibration of the HV read-out

To readout the HV of the power supplies via the voltage drop over the last resistor in the chain, the reading had to be calibrated. This had been done earlier for the TPC GOOFIE but remained an open task for the TRD device. Within the configuration file for the online software the parameters P_0 (offset) and P_1 (slope) had to be set. The linear fit $y = P_0 + P_1 \cdot x$, where x is the voltage measured by the PCI board (NI card) (i.e. voltage drop over the last resistor) and y the value shown at the HV power supply provided these values:

6 GOOFIE - A gas quality monitor

$$P_0 = 465.47; P_1 = 9848.48.$$

- Last resistor

At some point the voltage of the field cage could not be readout anymore. After investigations of the software and hardware the last resistor (see figure 6.8) was found to be damaged and had to be replaced. For this reparation, the GOOFIE had to be stopped and dismantled to reach the resistor inside the GOOFIE. After the replacement, the possibility of reading out the voltage was given again.

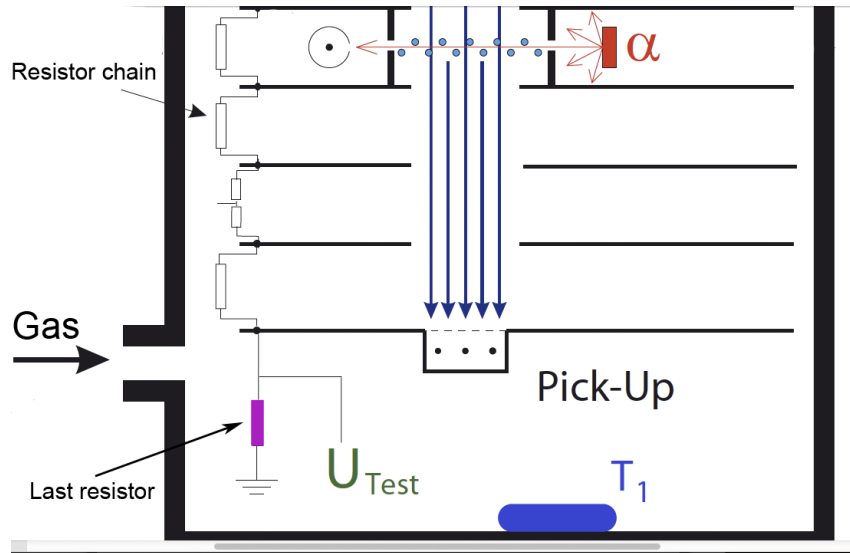


Figure 6.8: Location of the last resistor inside the GOOFIE .

- Discharges

The biggest hardware issue of the TRD GOOFIE where discharges discovered via the spectrum of the far trigger counter. An unphysical narrow spike, that was not connectable to a valid distribution generated by α -particles, was to be found along with a trigger rate much higher than one would expect. Due to experiences with former drift velocity monitors and because it had tripped on several occasions, the investigations were lead towards the high voltage network (connections, cables, sockets etc). It was found that the discharges were produced by faulty connections inside the GOOFIE, wherefore it had to be dismantled and opened for investigation.

One new resistor as well as shielding to avoid further discharges and damage by sparks was installed. After having had put the hardware back in place it was discovered that some channels of the ALTRO board were destroyed by the trips of the HV along with a damage on the PASA. The components had to be replaced and another (external) shielding was added to avoid future damage on the GOOFIE board.

The same pattern within the far spectrum was found a second time (much later and unrelated) but intense investigations on the GOOFIE lead to no result. Nothing was found broken or faulty inside and it worked properly. After all these “internal” investigations, the external hardware came into focus and the cause of the discharges lay in the set-up of the HV cable and the filter box which had to be replaced. These reparations lead to clean signals and reliable results for the drift velocity measurement.

Software

- Outliers in the drift velocity

As explained in 6.4, the drift velocity is calculated for every pack of 2500 events. Once these events are accumulated and the spectrum retrieved a Gauss-fit is applied to the peaks determining the peak positions of the near and far signal making it possible to calculate the drift time ($t_{far} - t_{near} = t_{drift}$) with high precision. However, there were additional peaks observed in the spectra of accumulated events which caused the Gauss-fit and therefore the drift velocity calculations to fail. These outliers came from the hardware for two reasons: 1.) Noise coming from the HV power supply induced baseline fluctuations, wherefore the threshold for the trigger signals had to be set rather high; 2.) some electrons, despite the trigger detector electrodes being connected to a voltage divider and a shielding of the entrance slit with a mesh, are sucked into the trigger detector, thus producing a late trigger. To solve this problem we applied improvements on the software and hardware side.

To decrease the noise the HV RC filter had to be optimized. The old filter had a resistance of 1 M Ω and a capacity of 1 nF which were replaced by R = 10 M Ω and 2.5 nF. In addition, a thin mylar foil was placed at the

6 GOOFIE - A gas quality monitor

entrance slit to the trigger detector to further mitigate the electron-socketing problem, even though this affects the trigger rate to a certain but acceptable amount. Figure 6.9 shows the improvement of the near and far signal after the hardware modifications.

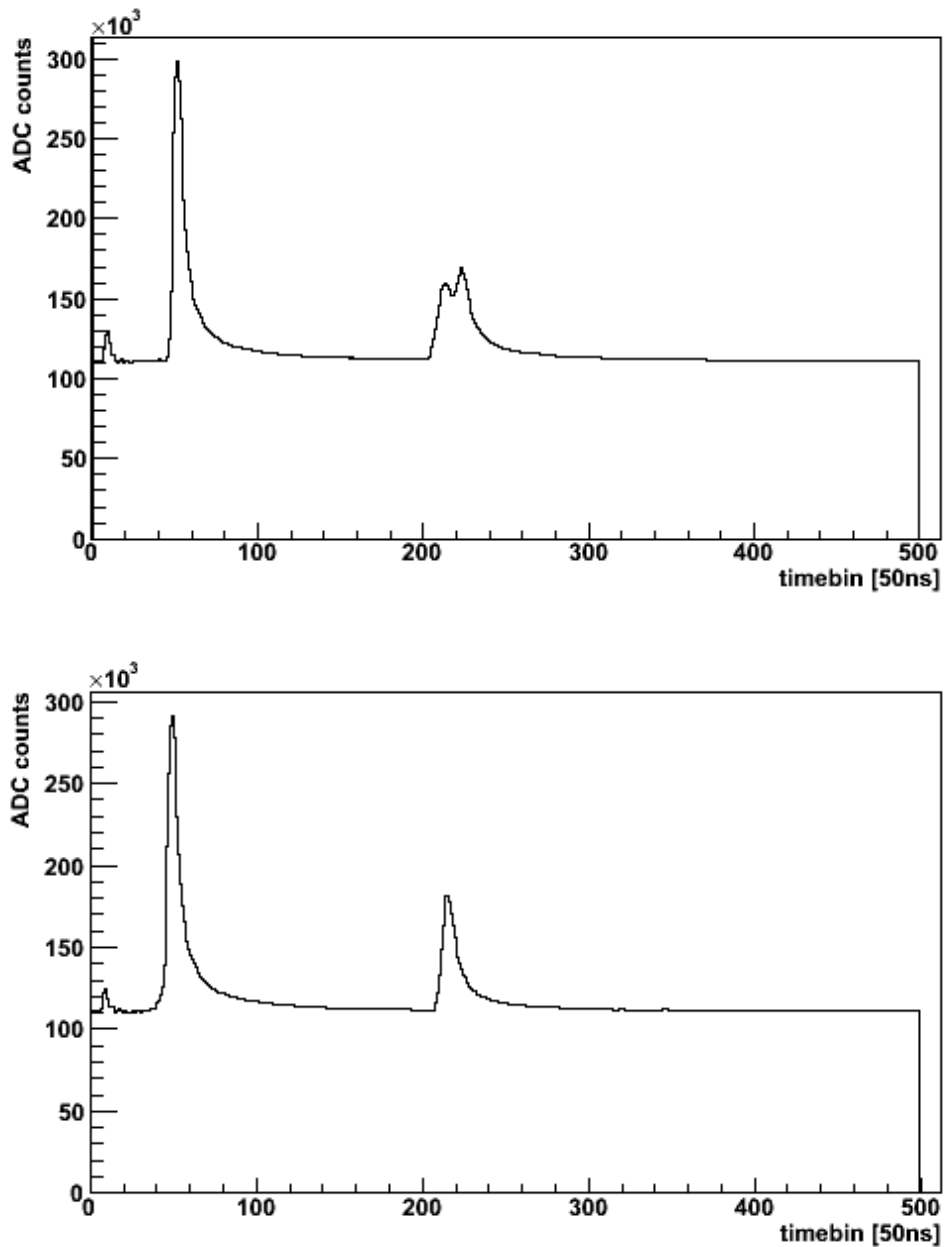


Figure 6.9: Spectra showing the near and far signal before (top) and after (bottom) installing the mylar foil [62].

Since the situation was improved but the problem not fully solvable, a work-around within the software had to be implemented. The idea was to adjust the peak width finding algorithm to force the unwanted peaks to be cut out. Therefore, the Gauss-fit window was optimized in such a way that a clean signal shape, which allows for a better peak position determination, was obtained. Thus, not only the outliers were removed but also an improvement in drift velocity calculation was achieved. These changes lead to the removal of the outliers and a satisfying provision of the drift velocity values as can be seen in figure 6.10 [62].

- Problems with the gain calibration

The gain calculations were equally affected by the baseline fluctuations which resulted in badly shaped pick-up signals. This caused the Landau-fit within the so-called peak integration range to give fluctuating gain values. To avoid these fluctuations, the gain was calculated as the integral of the fit function within an optimized fitting range such that only the proper signal peak was fully included [63].

- Gas composition online calculation and monitoring

Since the drift velocity and the gas gain in the TRD depend directly on the gas composition it is foreseen to monitor the N_2 and CO_2 content in the operating TRD gas with the help of the GOOFIE. Simulations performed by S. Dyba with MAGBOLTZ⁴ 7.1 and GARFIELD⁵ provided data files (GARFIELD) and the corresponding Townsend-coefficients⁶ (MAGBOLTZ) dependent on gas temperature, pressure, composition etc. These files and coefficients were then used as input to create a so-called geometry file whose result, calculated with GARFIELD, provides gain and drift velocity, respectively, as a function of the CO_2 and N_2 concentration. An example plot (ALIROOT) for the gain can be found in figure 6.11.

⁴<http://consult.cern.ch/writeup/magboltz>

⁵<http://garfield.web.cern.ch/garfield/>

⁶The number of electron-ion pairs per unit length generated by a negative particle moving in the direction of the applied electric field [36].

6 GOOFIE - A gas quality monitor

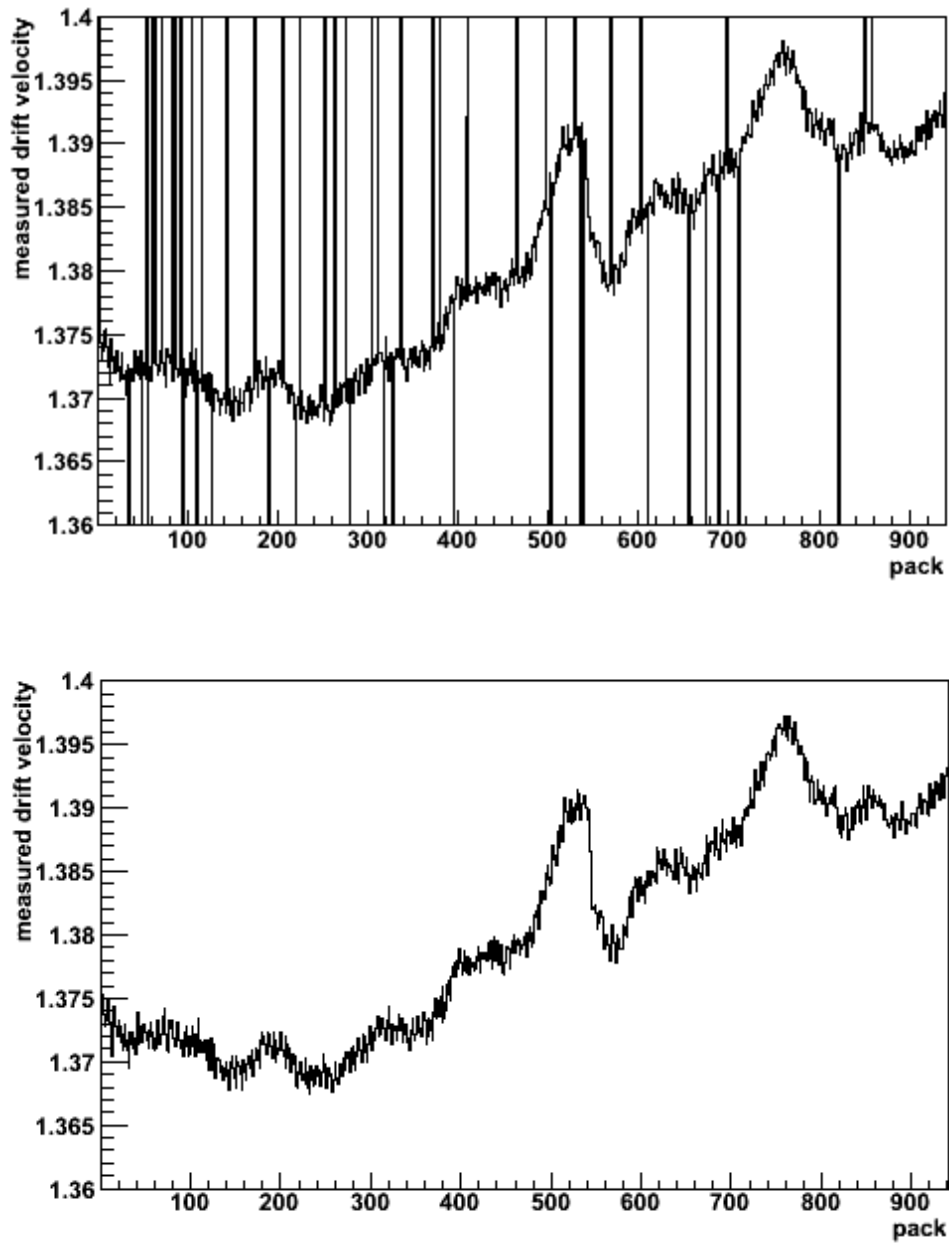


Figure 6.10: Drift velocity spectrum before (top) and after (bottom) applying the software improvements [62].

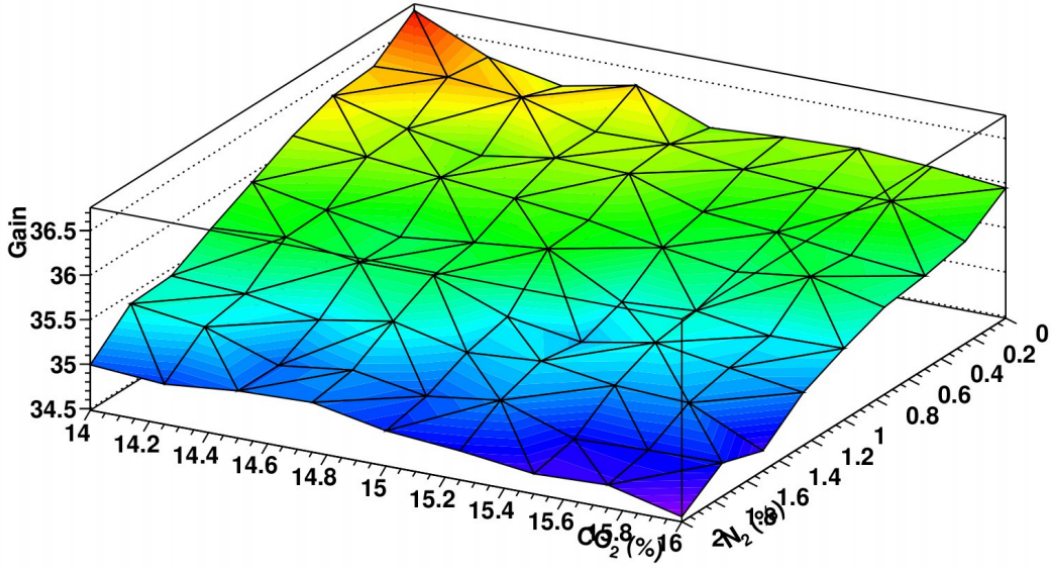


Figure 6.11: Simulated 3D spectrum of the gain vs. N_2 (y) and CO_2 (x) content.

The results for a drift field of 700 V/cm are as follows:

$$v_d = 3.4771 - 0.0190447 \cdot y - 0.114309 \cdot x \quad (6.12)$$

$$G = 40.7141 - 0.748968 \cdot y - 0.298851 \cdot x, \quad (6.13)$$

for a field of 665 V/cm - the actual drift velocity in the GOOFIE - the equations are:

$$v_d = 3.13013 - 0.0158658 \cdot y - 0.102748 \cdot x \quad (6.14)$$

$$G = 40.7447 - 0.676404 \cdot y - 0.299172 \cdot x, \quad (6.15)$$

with $y = N_2$ [%] and $x = CO_2$ [%] [64].

Using these constants with the input values of drift velocity and gain provided by the GOOFIE online application solving two linear equations (6.16, 6.17) leads to the gas composition in the actual TRD gas.

$$v_d(CO_2(\%), N_2(\%)) = P_2^d + P_1^d \cdot CO_2(\%) + P_0^d \cdot N_2(\%) \quad (6.16)$$

$$G(CO_2(\%), N_2(\%)) = P_2^G + P_1^G \cdot CO_2(\%) + P_2^G \cdot N_2(\%) \quad (6.17)$$

The parameters P_j^i correspond to the plane coefficients obtained by fitting the simulated two-dimensional tables. Drift velocity and gain have to be normalized with respect to the initial values of CO_2 (15%) and N_2 (0%) to obtain

6 GOOFIE - A gas quality monitor

the correct values for nitrogen and carbon dioxide. Since the gas density is another issue to be taken into account v_d and G used in the calculations are already corrected for pressure and temperature.

- Remote control of the online application

To make the GOOFIE systems more shifter and expert friendly it was decided to install a program (dim2shell) that can execute scripts on the GOOFIE PC via DIM to be able to (re-)start/stop the online application by clicking on a dedicated button in the PVSS DCS UI. For this purpose a newer DIM was installed, the DIM Name server updated and the actual GOOFIE software modified to use the appropriate libraries. In addition, executable scripts had to be written and placed on the GOOFIE machines in order to be able to control the online application remotely.

- Automation of the power supplies

Motivation

For the time being the GOOFIE power supplies (PS) had always been controlled manually, remote control was not yet possible. Therefore, the voltage had to be ramped up manually in small steps to avoid accidental burning by a transmitted discharge of some of the GOOFIE board channels as has happened before due to unforeseen power-cuts or similar incidents. This means bad reproducibility in voltages and therefore in measured drift velocity and gain. Thus, it was decided to implement remote controlling and monitoring in order to improve and facilitate the operation of the GOOFIE.

Digibox

Since both power supplies (an “iseg” PS for the pick-up voltage, a Heinzinger PS for the field cage) are serial devices, it was necessary to use a port server for the serial-to-ethernet connection to be able to bridge the distance between the PC farm and the devices. A PortServer®TS was therefore chosen since it provides a reliable way to connect any type of serial device over the ethernet. This so-called Digibox emulates a local serial port and is transparent for the communication on the PC. Its IP address had to be configured using DHCP

and the device was then automatically detected on the CERN network with the help of the software provided by “Digi” [65]. A schematic setup of the communication path can be found in figure 6.12.

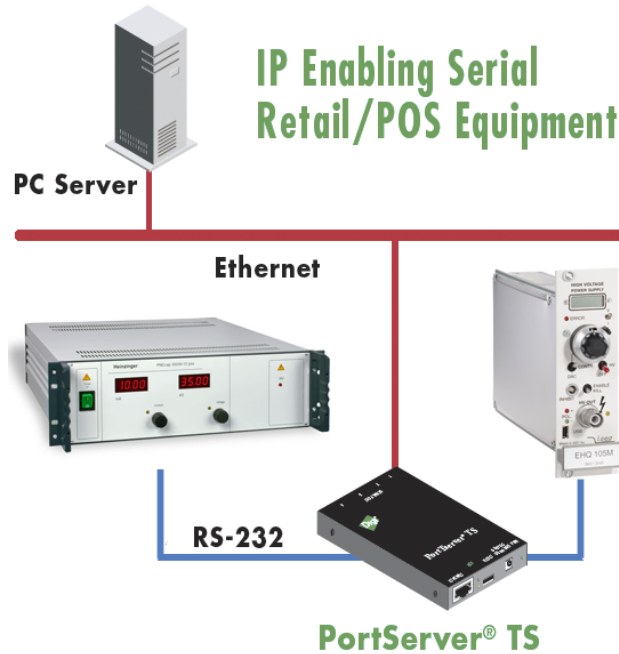


Figure 6.12: Serial-to-ethernet device PortServer®TS from Digi [65] interfacing between a Heinzinger (left) and an Iseg (right) power supply and a PC server.

Software/PVSS

In PVSS a Data Point Element (DPE) for each COM-port is used where all commands are written to which ensures that there is no race condition between two commands since they are processed in a serialized order. A script then sends the commands to the RS232, waits for the answer with a timeout and writes either the read value to the corresponding DPE or sets the status to *disconnected* in case of a timeout. Since the script knows the command it also knows how to interpret the answer. Furthermore, another script connects to the setting-DPEs and exchanges the corresponding commands with the COM DPE. A poll script regularly writes the commands to the COM DPE to poll the actual values of voltage and current. Since these improvements were to be implemented for both GOOFIEs (TPC and TRD), it has been developed in co-operation with the TPC. The working principle of TRD and TPC is similar

6 GOOFIE - A gas quality monitor

but not identical, wherefore this software then had to be modified to fit into the DCS of the TRD. The existing GOOFIE user interface was upgraded respectively. It can be found in figure 6.13 with the controls on the top right.

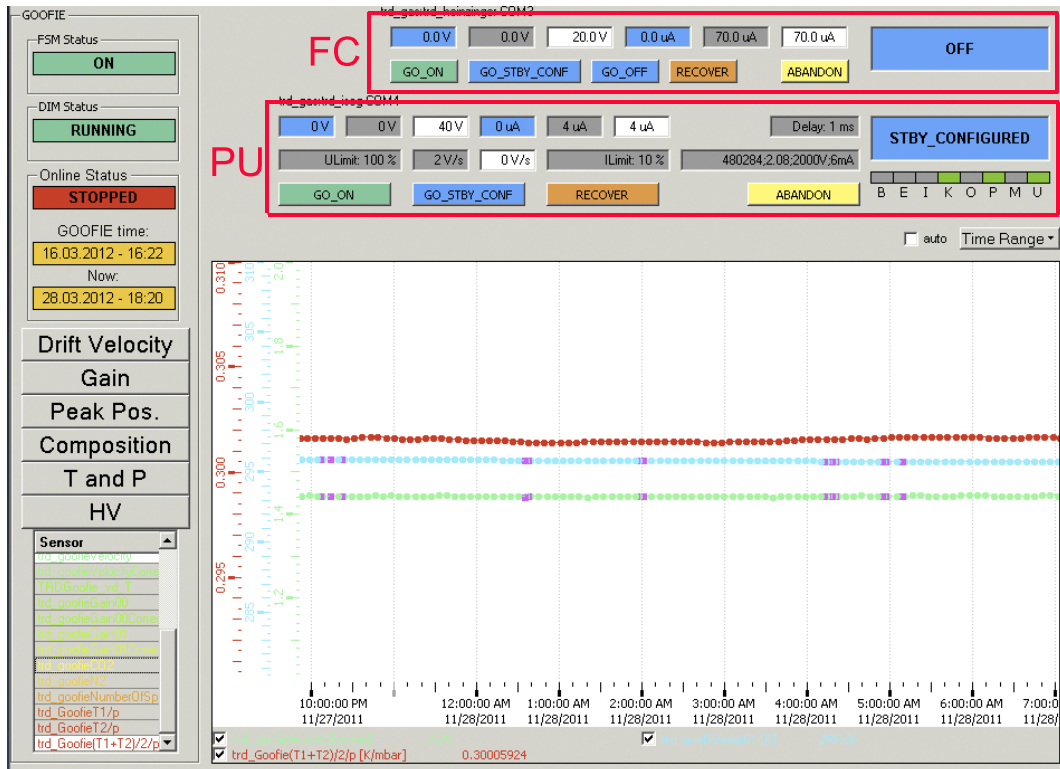


Figure 6.13: PVSS-based UI for the GOOFIE on the operator node of the TRD DCS. Highlighted are the control panels for the pick-up (“PU”) and field cage (“FC”) HV. It is possible to switch the devices on and off, set the desired voltage, ramping speed and maximal, abandon a ramping process or even recover in case a hard-/software problem has occurred.

7 Detector Control System - DCS

The topic of this chapter is the Detector Control System (DCS). The general DCS logic and architecture is discussed, including a description of the process control software it is based on. The next part outlines the DCS of the TRD focusing on its logic and the connection to and between its sub-systems. The TRD DCS user interface is given special attention to since the work of this thesis is mostly dedicated with its renovation and upgrade.

7.1 Introduction

For monitoring, controlling, operating, regulating and acquiring data of the LHC experiments a process control and monitoring system was developed by CERN. This “Detector Control System” (DCS) ensures the safe and correct operation of the experiment providing a user-machine-interface to all experimental devices. The DCS is one of the four “online systems” of ALICE which control the operation of the detector. The other three are the Trigger (TRG), the Data-Acquisition System (DAQ) and the High-Level Trigger (HLT). The Experiment Control System (ECS) is the top level of control connecting these four. Since the whole machinery can be controlled remotely via the DCS, it is possible to operate the full ALICE detector from one work station in the ALICE “control room”. The DCS takes care of the execution of commands, it assures the communication between the different detector components and it provides data archival. It is built on a three-layered logical architecture. Its lowest level - the **field layer** - collects information from the devices and provides services to them using common middleware protocols running on top of TCP/IP as standard for the device communication: **DIP** (Distributed Information

7 Detector Control System - DCS

Protocol) is a client/server protocol developed by CERN to broadcast data between different networks, whereas **OPC** (OLE - Object linking and embedding for Process Control) is a client/server protocol able to broadcast data and receive commands from standard commercial devices. The information collection and sending of control commands from/to sensors and remote devices is done via a number of computers and Programmable Logic Controllers (PLC) or PLC-like devices on the so-called **control layer** [66].

The computers executing the DCS tasks are called Worker Nodes (WN). Typically they do not allow for interactive work which is therefore done on the top level - the **supervision layer** - with the use of a dedicated server, the Operator Node (ON). It provides a set of user interfaces based on a commercial SCADA (Supervisory Control and Data Acquisition) system called PVSS (\rightarrow chapter 7.2). The ON is remotely connected to the individual detector systems on the WNs. Since certain requests like displaying of a big amount of data, retrieval of many alerts, etc., can significantly slow down the execution of the computer, this load must be isolated from the standard DCS operation which is assured by the concept of the ONs. This way, the PVSS systems running on the WNs are not engaged in handling the user requests [67]. Figure 7.1 shows the structure of the control system with the division into its three layers.

The DCS has different access control domains which each user has certain privileges granted for: **observer** (monitoring), **operator** (controlling), **expert** (debugging), **developer** (modifying), **administrator** (administering). In total, there are 20 sub-detectors of different sizes and hierarchical complexities controlled by the DCS. TPC and TRD have the most supervisory control nodes whereas ACORDE or ZDC only have one control computer. In addition, there are several non-detector projects for centralized services like rack and access control, global variables, DIM server, etc., or communication with the external systems (electricity, magnet control, environment and radiation monitoring, LHC services, gas control, etc.). Each ALICE sub-detector has its own DCS, yet all detectors use the common global DCS architecture. In order to operate a sub-detector, the integration and synchronization of all its systems is required. For the TRD they are namely: the low voltage (LV),

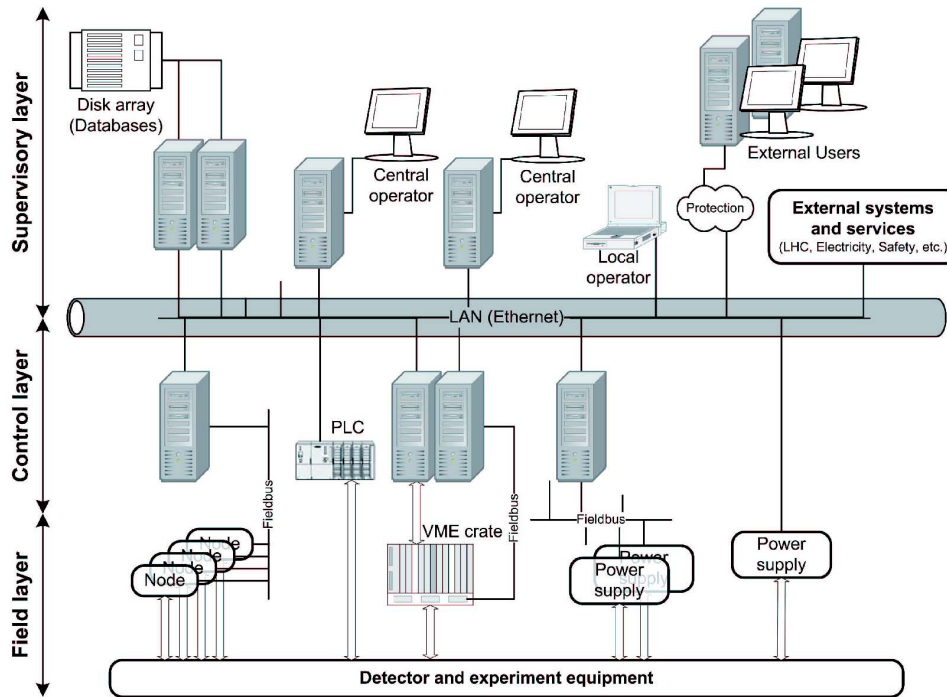


Figure 7.1: Overview of the ALICE DCS structure which is divided into three layers - both physically and logically [26].

high voltage (HV), front-end electronics (FED), power control units (PCU), Global Tracking Unit (GTU), pre-trigger, cooling and gas system, GOOFIE, etc. All the various TRD sub-systems have been defined as “objects” behaving as **Finite State Machines** (FSM). This gives the advantage of structuring the complex TRD as a hierarchical tree of smaller manageable components (objects), each component independent from the others but equally providing the possibility of an integrated control, both automated and user-driven. Since the functionality of each object is described and implemented as an FSM, one can model its behavior in terms of simple standard states like OFF, STAND-BY, CONFIGURED, RUNNING, etc., and actions like GO ON, GO STAND-BY, RECOVER, etc. These objects can be either physical devices like power supplies or abstract objects representing logical entities like detector stacks and layers. In addition, it is possible to group related components that represent the same sub-system (HV, LV, FED, etc) [68].

7.2 PVSS

The detector control systems of all LHC experiments are based on PVSS (Prozessvisualisierung und Steuerungssystem) since it is a very comprehensive object-oriented process visualization and control software including alerting of critical states or exceeded limits, and archiving of data for later initialization, configuration, displaying or analysis [69]. Within PVSS every logic state, measured value, set-point, etc., must correspond to a kind of variable that represents this value within the system. These process variables called **datapoints** (DP) are transferred to the software at the control desk. The DPs are of a **datapoint type** (DPT) that is defined by the structure of the device it is assigned to. This DPT provides a basic “template” to build DPs that are related to the device more easily. Values read from a device are stored in so-called **datapoint elements** (DPE) which can be defined as simple types (boolean, float, integer, etc.) as well as as well as complex types (Binary Large Objects (BLOB), structures, etc.). Certain process-control functions, so-called **configs**, can equally be defined at the DP [68]. Figure 7.2 shows an example of the structure and logic of the DP-concept.

PVSS applications are built of **panels** and **scripts**. Panels are all UIs such as process displays, operation windows, trends or diagrams. They include widgets like text fields, trends or clocks, whose dynamics are controlled by scripts. With these scripts it is possible to parametrize the widgets, i.e. to change the properties of a graphics object as a function of the DPEs. A PVSS internal control script language (CTRL; C-like) is used in these scripts to access data as well as the properties of a graphical object with the help of predefined functions and user-inserted programming code. It is possible to write global panel scripts, whose functions and variables are made available to all widgets in the panel as well as specific, individual widget scripts. Executable modules (UIs, scripts, DPs, etc.) created for an explicit application are called **processes**. Regarding the TRD, one individual project is running on each worker node (trd_gas, trd_hv, trd_gtu, etc.). Each project is built as a distributed project and is included as a sub-project in a main one (e.g. cooling and gas are combined in the project “trd_gas”). A detector project is therefore a highly distributed

architecture composed of several processes, called **managers** (device manager, distribution manager, database manager, control manager, etc.) who communicate via a PVSS specific protocol over TCP/IP. To add, control or configure a device within a project, the JCOP framework provides a so-called **Device Editor and Navigator** (DEN). The device hierarchies can be built here to give a logical structure to the DCS. It is possible to distinguish between the hardware view (physical device), logical entities view (e.g. a group of cooling loops) or the FSM view allocation. One can add user-defined device types but the framework already provides a number of device types with common functionalities, e.g. Wiener power supplies. They communicate through a CAN bus interface and any model that supports the standard Wiener protocol can be operated with the help of this template [70].

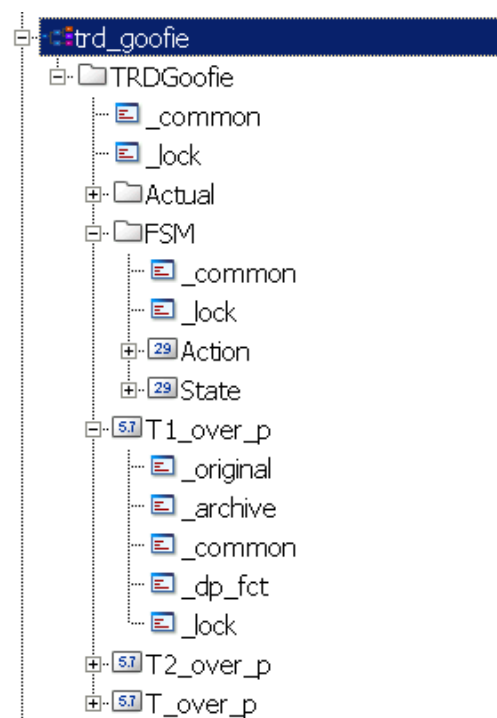


Figure 7.2: The datapoint (DP) concept. “trd_goofie” (1) is a DPT with “TRDGoofie” (2) as a DP. “Actual” and “FSM” (3) are DPE defined as BLOB with “sub-DPEs” (e.g. “Action” and “State” for “FSM”). “T1_over_p” (4) is a DPE defined as a float with several “configs” such as “_dp_fct” (5).

7.3 TRD DCS

The DCS for the TRD follows the same principle of architecture as the central DCS and can equally be divided into the three sub-layers. The field layer includes power supplies, field bus nodes, sensors, etc. One level higher lies the (process) control layer consisting of the worker nodes, PLCs and PLC-like devices, connected to the operator node which forms the supervision layer. Computers and devices are connected to the DCS LAN that runs through all the experimental locations and to standard field-buses where ethernet is used for communication and device control. At present there are nine worker nodes providing collected and processed information to the ON for supervision, maintenance and controlling or sending user commands to the equipment (field layer) [71]. Each TRD sub-system is connected to a specific WN. Some systems like, e.g. cooling and gas, are grouped together on one WN while others, like the high voltage, have two dedicated WNs due to their size. Within the ALICE DCS network the WNs have unique hostnames. The TRD sub-systems and their WNs can be found in table 7.1

TRD sub-system	abbr.	WN
Low Voltage	LV	alitrdown001
Power Control Unit	PCU	alitrdown001
High Voltage	HV	alitrdown002
Front End Detectors	FED	alitrdown003
Global Tracking Unit	GTU	alitrdown004
Pre-Trigger	PT	alitrdown004
Front End Detectors	FED	alitrdown005
<i>general purpose</i>	—	alitrdown006
Cooling	COOL	alitrdown007
Gas	GAS	alitrdown007
<i>FEE services</i>	—	alitrdown008
High Voltage	HV	alitrdown009

Table 7.1: The TRD sub-systems and their dedicated worker nodes.

The concept of finite state machines is mapping a physical device to a limited (finite) number of simple states. It can switch between these states by executing standard commands from an operator or reacting to external factors that make a change of the state necessary. The TRD FSM state diagram is displayed in figure 7.3. A process called **state manager** (SM) takes full control of the physical devices assigned to it. It is in charge of coordinating or synchronizing them, responding to spontaneous changes in their behaviors, etc. It follows user-defined instructions and sends the necessary commands [68].

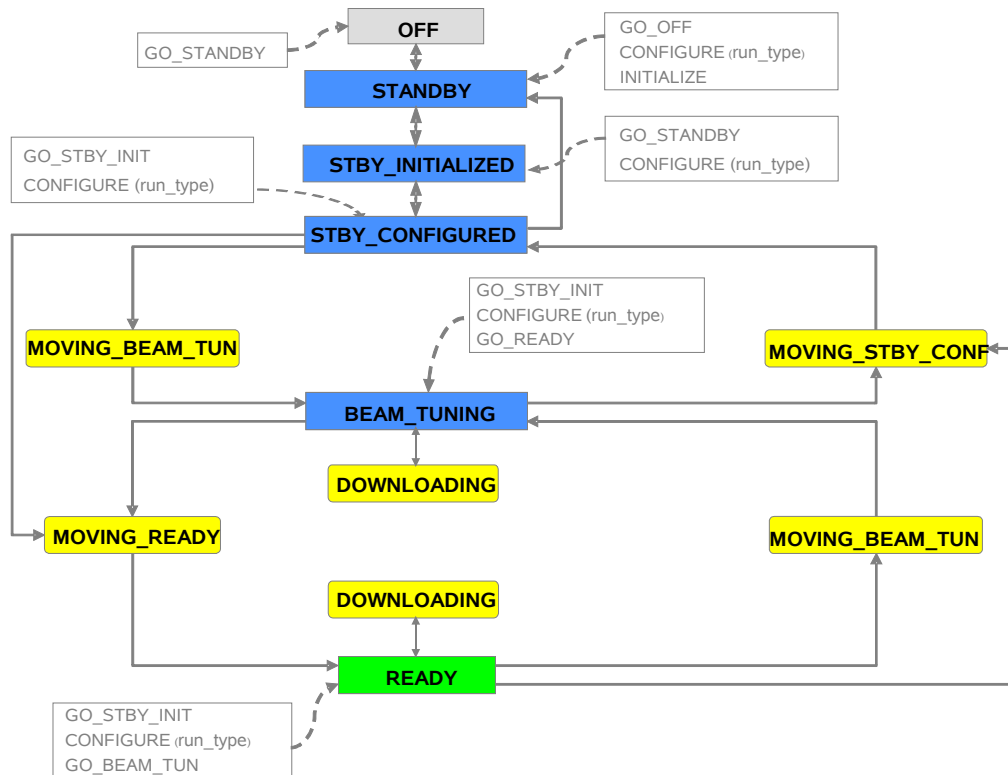


Figure 7.3: TRD FSM state diagram [72].

In the case of the TRD the overall hierarchy is based on the physical devices (supermodules, power supplies, etc.) with the TRD DCS as the main control unit. All sub-levels (nodes) receive commands from this top unit and send their information back to it. Furthermore, the DCS provides an interface between the LHC and the detector to control it accordingly, e.g. avoid damage because of beam loss by bringing the TRD into a safe state. The TRD comprises 18 “control units”, one for

7 Detector Control System - DCS

each SM, which contain all the detector equipment, such as LV, HV and FEE, the pre-trigger, GTU and TRD INFRASTRUCTURE containing the gas and cooling system, GOOFIE, PCU, PT LV and VME crate control. To get an idea of the TRD DCS structure as well as its connection to central DCS and ECS, be referred to figure 7.4.

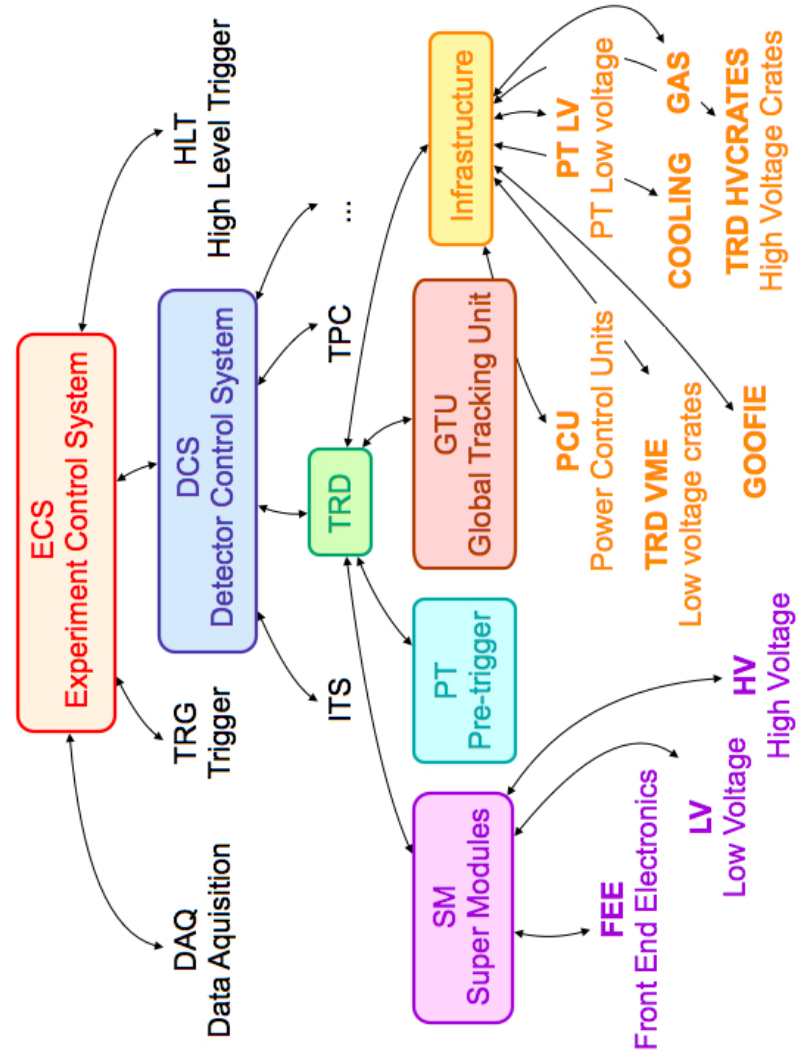


Figure 7.4: Overview of the TRD DCS structure and its connection to the central (ALICE) detector and experiment control systems [73].

7.4 Upgrade Of The TRD UI

Motivation

As described in section 7.2, PVSS provides the possibility to implement a user interface (UI) to supervise, control, operate and monitor a detector remotely. It is generally equipped with several tools that are common to all ALICE sub-systems such as an access control panel, an auxiliary monitoring area with the FSM states of the individual nodes, access to the common alarm panel, help, settings, environment variables, LHC information, etc. However, the FSM hierarchies and monitoring panels (GUIs) are developed by and therefore specific to each sub-detector independently. The GUI of the TRD consists of several panels for monitoring its subsystems and providing the possibility of user operations. The panels have access control requiring certain grants (observer, expert, etc., as mentioned before) for certain operations. In picture 7.5 you can find the TRD FED GUI as an example.

The FSM hierarchy follows a tree-like structure displayed in a browser as can equally be seen in figure 7.5. From the FSM browser, as part of the GUI, it is possible to launch the FSM operation panel from where commands to the FSM objects can be sent. Furthermore, nodes (and sub-nodes) can be taken, released, included, and excluded from there in order to be able to send global commands or restrict an operation to individual nodes.

The hardware structure and communication protocols between the hardware and supervisory level of the sub-systems as well as the controlling, monitoring and implementation into the FSM hierarchy was mainly realized in [68]. To improve the operation of the TRD renovations of the existing (G)UI had yet become necessary. Mainly the design but also some of the structure was modified and further developed as will be described in the following.

Design Renovations and Modifications

A common upgrade to all panels was designed and programmed to provide a user-friendly way to switch quickly between the different sub-systems from the panels themselves instead of having to go via the FSM tree (navigate to the desired node, right mouse click, “view panel”). Therefore, it was necessary to implement buttons

7 Detector Control System - DCS

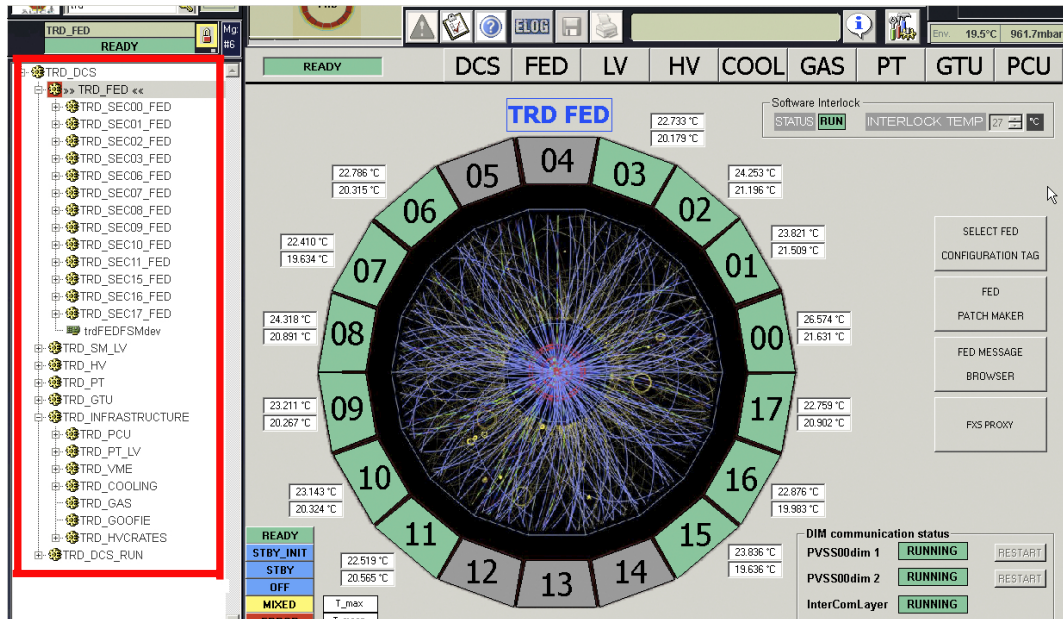


Figure 7.5: GUI for displaying and controlling the TRD front-end detectors (FED). Marked in the red box on the left is the tree-like FSM browser.

common to all GUIs for the top node, nodes and sub-nodes). They can be found on the top of each panel (be referred to figure 7.5 as an example) creating the possibility to navigate from, e.g. the cooling to the FED, with one mouse click. The same principle was introduced to navigate between the different supermodules (within one sub-system) as will be described in more detail using the HV system as an example. The GUIs for the individual sub-systems have also undergone respective modifications. They will be discussed separately on that account.

- TRD DCS overview

In figure 7.6 the first UI [68] of the TRD top node (DCS overview) can be found. The modification ideas included implementation of displaying ALICE global information such as the actual run status, type and number. Furthermore, a color-coded alarms indicator and quick-access to the more detailed alarm-panel was needed. In addition the FSM states of all sub-systems should be visible on this top-node in order to minimize the time of problem finding and solving. With the ALICE-wide implementation of the “super safe” status (lowered high voltage) to which a detector needs to be brought to avoid damage when the

LHC beam is about to be injected, an “emergency button” to ramp down (or up, if already in “super safe” and to be brought to “safe”) the HV of all SMs at the same time with one single action. The last modification was to visibly divide each SM into LV, HV and FED and display the (color-coded) FSM state of each supermodule’s sub-system directly. The present TRD DCS panel can be found in figure 7.6 (b).

- Gas and Cooling System

Since the infrastructure of the cooling and gas systems is common to all LHC experiments, dedicated CERN Departments provide maintenance, support and control applications for most of the equipment. In case of the gas system the main application to supervise and control the system on an expert level is the GCS, developed by the CERN gas working group. However, there is the possibility and need to monitor this system by a general shifter or non-expert. Therefore, a dedicated user interface for monitoring of the states and trend displays of the individual sub-systems’ pressures, flows, etc. was developed and implemented into the TRD DCS. The main UI can be found in figure 7.7 (a).

The ALICE cooling plants are controlled and monitored by an application developed in a joint collaboration between CERN’s technical support department and JCOP. This application can be implemented into each sub-detector’s individual DCS according to the detector requirements. In addition, it provides a common overview panel of the whole detector with all its 18 individual loops (one for each supermodule) supplied by the cooling plant plus the five thermal screen loops shared with the TPC, quick access to several trending plots, displaying of the most important parameters of the cooling plant and control access. The overview panel is shown in figure 7.7 (b).

- GOOFIE

As already mentioned (→ chapter 6), a special panel has been developed for the GOOFIE gas quality monitor. It permits to plot the trends of all data provided by the GOOFIE online application, such as drift velocity, gain, temperature, pressure, etc., either individually or in common trends depending on

7 Detector Control System - DCS

the user's requirements. Furthermore, the two power supplies serving the pick-up and field cage high voltage have been implemented into the FSM hierarchy and are remotely controllable (through RS232 and the mentioned "digibox") for precise setting of the voltages and convenient displaying of the voltages and currents. The communication scripts and panels have been developed in close collaboration with Ulrich Frankenfeld from the TPC DCS experts. Furthermore, the UI (figure 7.8) displays the FSM, DIM and online status of the GOOFIE itself as well as the states of the power supplies, respectively.

- FED

To improve the efficiency of monitoring and operation of the TRD's FEDs it was requested to implement temperature displays for all sectors (average and maximum), a status panel for the ICL, the possibility to restart the two DIM servers and quicker access to the FED configuration tags, patch maker, message browser and FXS proxy. Furthermore, the software interlock and DIM server status displays were moved from the individual sectors to the overview panel which can be found in figure 7.9.

- HV

The HV overview panel of the whole TRD can be seen in figure 7.10 (a). The main improvements are quick-access to each individual sector by clicking on its dedicated object on the main panel, displaying of DIM, HV server and crate status, as well as trending plots of the anode currents and two 'emergency' buttons for switching off or bringing into stand-by the HV of the whole detector in one action/mouse click. The HV control and monitoring panel of an individual supermodule can be found in figure 7.10 (b). The main modification for this sub-system was the division of anode and drift into two individual sections with tabs for the voltages, currents, and FSM states of each SM chamber. These values are displayed with color-coded indicators. Furthermore, it is possible to access individual trending and control for each chamber by clicking its indicator opening another panel. In addition, a tab for indicating the voltage behavior during a conditioning test has been implemented to the anode panel. As mentioned earlier, quick switching between the individual SMs

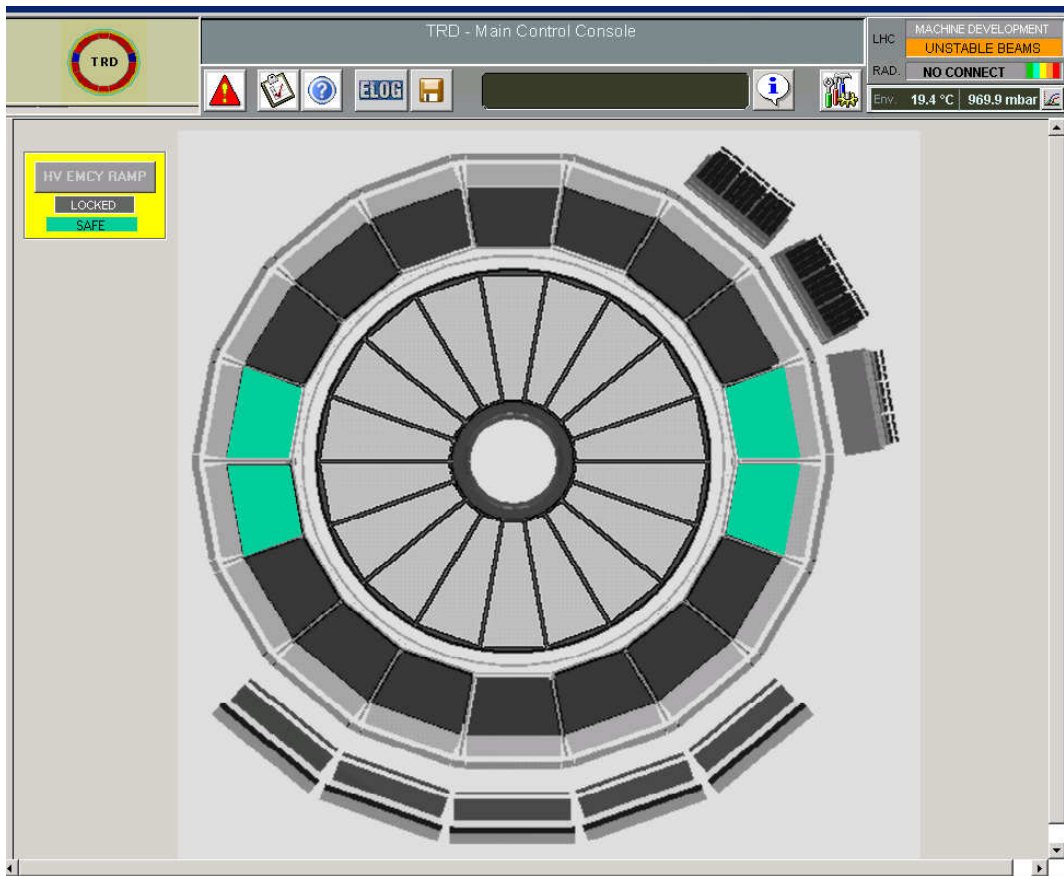
concerning one sub-system, e.g. from the HV of SM01 to the HV of SM02 (see +/- buttons on the top left in figure 7.10 (b)), as well as switching between different sub-systems of the same SM, e.g. from the HV of SM01 to the cooling of SM01 has been implemented. Furthermore, it is possible to directly access the overview panel of any sub-system from any sector (see the top of figure 7.10 (b) for both).

- LV, PCU

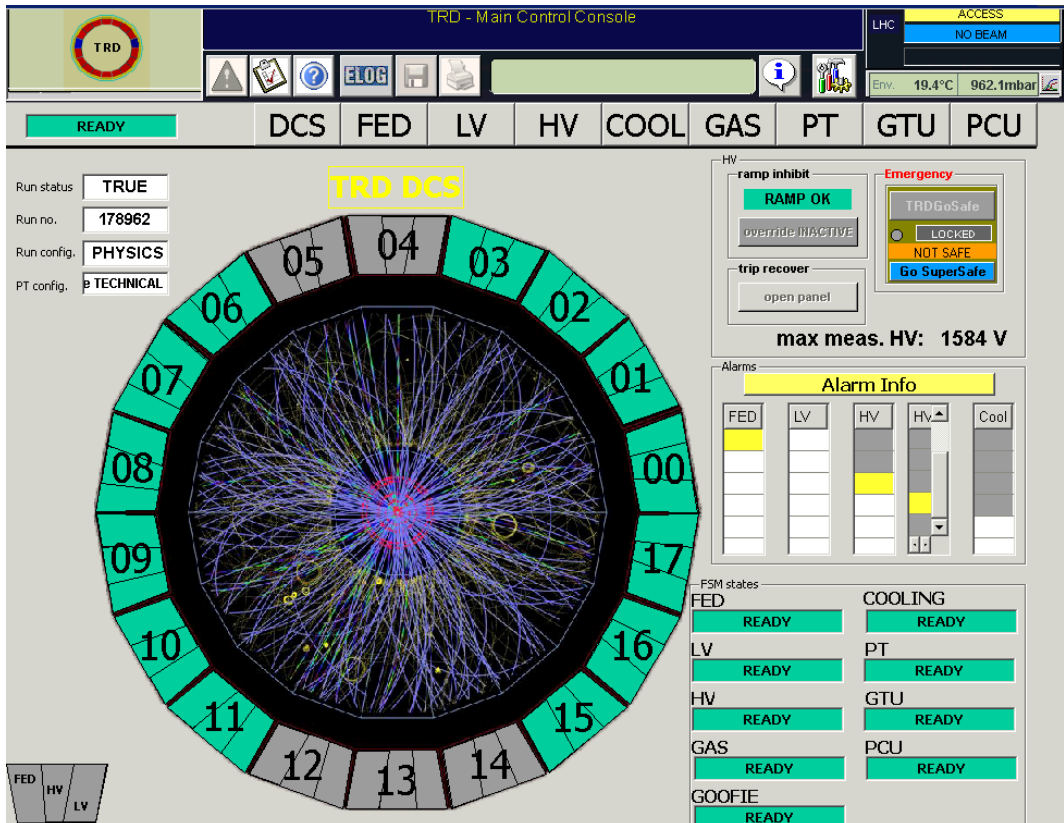
The low voltage system of the TRD provides LV power not only to the SM FEE but also to the power control unit, power distribution box, global tracking unit and pre-trigger. In the FSM hierarchy, the LV system for the FEE belongs to each SM individually while the LV for PCU, PDB, GTU and pre-trigger are listed in the infrastructure. However, for convenience and efficiency a quicker access to these sub-system via the LV overview panel was implemented. Furthermore, each sector was equipped with an indicator of its digital 3.3 V power and divided into the three levels of LV supply (two chamber layers each: 0+1, 2+3, 4+5). In addition, it is now possible to switch the whole LV off with one click, load the FSM recipes to all sectors and monitor the OPC server status (see figure 7.11 (a)).

The PCU and PDB build the power control system providing LV power independently to each DCS board via one PDB located at the end-cap of each SM. Therefore, they are the first systems to be powered up and configured at TRD start-up which makes it mandatory to have an efficient monitor and control of the devices. The PDB consists of a common power input which is distributed to 30 channels each controlled by a Field Effect Transistor (FET) as switch. The PDB primary power line is provided by a single LV channel powering two PDBs. An overview panel for the PCU was implemented to show the channel and PDB states for each SM individually, DIM, PCU and watchdog timer states and to provide the possibility to switch on/off all supermodules at the same time and an overview of the LV power. Furthermore, each SM had to be accessible and controlled as a unit, layer-wise, stack-wise and even as each DCS board on its own (see figure 7.11 (b)).

7 Detector Control System - DCS



(a) Monitoring panel of the DCS top node as developed in [68].

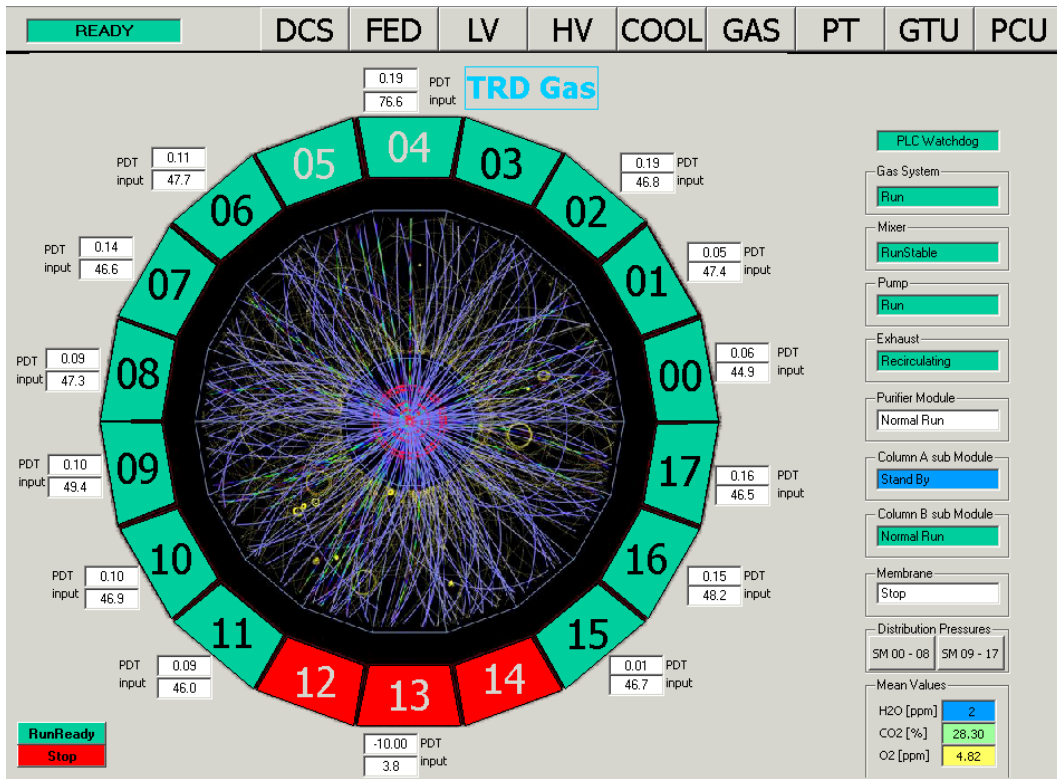


118

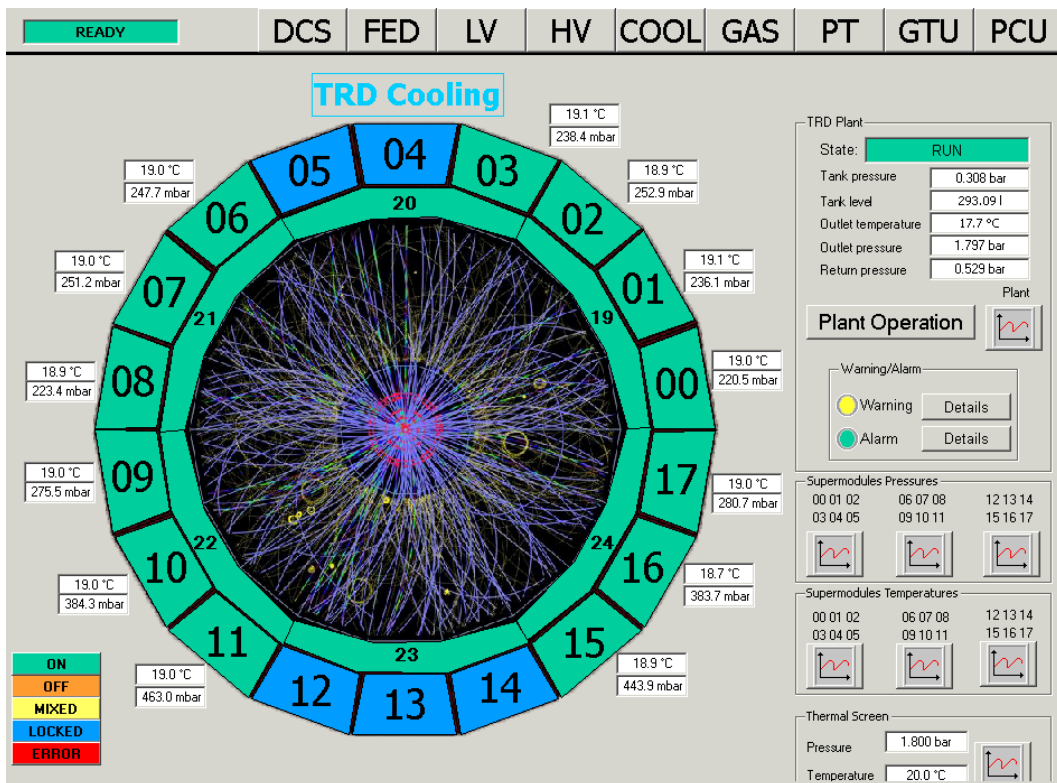
(b) Actual monitoring panel of the DCS top node.

Figure 7.6: Comparison of the former and recent DCS top node.

7.4 Upgrade Of The TRD UI



(a) GAS



(b) COOL

Figure 7.7: Monitoring and control panels of the gas and cooling systems.

7 Detector Control System - DCS

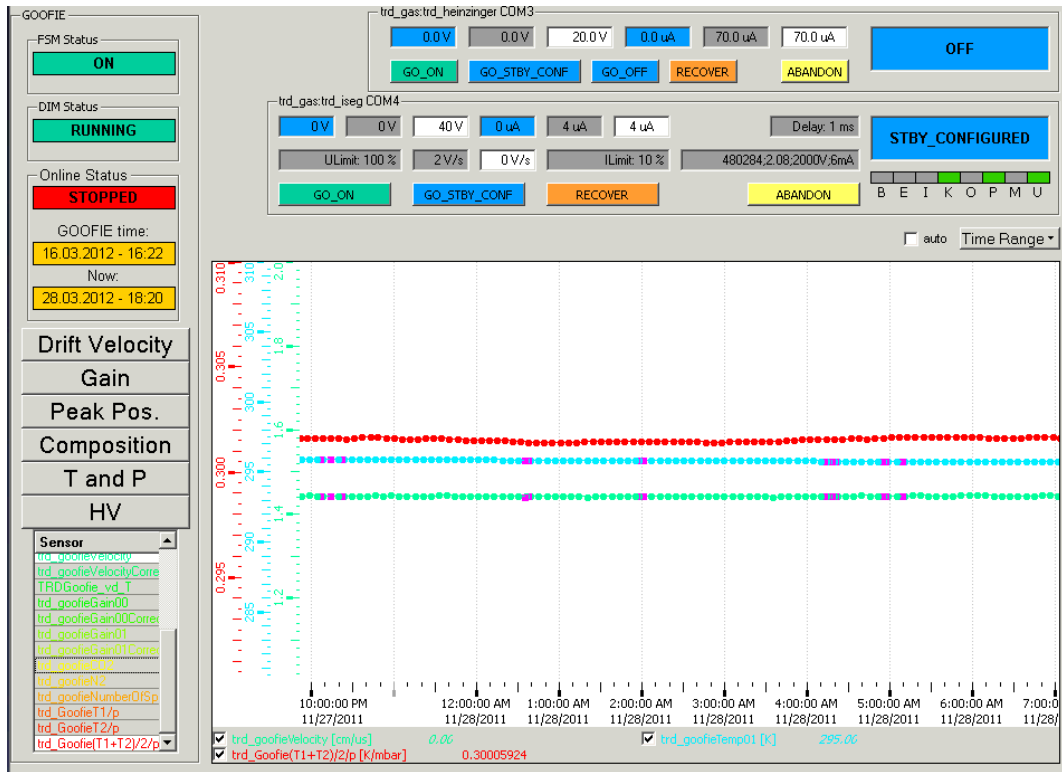


Figure 7.8: GUI for monitoring and operation of the GooFIE.

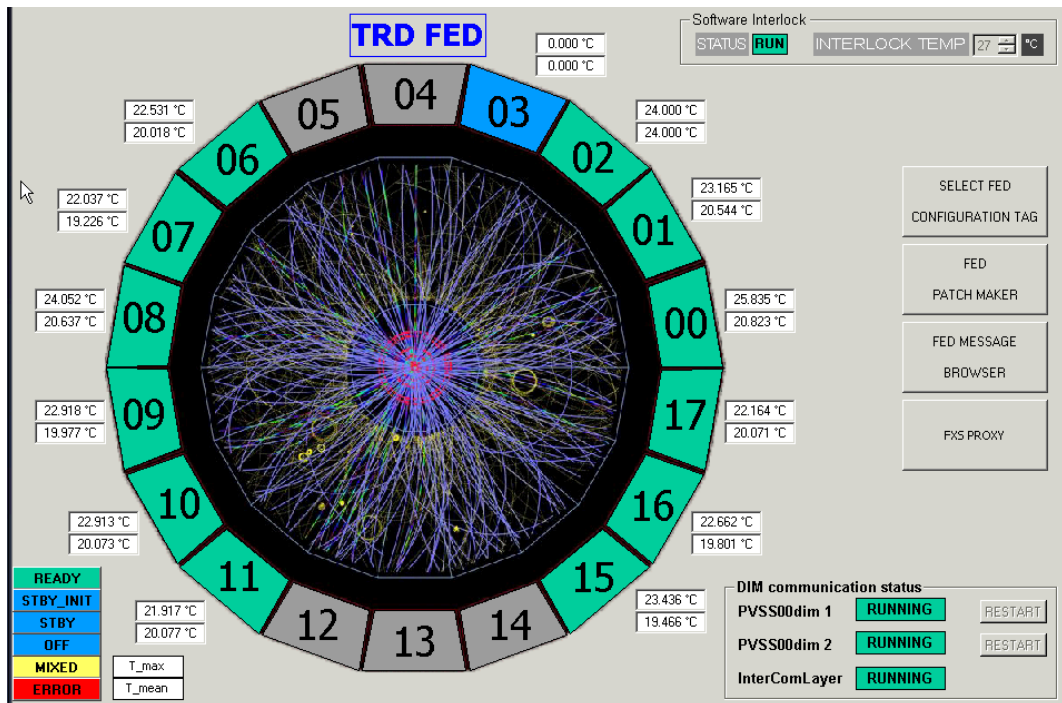
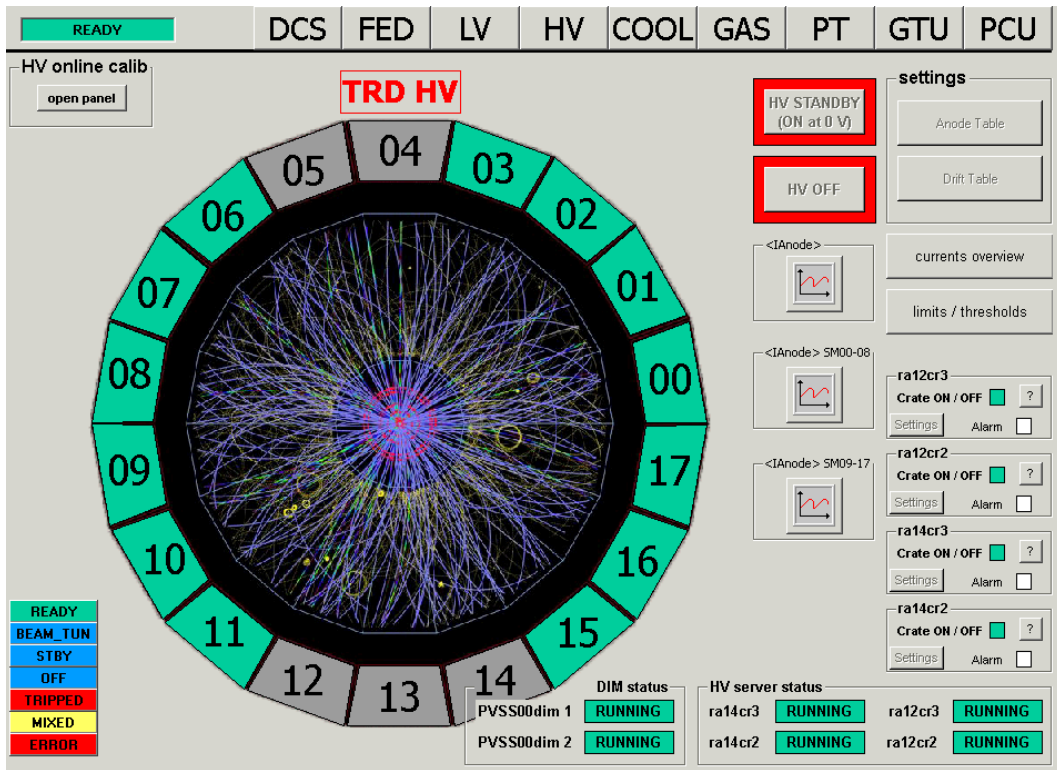
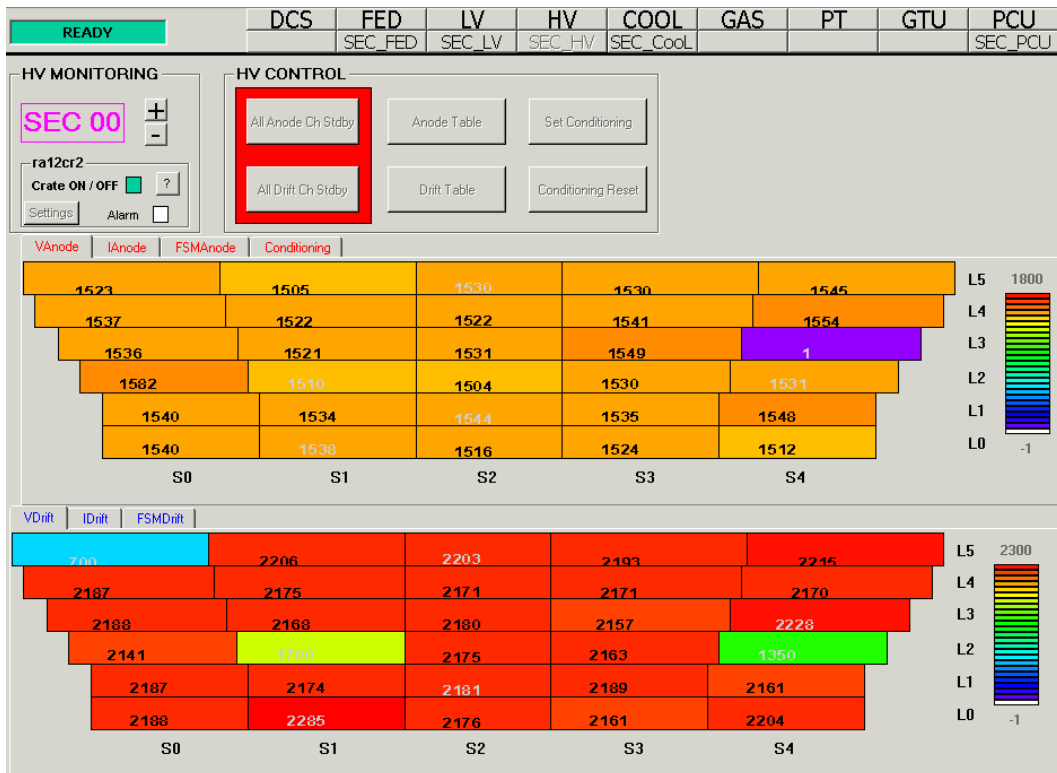


Figure 7.9: FED overview panel.



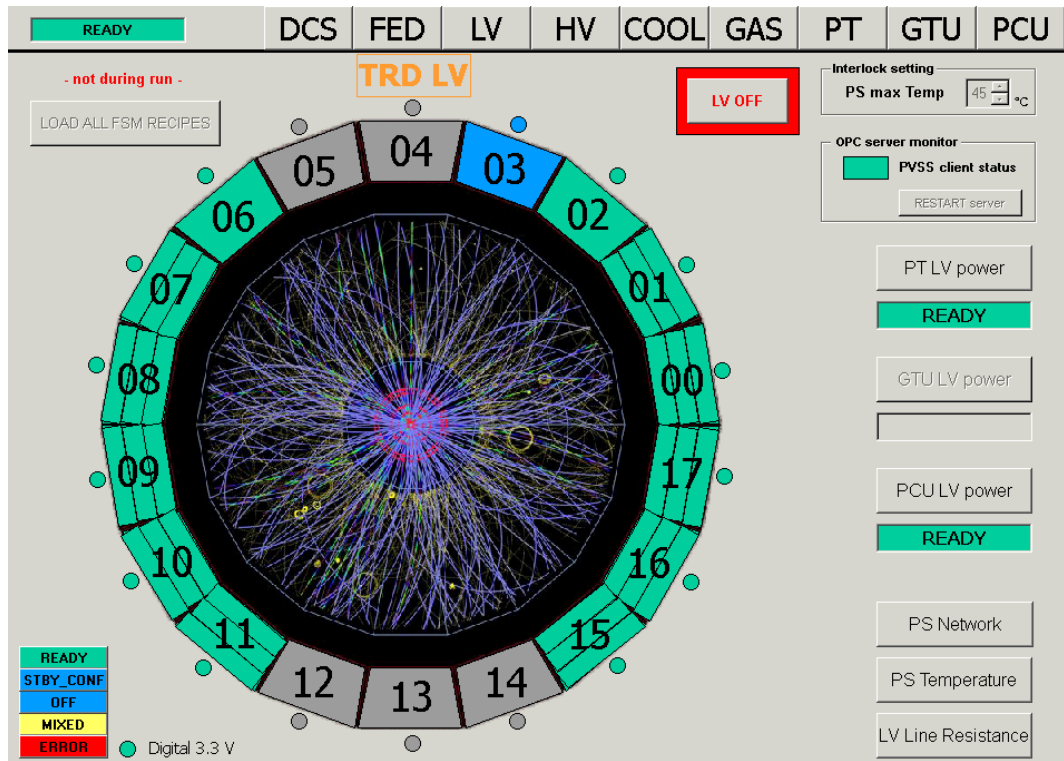
(a) HV



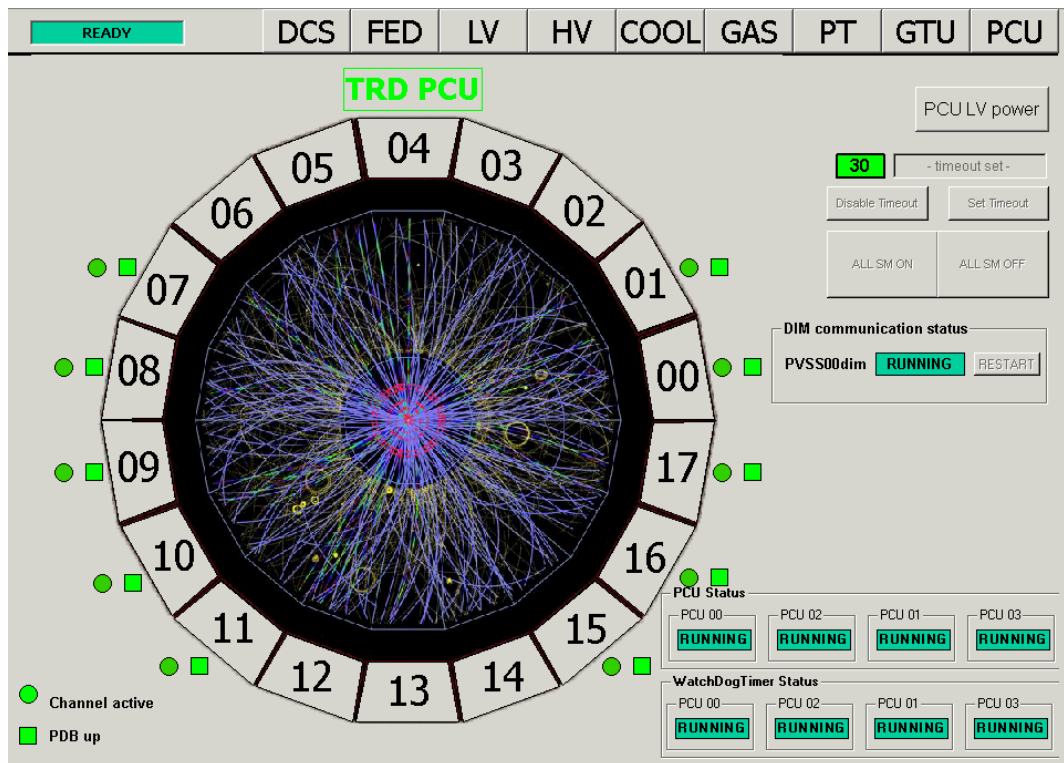
(b) SM HV

Figure 7.10: Monitoring and control panel of the HV of an individual SM.

7 Detector Control System - DCS



(a) LV



(b) PCU

Figure 7.11: LV and PCU.

8 Read-Out Of The TRD Pre-Trigger System

Since at present only final trigger decisions and monitoring results (counters) are being readout, it was proposed to implement a hardware concept to also acquire all data necessary to simulate and predict full pre-trigger functionality and to verify its proper operation. The idea of this new module called PIMDDL (Pre-trigger Interface Module Detector Data Link) had to be further studied and developed. After finalization of the concept and construction of the hardware at the University of Heidelberg, functionality tests were performed at CERN/point 2. This chapter provides an introductory insight into the ALICE trigger and TRD pre-trigger system leading to the studies and tests carried out.

8.1 The ALICE Trigger System

In order to be able to select different event types it is necessary to have efficient triggers. A trigger is a logical signal which starts data recording or activates data read-out. There are multiple trigger levels within which an event is either accepted, so the data is processed or it is rejected which leads to discarding the data. The main challenges lie in the precise definition of suitable trigger criteria and to evaluate them on a short time scale to be able to distinguish between time-critical signals. The precise investigation of physics is based on high statistics. Thus, it is eligible to select/enhance rare event types as much as possible within the limits of read-out, recording and analysis capabilities. Frequently present event types, on the other hand, are to be discarded or downscaled, but still taking specific needs into account,

8 Read-Out Of The TRD Pre-Trigger System

e.g. keeping minimum bias samples. This principle allows for a substantial reduction of the data volume and adjustment of the event samples according to the read-out rate limited by the slow detectors without losing important data.

The ALICE **Central Trigger Processor** (CTP) - the core of the trigger system and decision maker - can generate three levels of hardware triggers, called L0, L1 and L2a/L2r, based on

- 2 LHC timing signals
(40.08 MHz LHC bunch crossing clock and 11.246 kHz orbit signals)
- 60 trigger inputs from the ALICE trigger sub-detectors
- 24 BUSY inputs, one from each read-out sub-detector.

As afore mentioned, the difference in the read-out time of the sub-detectors as well as their time needed until they can provide a higher level trigger decision is the reason for the three level hierarchy. This allows the system to read out the data from faster detectors, while slower detectors are busy with reading out the data from earlier events. There are 50 defined combinations of input signals and trigger **veto**s for each level of hardware trigger, so-called **classes**. A class becomes active following a pre-defined combinatorial logic. There are 24 inputs for an L0 trigger decision, 20 inputs for L1 and 6 inputs for L2. The logic to treat each of the 24 read-out detectors individually would yet be too sophisticated, wherefore they can be grouped unrestrictedly (and with overlapping use) into a maximum of six dynamically partitioned independent **clusters**. Each cluster can be associated with an arbitrary number of trigger classes but each trigger class can only be linked to one cluster. If there is at least one class of a cluster active (logical OR of outputs coming from the classes), a cluster becomes active and sends the corresponding trigger signals to its detectors. In other words: a cluster can take the information from several classes as an input and send its trigger decision/output to the group of assigned sub-detectors. This concept allows for parallel decisions at each level which means that the different groups of detectors can read out different events at the same time [74].

L0

The L0 trigger class condition is formed from all the 24 L0 inputs, two scaled-down BC clocks and 2 random triggers. The two BC inputs are pulses of 25 ns with a programmable interval between the pulses in a range from 0 to ≈ 25 s, synchronous with the BC clock. The two random triggers are arbitrary patterns of 25 ns pulses, equally synchronous with the BC clock. The last trigger input to be taken into account for an L0 decision has to arrive at the CTP $0.8 \mu\text{s}$ after an event. The L0 output is then generated in less than $0.9 \mu\text{s}$ and will arrive not later than $1.2 \mu\text{s}$ after a collision at the detectors within the relevant cluster. None of the detectors in this cluster should be BUSY at the start of a L0 trigger but all be ready to take data. As soon as the L0 trigger is received, the detector will go BUSY and maintain this state until it is able to take data again.

L1

$6.5 \mu\text{s}$ after an L0 trigger the detectors expect the L1 trigger. The last of the 20 possible inputs must therefore arrive within $6.1 \mu\text{s}$ and the L1 trigger decision made at $6.2 \mu\text{s}$, since the decision time should not exceed 100 ns. The trigger is associated with an L1 message (containing the event ID) which is sent right after the L1a (accept). In case an event is rejected on L1, no L1 signal is issued which means that the *absence* of the L1 signal after a fixed number of clock cycles is used as an “L1 reject”.

L2

The drift time of the TPC - the slowest read-out detector - is $88 \mu\text{s}$ wherefore the L2 trigger must arrive later than this but before $500 \mu\text{s}$ have passed. Therefore, the last trigger input is taken from the CTP at $87.6 \mu\text{s}$ and the trigger issued at $87.7 \mu\text{s}$. Either an L2a (accept) or an L2r (reject) is generated by an event that has passed the L1 trigger decision. L2r is indicated by a word, while L2a is associated with a message giving additional information. After an L2a the data from the sub-detector(s) is sent to the High Level Trigger (HLT) which will be explained in more detail later. An L2r will discard any L0 and L1 that was generated before.

Vetoos

There are several reasons for the CTP to discard events, i.e. no L0 is being generated. These vetoos can be triggered by

- the CTP being busy due to a DAQ problem, data overload etc.,
- a signal arriving within the dead-time of the CTP (when an L0 trigger input had arrived at the CTP, it cannot process another input for the next 1.6 μ s),
- at least one read-out detector in the cluster being busy reading out an event, not able to accept another one yet,
- the L0 trigger input not being associated with the active class,
- the test class L0 (when a calibration (software) trigger arrives at the same BC as an L0 trigger input, it is ignored),
- the data acquisition system (DAQ) being busy,
- an event not being in the so-called BC-mask (it is possible to define "valid" BCs in the orbit where triggers are expected),
- the **Past-Future Protection** (PFP) - a programmable time interval around a trigger that will reject events too close to each other.

The PFP prevents events from being piled-up or overlapping in the detector(s). Depending on whether the LHC is circulating protons or lead ions, it can be used in two different modes. Pb-Pb: The PFP circuit monitors the number of interactions, classified according to multiplicity. Pile-up of two central (high multiplicity) events will veto the trigger, while pile-up of an event with peripheral (low multiplicity) events is tolerated up to some programmable level. pp: Since the multiplicity is much lower compared to Pb-Pb, the number of separate primary vertices resulting from pile-up are more important than the number of tracks. Therefore, there are two different time windows for the number of interactions, one corresponding to the TPC ($\pm 88\mu$ s), one to the inner tracker ($\pm 10\mu$ s), due to the different pile-up tolerance in these two detector systems. The only veto for L1 and L2, apart from no trigger input, is PFP [74].

As mentioned in chapter 7, the ECS configures and controls the CTP. Its read-out

is provided to the ALICE DAQ with detailed trigger information for each L2a-event and it also generates a so-called **interaction record** which is a list of all BCs in which the interaction signal has been detected (= CTP read-out) [75], [74]. The design layout/context diagram of the CTP can be seen in figure 8.1.

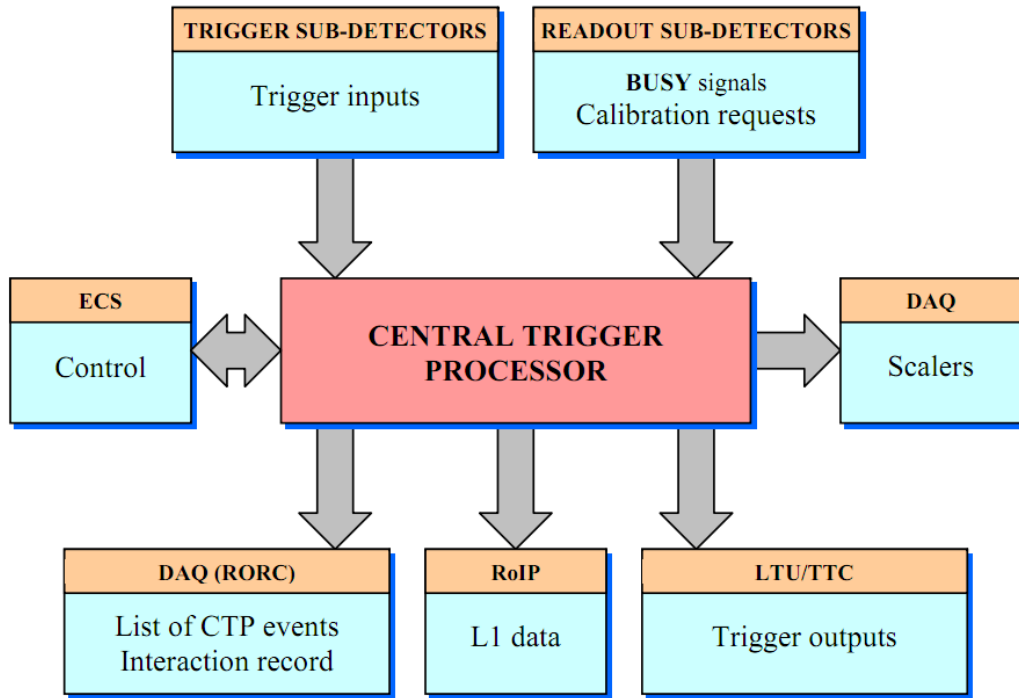


Figure 8.1: The context diagram of the ALICE CTP [75].

The hardware of the CTP consists of several 6U VME¹bus-compatible boards of eight different types: one board for each of the three trigger levels (L0, L1, L2), one for BUSY handling, one for the interface logic (INT) between the CTP, DAQ (via Direct Data Link - DDL) and RoI-processor (Region of Interest-processor) which allows segmented read-out of the sub-detectors, an I²C board (Inter-Integrated Circuit board) which monitors and transmits temperatures and voltages on the CTP boards and several boards for the fan-in and fan-out logic (FO) which, furthermore, are connected to the Local Trigger Unit (LTU) for the individual detectors (LTU described in more detail later). The front panel connections to the CTP crate in-

¹VERSA Module Eurocard bus - a computer bus standard. VMEbus cards exist in three standard heights: 3U, 6U and 9U where 1U = 1.75 inch

8 Read-Out Of The TRD Pre-Trigger System

clude timing, orbit, and busy signals via the BUSY board, trigger inputs, and CTP outputs with DDLs (Detector Data Links) via the INT board. Internal connections are established via a custom backplane which plugs into the user-defined pins of the VME J2 connector. All signals are transmitted as LVDS (Low-Voltage Differential Signaling). The connection is (physically) made with a 16-pin IDC connector and an 8-twisted pair flat-cable. On both the FO and the LTU boards, the connector is mounted on the front panel. A single FO board provides the connections to four LTU boards which correspond to four sub-detector partitions. A layout of the CTP VME can be found in figure 8.2 [75].

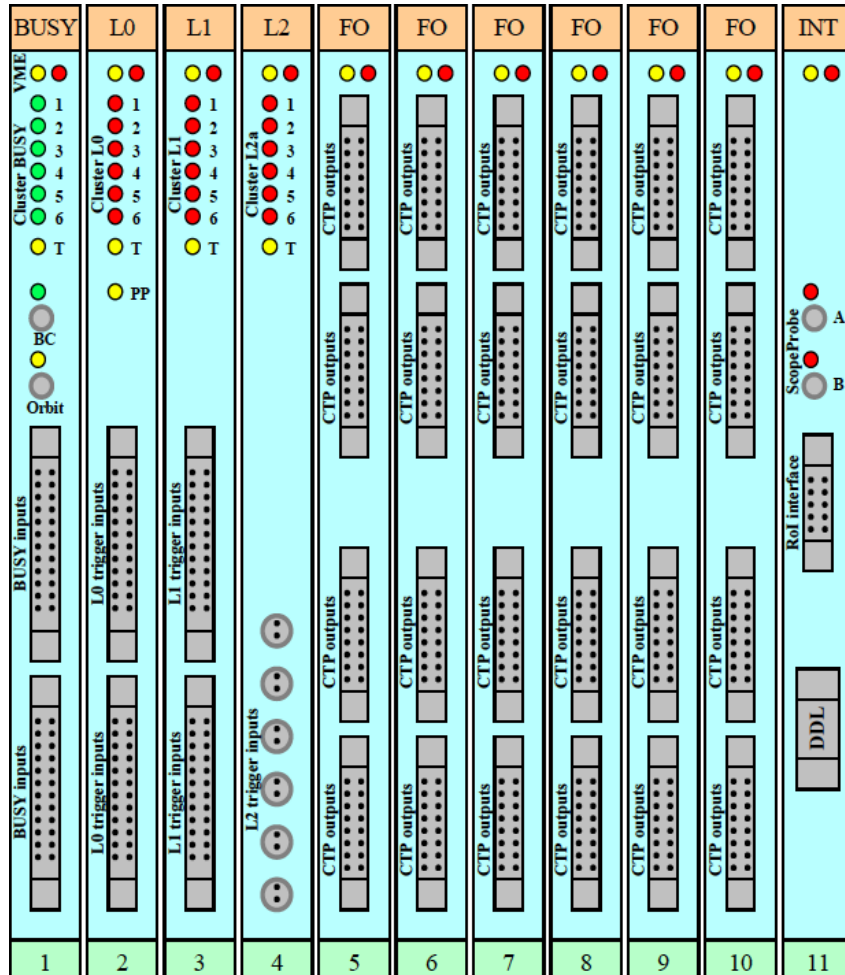


Figure 8.2: The CTP boards in a VME crate. 1 - 4: trigger inputs, 5 - 10 trigger outputs transmitted to the sub-detectors via the LTU, 11 interface to DAQ (via DDL) and RoIP [75].

8.1 The ALICE Trigger System

The **Local Trigger Unit** (LTU) serves as a uniform interface between the CTP and the (sub-)detector read-out electronics. It is a 6U VME board very similar to the other CTP boards in order to maintain the concept of a uniform interface throughout ALICE to simplify system updates/upgrades/modifications etc. The LTU builds the link the CTP and an LHC-wide used system dedicated to delivering individually addressed as well as broadcast signals to many destinations: the **TTC** (Timing, Trigger and Control). The **TTCmi** (machine interface) distributes the bunch crossing clock (TTC-CLK; 40.08 MHz) and the orbit clock (11.246 kHz) - the timers coming from the LHC itself. The “answers” coming back from the sub-detectors to the CTP (via the LTU) are their BUSY signal and the trigger inputs. In order to achieve the highest synchronization precision there is a scheme whereby two time-division multiplexed data channels transmit the needed information. The so-called “A-channel” is reserved for the L1a, delivering a one-bit decision for every bunch crossing from the detector to the TTC. The “B-channel” is used for trigger messages (L1M, L2a, L2r) and other commands supporting up to 16,000 receivers per distribution zone, each associable with up to 256 internal and external subaddresses. The transfer from the detector to the TTC is carried out with the help of the LTU which receives these information and converts them into a TTC-compatible format. Each ALICE sub-detector has a TTC-partition containing an LTU, a TTC VMEbus Interface (TTCvi) and a TTC Laser Transmitter (TTCex). Three VME system boards form a TTC partition. An overview of the CTP partitions can be found in figure 8.3. Furthermore, the CTP formats and transmits its read-out and the interaction record data (i.e. a list of all the bunch crossings in which the Interaction signal has been detected) to the DAQ via the optical DDL. For improving the offline monitoring and analysis of trigger efficiencies the CTP can additionally send the status of the L0 inputs to the DAQ (via a differential LVDS-cable) every time an L0 trigger is sent. The hardware setup of the trigger system can be found in figure 8.4. The CTP is located in the middle with the sub-detector interfaces and TTC electronics racks connected to it [74].

8 Read-Out Of The TRD Pre-Trigger System

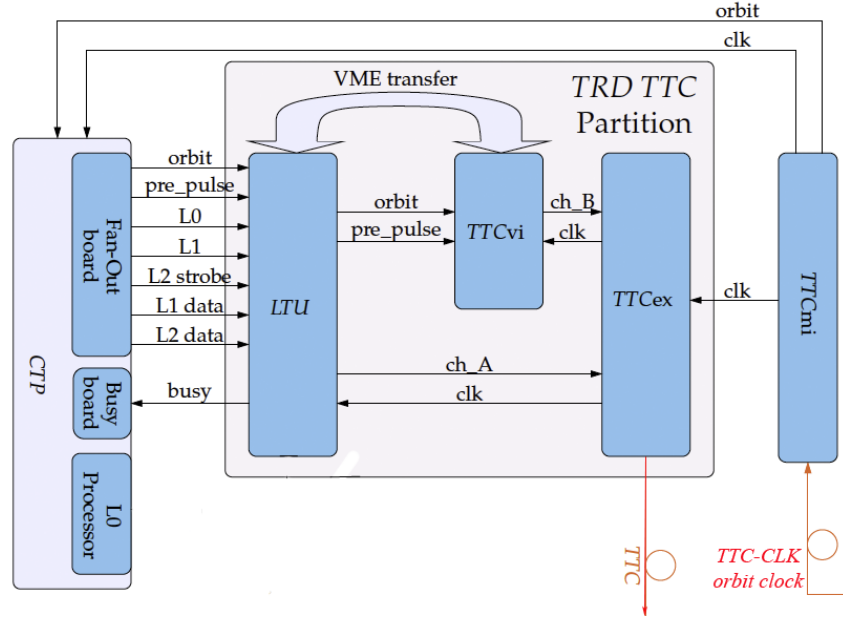


Figure 8.3: A block diagram of the ALICE trigger system [76].

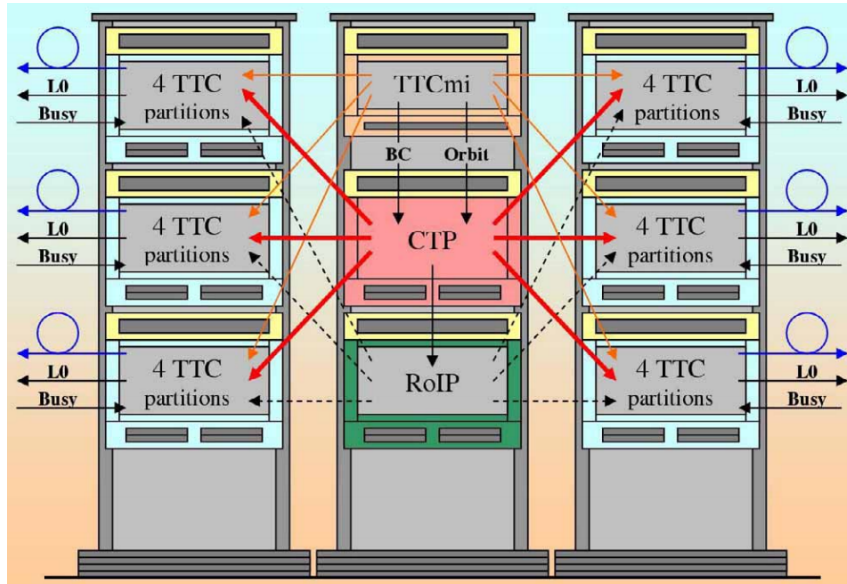


Figure 8.4: Layout of the ALICE trigger system. Its location in the ALICE cavern being underneath the muon spectrometer [27].

After the three hardware triggers (L0, L1, L2) there is a fourth (software) trigger stage: the **High Level Trigger** (HLT). It is a large computing cluster that can directly access the data of the sub-detectors. It reconstructs and analyses the collision data online and decides whether an event should be rejected or stored permanently. It is therefore the last trigger stage of the experiment and supposed to reduce the read-out data following three steps: triggering on interesting events, selecting the RoI, compressing the data without losing the contained physics [76].

8.2 The ALICE Data Acquisition System

The DAQ handles the data flow from the detectors to the permanent data storage in the CERN computing center (CC). As already mentioned above, the ALICE trigger and DAQ system are intertwined in a sophisticated architecture. This trigger decision is distributed to the FEE of each detector via the corresponding LTU and the TTC. If the decision is positive, over 400 optical DDLs transfer the data from the (sub-)detectors to the Local Data Concentrator/Front-End Processors (LDC/FEP) - a farm of 300 individual computers. Two DDL interface units are implemented for this purpose: the Source Interface Unit (SIU) at the FEE and the Destination Interface Unit (DIU) at the LDCs. All the arriving information are checked for data integrity and then processed and assembled into sub events which are sent to one of the 40 Global Data Collector computers (GDC) for event building. 20 Global Data Storage Servers (GDS) are responsible for storing the data locally before their migration and archiving at the CC. There is a dedicated distributed process-oriented software framework called DATE (ALICE Data Acquisition and Test Environment) that manages this data flow between the different DAQ nodes (LDCs and GDCs). DATE consists of several processes executed on every node, depending of its role in the data acquisition. An overview of the DAQ architecture can be found in figure 8.5 [77].

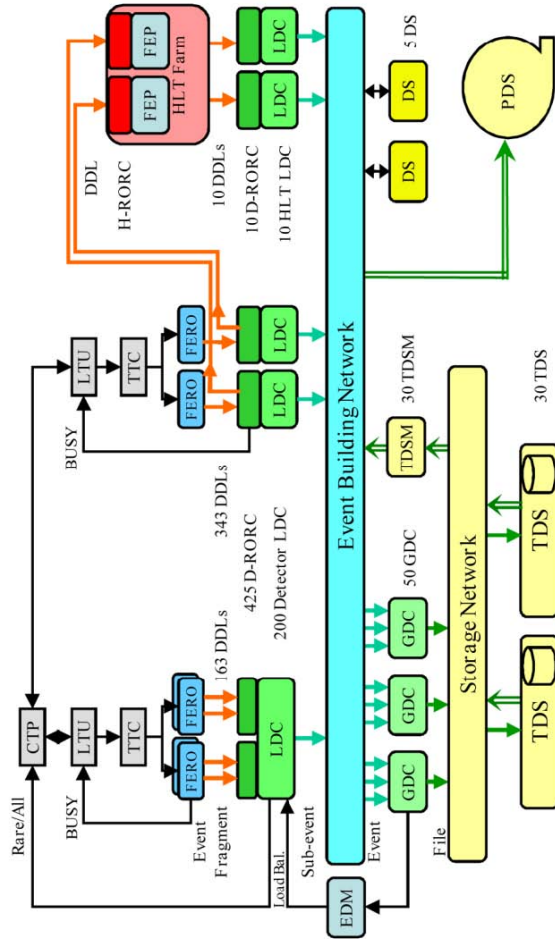


Figure 8.5: The architecture of the ALICE DAQ; The CTP selects the events, initiates the detectors' read-out via their LTUs and the TTC, and synchronizes the experiment with the LHC clock. The DAQ takes care of the data flow from the detector FEEs to the permanent storage, and of the control of this data flow using more than 500 DDLs. The HLT filters the information by quality to keep the amount of data on a reasonable level [77].

8.3 The Pre-Trigger System

The TRD has a very high granularity (1.1 million pads) in order to account for the required momentum resolution and pion rejection in highest multiplicity events. To handle this high granularity a large amount of read-out electronics is needed, which causes a lot of heat while running. Therefore, it is necessary to keep the TRD's electronics in an energy-saving stand-by mode as much as possible. However, this makes it necessary to have an early wake-up signal for the electronics shortly after a collision to profit from the TRD's fast triggering capability. This wake-up signal comes from the fast forward detectors (T0, V0) and the TOF detector or is alternatively derived from the LHC bunch counter (BC). This **pre-trigger** (PT) allows for the 75,000 MCMs of the TRD's FEE to be woken up in time to take data when an interesting event occurs. If no L0 trigger is seen $1.2 \mu\text{s}$ after an event, the data is discarded and the FEE returns to its stand-by mode. In order to generate the signal before the ALICE L0 trigger and therefore keeping the latency on a very low level, the pre-trigger system must be physically installed very close to the detector inside the L3 magnet [78].

To collect, digitize and pre-amplify the analogue signals from the V0 and T0 detector an interface to the pre-trigger system is needed: the so-called **Front End Boxes** (FEB). The 2×32 signals from the V0 photomultiplier tubes are processed by 2×4 FEBs, while there are two FEBs for the 2×12 T0 signals, making it a total of 44 channels/five FEBs per side of the collision point. The preamplifier of the FEBs receive the analogue signals from the detectors and convert them into three outputs: two output signals are used in the V0 and T0 FEE while the third is provided to the PT system. It is a differential signal with an amplification of 5 for each polarity. This differential signal is then discriminated into a digital signal and fed into the FEB FPGA. The converted digital signals are used as input to the first of three stages of **Look Up Tables** (LUT) which correspond to three decision levels and are implemented in the FPGAs of the FEBs. Each set of five FEBs sends its data to a **Control Box** (CB-A/C; depending on the side of the detector) where they are combined and processed by the second stage of LUTs [79], [80].

8 Read-Out Of The TRD Pre-Trigger System

Since the TOF detector provides the big amount of 576 digital bits per bunch crossing, processing like for T0 and V0 is not possible. Therefore, it has its own big single FPGA, capable of handling this high number of input channels². This so-called **TOF Logic Multiplicity Unit (TLMU)** calculates trigger decision base on the events seen by the TOF modules which are classified by multiplicity ranges and coincidence between the 18 supermodules (like back-to-back, back-to-back ± 1 (sector) or back-to-back ± 2 (sectors)). The result are 8-bit signals corresponding to eight different TOF trigger conditions. Together with the trigger signals from the CTP and the CB-A/C data transferred via optical fibers, the TOF data is arriving directly at the so-called **Control Box Bottom (CB-B)**. All the PT contributions (incl. the CB-B internal BC) can be used individually or combined in a third stage of LUTs to make a final trigger decision, generating a PT and providing the L0 contribution. The trigger output to the TRD supermodules and the CTP is generated by a finite state machine. It ensures that only a valid sequence of trigger pulses can be sent to the SMs. A diagram of the PT creation path can be found in 8.6 [81].

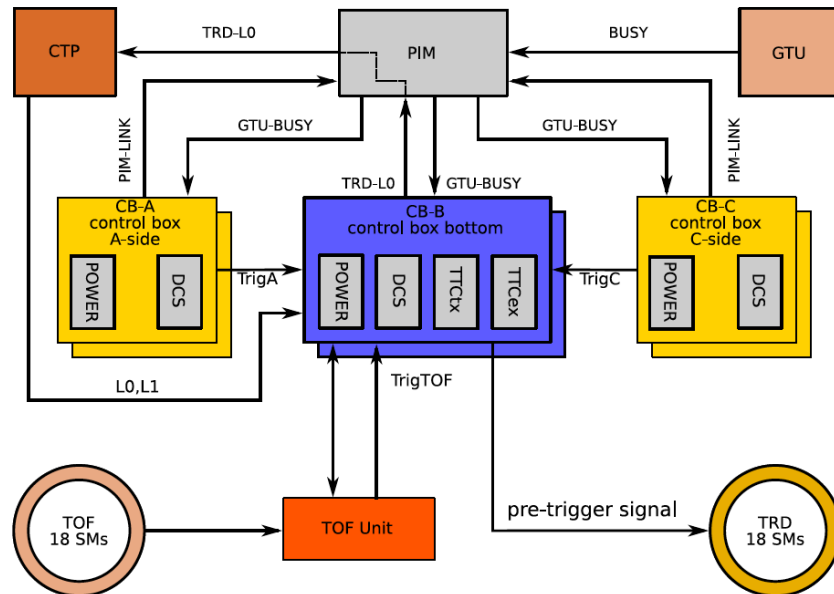


Figure 8.6: A diagram of the PT creation logic [80].

²Another motivation for the single FPGA is to have the possibility of deriving non-local trigger decisions, e.g. coincidences from opposing TOF sectors (for example for cosmic data taking)

As soon as the TRD FEE has been woken up by a PT, the MCMs start to read out, amplify, filter and temporarily save the charges created on the cathode pads. However, this process can be aborted by a missing L1 trigger. If this is not the case, fits are calculated and they start to reconstruct the tracklets - the track fragments of a passing particle within one of the layers of the TRD drift chambers. This tracklet information is shipped via the TRD module's **Optical read-out Interface board (ORI)** to the **Global Tracking Unit (GTU)** within $4 \mu\text{s}$ using a transfer rate of 2.5 GBs^{-1} . The GTU combines the tracklets to tracks to identify electrons with high transverse momentum, jets (number of tracks above a certain p_t threshold), single tracks etc. Based on these information it issues and sends a TRD L1 to the CTP within $< 6.1 \mu\text{s}$. Figure 8.7 gives the time line of a typical trigger sequence from PT to L1 showing the inputs from the pre-trigger system and CTP and the global outputs that are forwarded to the TRD supermodules.

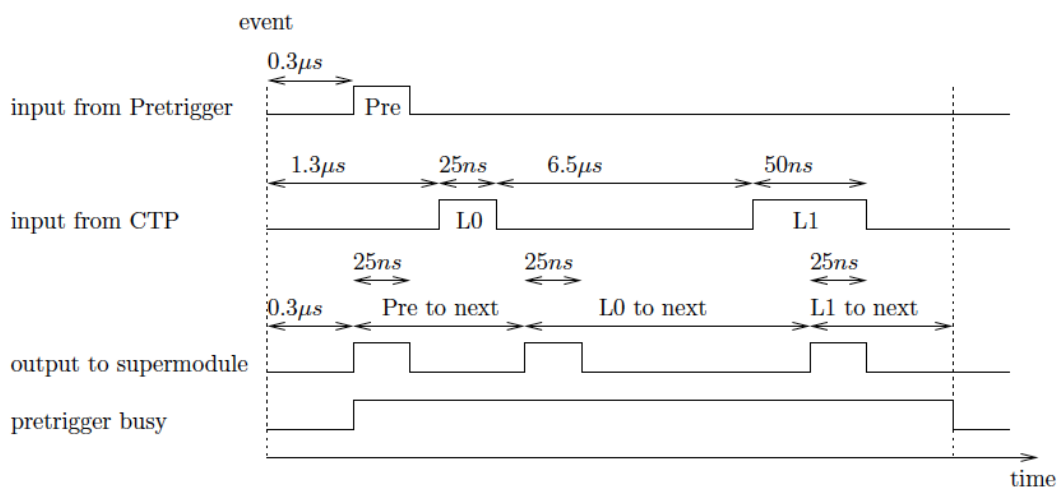


Figure 8.7: Timeline of a trigger sequence. The FEE on the TRD supermodules expect three trigger pulses each being 25 ns long: PT, L0a and L1a. (The 50 ns L1 pulse from the CTP is reduced to 25 by the pre-trigger processing logic.) All three triggers are identical and therefore have to arrive in the right chronological order to be identified correctly. The timing is uploaded to the FEE of the SM during the start-of-run configuration. [78].

If an L1a comes back from the CTP ($7.4 \mu\text{s}$ after the collision), the FEE sends the

8 Read-Out Of The TRD Pre-Trigger System

buffered raw data to the GTU and goes back to stand-by. The GTU temporarily stores the raw data within its event buffering units, until an L2-decision is made. An L2a will cause the data to be sent to the DAQ and HLT, an L2r will discard it. Due to the GTU multi event buffer, it is even possible that a new trigger sequence is started after the L1 (before the L2a) [76].

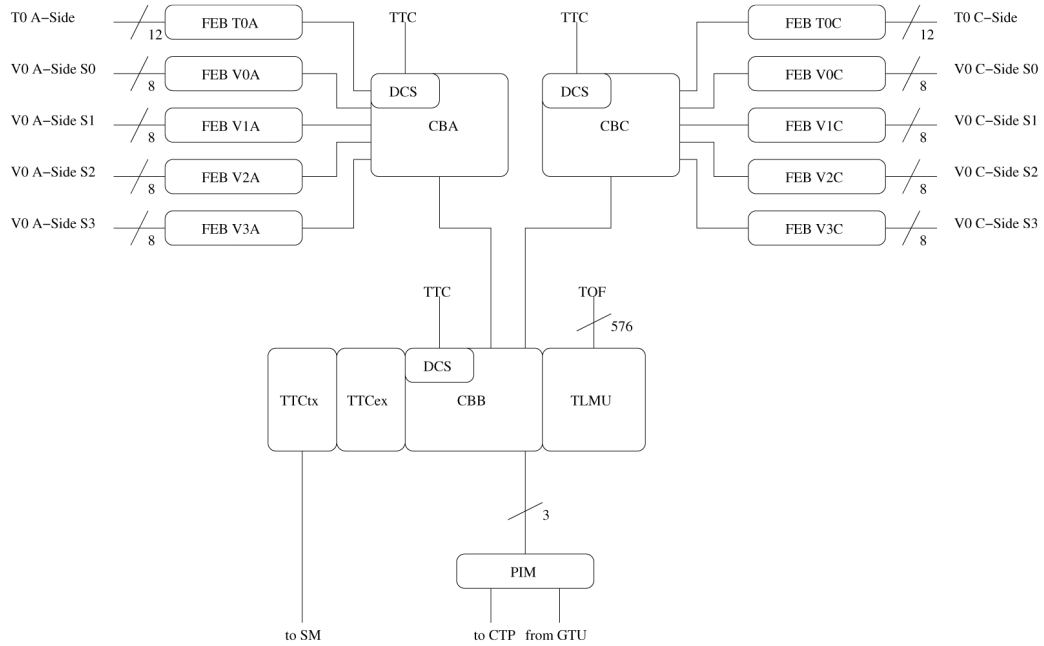


Figure 8.8: Schematic of the connections between the different hardware components of the pre-trigger system. The CB-B is the center of the system. It receives inputs from CTP (via TTC), GTU (via PIM), CB-A/C and the TLMU; its outputs go to the TRD and CTP. CB-A/C get their inputs from the five FEBs and have one output to the CB-B each [78].

Figure 8.8 gives an overview of the main pre-trigger hardware parts and their connections between each other. Since the control boxes use standard TRD DCS boards, they need an Ethernet infrastructure for communication purposes. The CTP interface is using LVDS whereas the pre-trigger uses optical connections only (except for the Ethernet), wherefore a custom module is implemented to interface between the two: the **Pre-trigger Interface Module** (PIM - details below). For additional debugging and trigger study, all CBs can send their trigger output to this PIM. Since the PT signal is essential for the smooth operation of the TRD all pre-trigger

system sub-components except for the TLMU and PIMFPGA exist twice. If the primary system fails, the backup system is powered up and takes over. PIM and TLMU can operate with both systems. Through their direct connection to the CB-B they get the information which system is to be used. From the three control boxes within the pre-trigger system, A and B have the same hardware and functionalities, while CB-B is slightly different. It consists of 2x4 modules for the primary and back-up systems, namely a **pre-trigger main-board**, a power module, a TTCex (encoder/transmitter) and a TTCtx (transmitter) module, whereas the CB-A/C do not have the TTC modules. Primary and back-up system in each box are separated and have their own power supply. The functions and features of the CBs are summarized in table 8.1 and a schematic view of the hardware of the control boxes can be found in figure 8.9 [82].

Function / Feature	CB-A and CB-C	CB-B
TTC receiving (TTCrx)	yes	yes
TTC forwarding (TTCex/TTCtx)	-	yes
FEB control and trigger accept	yes	-
TOF trigger accept and logic	-	yes
Sub pre-trigger logic	yes	yes
Main pre-trigger logic	-	yes
Interface to PIM	yes	yes
Ethernet	yes	yes
Backup system	yes	yes
Form factor	small VME 6U	full VME 6U

Table 8.1: Functions of the CBs in the pre-trigger system [82].

The pre-trigger main-board - of which each CB has two - is a composition of four individual PCBs. The **base board** supports all other components and provides services such as power and I/O devices. Namely it has several optical in- and outputs, three Lemo connectors to provide signals to the TTC and a RJ45 connector for the network connection. All connections are forwarded to a double-row of metal

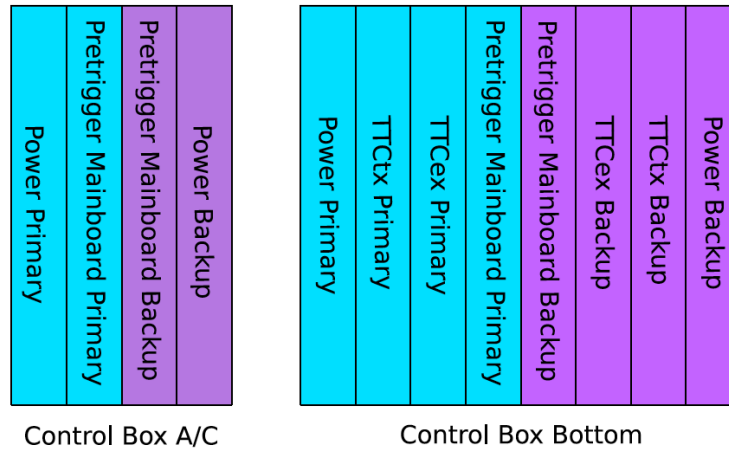


Figure 8.9: Hardware setup of the CB-A/C and CB-B [80].

pins, which are shared by the **DCS board** and the **FPGA sub-board**. The DCS board contains an FPGA with an embedded ARM processor running Linux which allows for easy access (ethernet) and control of all pre-trigger parts. It reads and writes the registers of the control box FPGA via SCSN. The FPGA designs for the pre-trigger main-board, the FEB and TLMU FPGAs can be uploaded via two JTAG lines. Furthermore, it receives the LHC clock signal and the CTP trigger signals through the optical receiver TTCrx, which decodes the incoming optical signal. An FPGA board with a Xilinx Spartan3 FPGA provides the full logic for the signal processing and trigger generation for the TRD FEEs. It receives the converted TTC signals from the DCS board. The last component of the pre-trigger board is an **adapter card** which is different for the CB-A/C and CB-B. In case of the CB-A/C it provides the connection to the FEBs through RJ45 (incl. the JTAG connection). In addition, there are five optical transmitters on the base board of which three are connected to the PIM, one transmits the trigger element to the CB-B and the last one is spare. The BUSY signal from the GTU is received through an optical receiver. To collect the trigger elements the CB-B adapter card has a multi-pin connector to the TLMU (instead of the RJ45s on the CB-A/C cards) and two optical inputs for the connection to the CB-A and C. These inputs are synchronized, aligned and sent to the top level LUT whose 4-bit output is then fed to the trigger logic, together with the ALICE trigger signals (L0 and L1) and the GTU BUSY signal. Through

three optical outputs this information is forwarded to the PIM from where it is sent to the CTP. Two Lemo connectors serve this purpose of sending the signals to the TTC modules, a third one is used for forwarding the CTP B-channel which transmits serial data commands [80]. Figure 8.10 shows the block diagram for the pre-trigger mainboard of the CB-B.

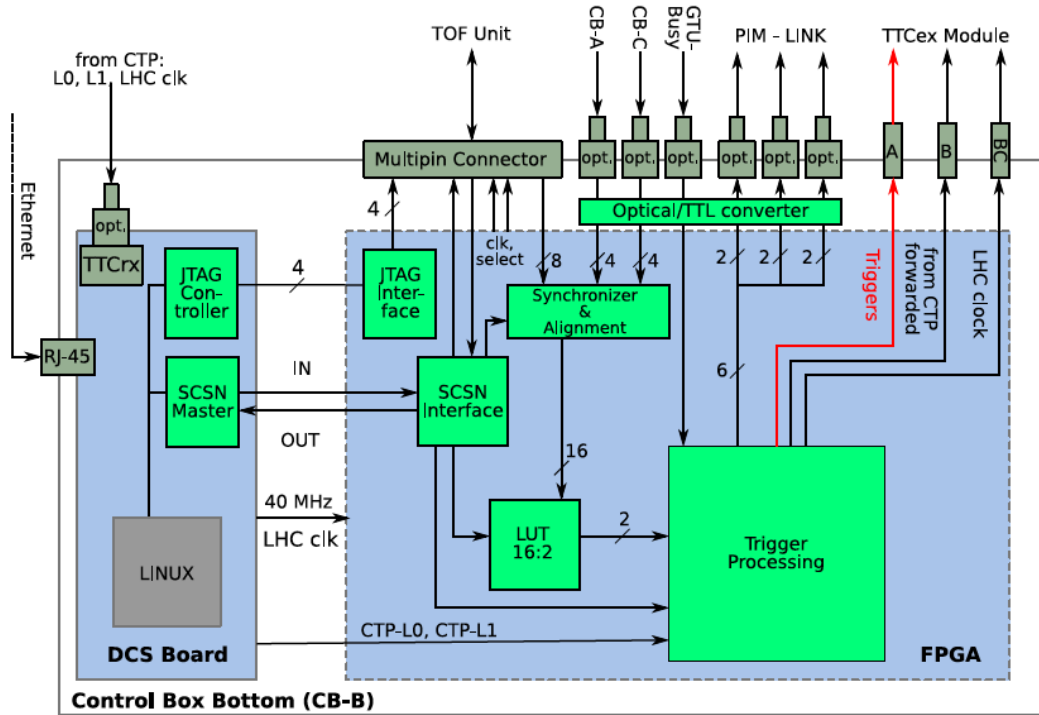


Figure 8.10: The pre-trigger main-board of the CB-B with its DCS and FPGA board, plus the interfaces to the TLMU, CB-A/C and TTC modules [80].

The afore mentioned PIM is responsible for forwarding the TRD L0 contribution to the CTP. It receives the data from the CB-B via optical fibers and converts them to LVDS signals, so they can be sent to the CTP. Equally, it converts LVDS signals to optical signals, e.g. the BUSY signal from the GTU to the pre-trigger system. It comprises two different types of VME modules:

The **PIMOPT** is the optical interface module which converts between optical and LVDS signals, sending information to and from the the control boxes. Each of the two pre-trigger main-boards of a CB connects with four optical fibers to either the primary or backup PIMOPT. Three of the fibers transmit the CLK and two trigger

bits to the PIM. The fourth fiber transmits the BUSY signal from the PIM to the CB. Therefore, PIMOPT has 3x3 optical receivers and three optical transmitters to interface with CB-A/B/C. Each data link coming from the three CBs is 160 Mbps incl. the LHC-CLK information and it can carry 4x3 bits per BC. In case of conflicts with the 160 Mbps it is possible to downgrade to 80 Mbps x 3 links which leads to 2x3 bits per BC. In one VME crate there are two PIMOPTs installed of which one is used to receive signals from the primary part of the CBs and the other for the back-up system.

The **PIMFPGA** is connected to the PIMOPT primary and back-up system via ribbon cables. It can send the two (primary/back-up) received BUSY signals from the GTU back to PIMOPT and transmit up to eight trigger contributions to the CTP. It uses the same FPGA as the FEBs that can automatically detect which of the PIMOPT systems is active and switch internally between the two. A JTAG-port is used to program the EPROM (Erasable Programmable Read Only Memory). For the interfacing with the CTP, there are eight LVDS drivers functioning with the CTP-standard chips. Four LVDS receivers get the BUSY signals from CTP and GTU [83].

Physically, the pre-trigger modules are located as follows: CB-A sits under the gangway of the ALICE mini-frame in front of the V0 detector, CB-C is on top of the muon absorber inside the L3 magnet. Equally inside the magnet are the CB-B and TLMU, located on the C side below sector 12 (compare figure 8.11). The PIM sits in a VME crate in the C-Side racks under the muon arm.

8.4 Studies On Realizing The Read-Out

- Idea and Motivation

Since the beginning of the pre-trigger operation only the final trigger decision and monitoring results were read-out, but it was decided to implement an upgrade to acquire all necessary data to predict, cross check, monitor and analyze the full pre-trigger functionality. In addition, this upgrade would bring improvement to the physics performance of the TRD. Electron PID in central

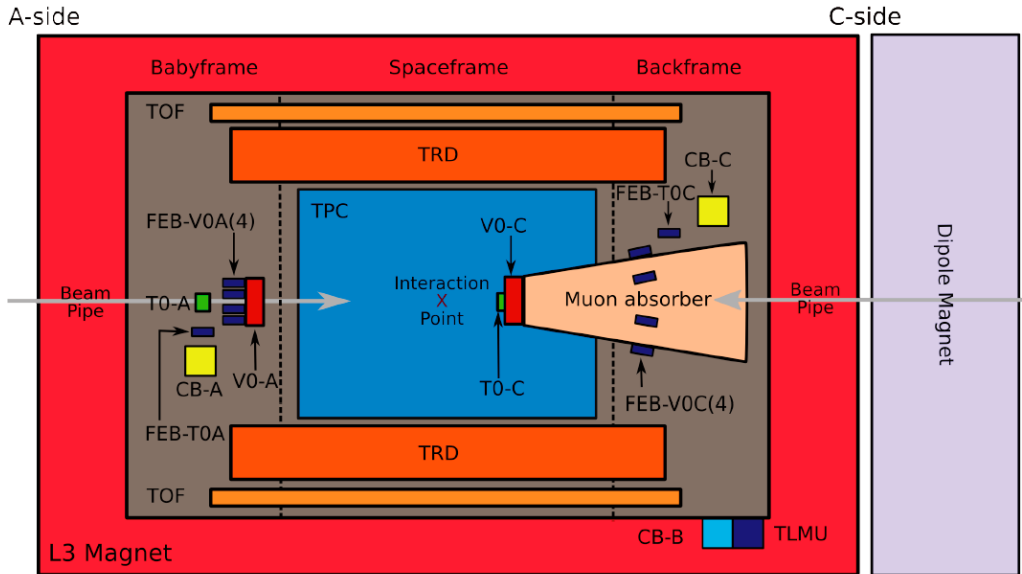


Figure 8.11: Physical locations of the pre-trigger subcomponents within the ALICE cavern (not shown: PIM) [80].

diffractive events would be more feasible when all TOF bits were to be found in the data, even though the TRD is not yet fully equipped. The masked out TOF bits (gaps of the missing SMs) and noisy bits could be corrected for more easily and precisely. With a read-out of all the pre-trigger input data - namely the discriminated V0/T0 signals and TOF bits - there would be more information for simulation of implemented and alternative pre-trigger algorithms to check the proper pre-trigger operation.

The data from all processing stages - the trigger inputs from V0/T0 and the LUT results, all 576 input bits and trigger conditions from the TLMU plus the CB-B trigger inputs (CB-A/C, TLMU) and decisions - would further improve the supervision of the pre-trigger operation concerning data processing, transmission errors etc. The main idea was to implement a “pipeline” for the complete pre-trigger data to enter the read-out in the FEBs, CB-A/B/C and TLMU. Furthermore, it was considered that a read-out trigger (PT or L0) would transfer data to a local event buffer, then forward all data from the CBs to a new interface module named **PIMDDL** (Pre-trigger Interface Module

8 Read-Out Of The TRD Pre-Trigger System

Detector Data Link) which would then send the data to DAQ on each L2a. The idea of the read-out scheme can be found in figure 8.12 [84].

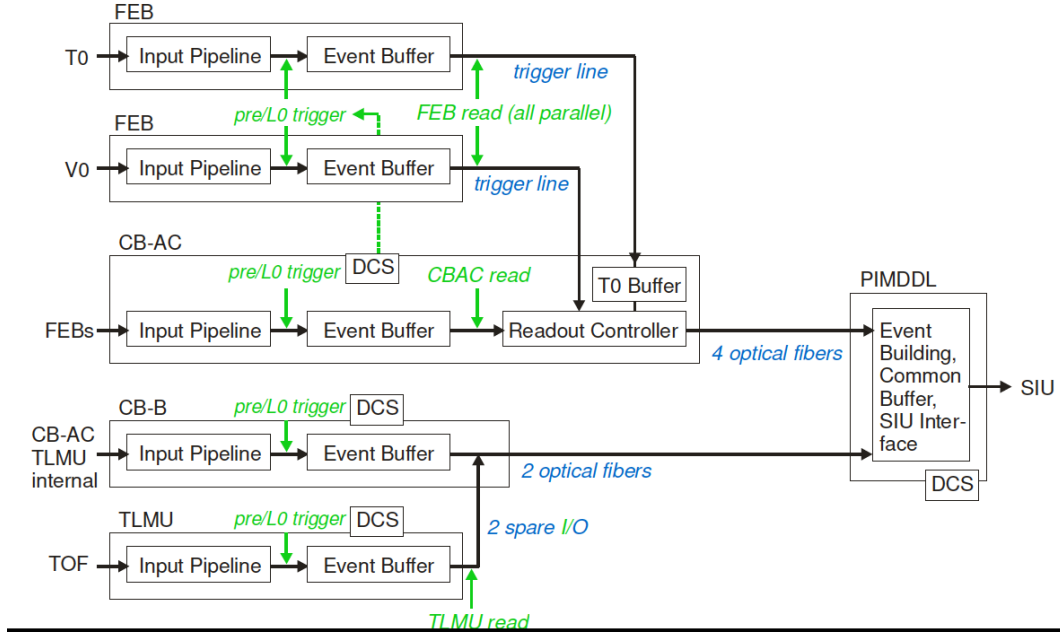


Figure 8.12: Readout concept [84].

All data should be read-out (i.e. on pre-/L0/L1/L2 triggered events) and marked with a timestamp, so that later the full pre-trigger timing is extractable (internal delays, external timings). In addition, multiple bunch counts (BC) around a PT with a configurable range and read-out trigger level should be stored [84].

- Realization

Firmware changes and upgrades such as additional functionality in all FPGA designs are necessary to realize the idea of a PIMDDL. In general, all FEBs, CB-A/B/C and TLMU need an additional read-out data pipeline, its depth depending on the read-out trigger and range, an event buffer whose depth depends on the read-out range of the respective FPGA and a read-out controller. Furthermore, the FEBs need additional logic for a multifunctional SCSN/trigger line and the CB-A/C an FEB read-out control plus an additional T0 data buffer. An overview of the rates of (desired) data to be processed can be found in table 8.2.

8.4 Studies On Realizing The Read-Out

Data & rates per BC		
Source	Rate [bit]	Details [bit]
V0 FEB (2x4)	10	V0: 8, LUT: 2
T0 FEB (2x1)	14	T0: 12, LUT: 2
CB-A	14	FEBs: 10 (4x2 + 2), LUT: 4
CB-C	14	FEBs: 10 (4x2 + 2), LUT: 4
TLMU	584	TOF: 576, TLMU result: 8
CB-B	24	TLMU: 8, CB-A: 4, CB-C: 4, LUT: 2, PT:1, CTP: 3, misc: 2
Data & rates per event		
Source	Rate [bit]	Read-out time [μs]
V0 FEB	210	5.25
T0 FEB	294	7.35
CB-A	294	1.9
CB-C	294	1.9
A side total	1428	9
C side total	1428	9
CB-B	504/12768 (with TOF)	6.3 (160 with TOF)
total (A + C + CB-B)	3360/15624 (with TOF)	

Table 8.2: Details of the data to be read-out by the PIMDDL. The data is listed for a single bunch crossing (BC) and for the range of 21 bunch crossings around a pre-trigger (e.g.: +15/-5) at the LHC CLK rate of 40MHz [84].

For the hardware the idea was to use the existing hardware and logic resources to the largest possible extend which would mean keeping the pre-trigger system as it is up to the PIMOPT from where the connection between the FEBs and TLMU to the CBs would be established through the trigger decision path, while the CBs and PIM could use existing, spare fibers. The LVDS connection from the PIMOPT was supposed to go directly to the new PIMDDL module. The requirements included that it should contain an FPGA for data buffering, interface control and event building, an SIU interface to the DDL, a DCS

8 Read-Out Of The TRD Pre-Trigger System

board for the trigger (TTC) interface and slow control plus an interface to the PIMFPGA for L0 forwarding to CTP. Several alternatives were considered as to which hardware to use [84].

One proposal was to do a new design based on the one of the TRD **Super-Module Unit** (SMU) since it already fulfills some of the pre-trigger read-out requirements. Originally it is responsible for controlling the operation of a GTU segment, according to the trigger information received by the CTP. It has the required 6U VME form factor, an interface to PIMOPT via a mezzanine board and an interface to power (VME to CompactPCI interface board) would be possible. It consists of a high-end FPGA which provides 94896 configurable logical blocks and 768 I/O pins plus additional specialized functional blocks, such as 20 Multi Gigabit Transceivers (MGT) that can be used for serial data processing with gigabit rates. Digital Clock Managers (DCM) allow the manipulation and derivation of clock signals with a constant phase relationship to the reference clock (LHC CLK). Furthermore, it is equipped with an SIU that establishes the optical link to the DAQ and a DCS board for the connection to the TRD. A design sketch of the SMU board can be found in figure 8.13.

The second idea was to re-use the design of the TPC Readout Control Unit (RCU) which was initially developed for controlling the read-out of the TPC, and initializing and monitoring its Front-End Cards (FEC) but is now also used for other detectors such as PHOS and FMD. It equally has the 6U VME form factor and provides the required interfaces to DCS, DAQ and TTC, plus the data paths and logic but would need a new interface to PIMOPT on the existing FEE bus connectors plus a separate power connector. Figure 8.14 shows the schematics of an RCU motherboard with its connections to the DAQ, trigger and detector control systems and to the front end electronics of the respective detector [85].

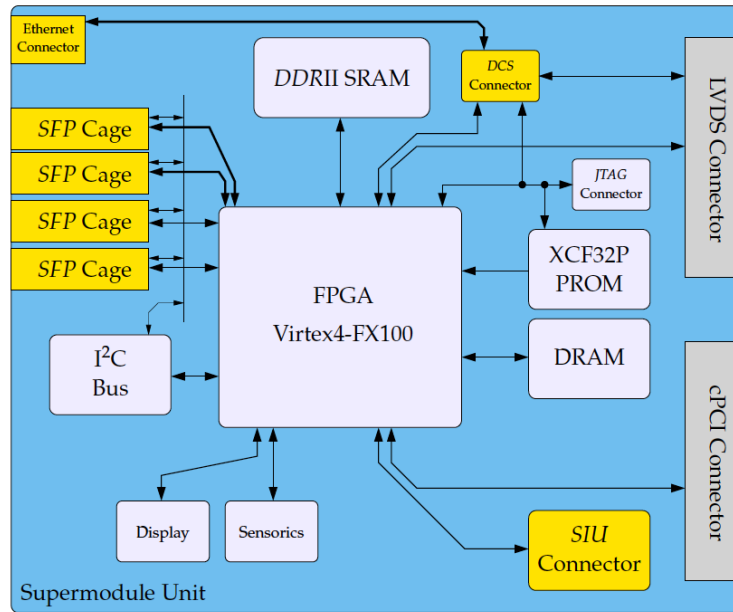


Figure 8.13: Schematic of an SMU board [76].

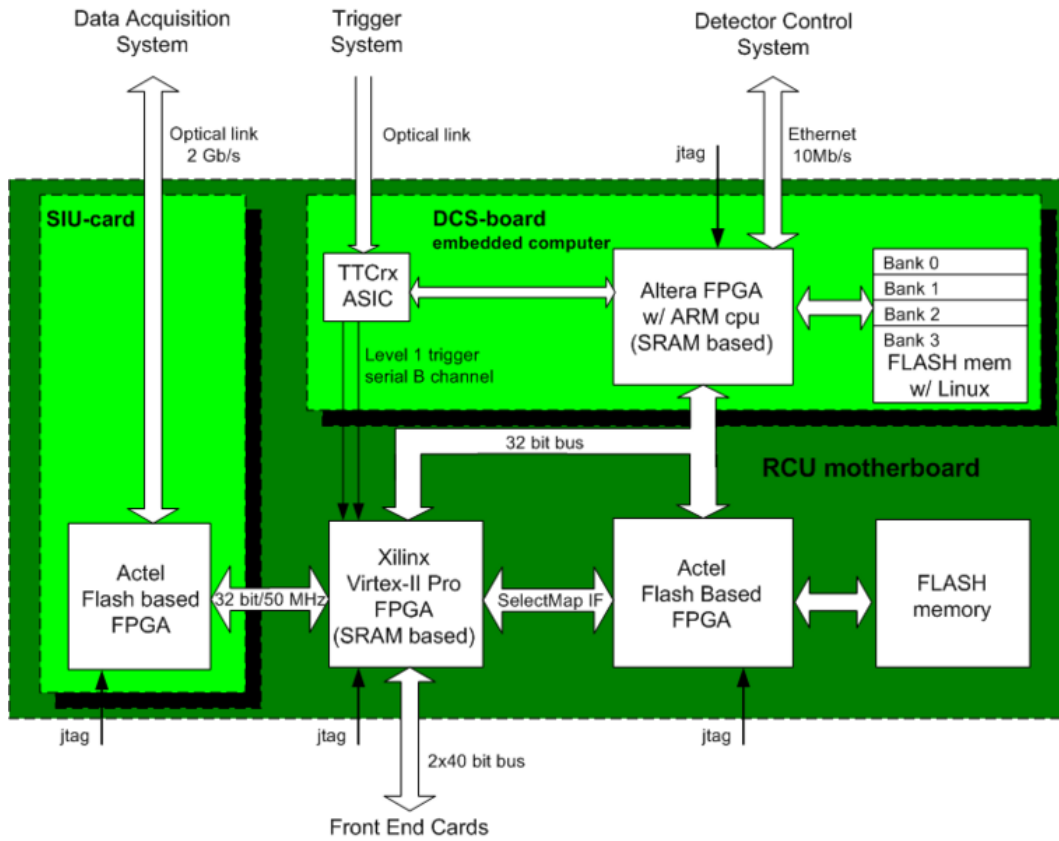


Figure 8.14: Schematic of an RCU mother board [85].

8 Read-Out Of The TRD Pre-Trigger System

After balancing the arguments it was yet decided to go for the third option which is to re-use and upgrade the existing CB-B pre-trigger main-board, adding an FPGA and optical links. The motherboard was not changed but kept as it is, except for some modifications on the connectors and adding a larger FPGA - the Actel FPGA ProAsic3+ with 75k Data Flip-Flops (DFF) and 500 kbits memory. A design sketch of the modified CB-B can be seen in 8.15 [86].

- Testing at CERN

After finalization of the concept, design and layout [86], two PIMDDL boards were assembled and successfully tested for their basic functionalities at the University of Heidelberg before one of the modules was shipped to CERN and included into the surface setup for further testing. Since the PIMDDL combines the CB-B and the data read-out functionalities in one board, it had to be tested with respect to both. As afore described, the trigger information from CB-A/C and the TLMU are collected at the CB-B where the pre-trigger signal is derived and then transmitted to the TRD. In addition, this signal is sent to the CTP as the L0 contribution from the TRD. The GTU is connected to the CB-B to send a BUSY signal in case the TRD is not ready for receiving triggers, thus preventing the generation of further pre-trigger signals. The PIM part of the pre-trigger, now implemented in the PIMDDL, is used to translate between the CB-B (or more globally spoken: the pre-trigger system) and the GTU/CTP. In order to test all interconnections the PIMDDL was connected to an LTU, CTP simulator for receiving the LHC CLK and triggers and a CB-A/C main board connected to two FEB boards and equally the CTP simulator. To distribute its trigger decision, the subsequent ALICE triggers and the LHC CLK to a setup of several DCS boards - since no TRD supermodule was present at this time - it was additionally connected to the respective TTC modules (TTCex and TTCtx) with which it was possible to transmit the three signals (A channel for the trigger signals, B channel and BC channel for the LHC CLK). All CB-B functionalities were found to be present and operating properly. Furthermore, it is possible to send, receive and readout data. How-

8.4 Studies On Realizing The Read-Out

ever, the FPGA software is not yet fully developed, wherefore only “dummy data” was used for testing the general functioning.

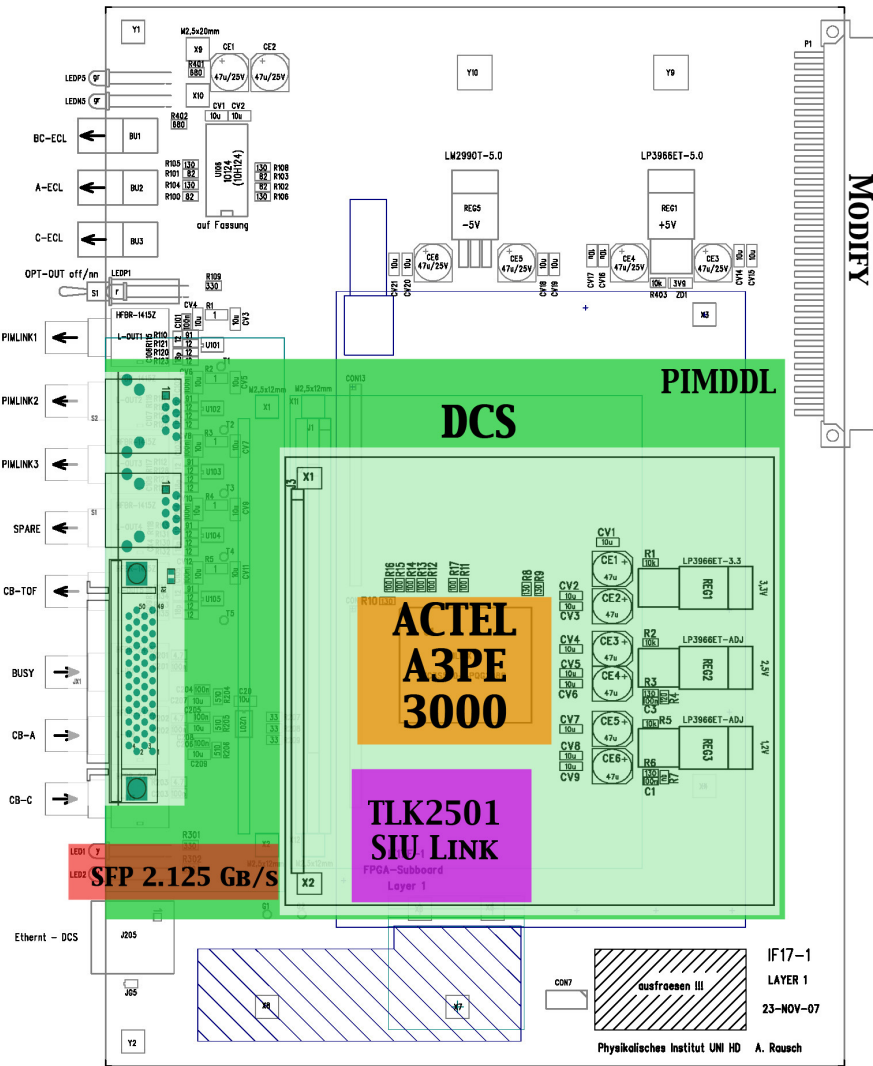


Figure 8.15: The "new" CB-B with the modifications for the PIMDDL functionality.

8 *Read-Out Of The TRD Pre-Trigger System*

Summary and Outlook

This chapter gives a summary of the work covered by this thesis. It was dedicated to the development, commissioning, testing, maintenance and upgrading of parts of the ALICE Transition Radiation Detector. The main focus of this work laid on the gas and gas monitoring system of the detector, its control software and a new pre-trigger hardware module for data read-out.

- The TRD gas system was surveyed, controlled, maintained, operated, improved and further developed to meet the high demands of the TRD. The quality of the operational gas has to be as high as possible to ensure the continuous excellent performance of the TRD. Therefore, especially the contamination of the Xe-CO₂ mixture with other gas components from, e.g. air diffusion, need to be kept on the lowest level. Since SF₆ has a very crucial effect on the detector efficiency each Xe supply was tested for an eventual contamination with this gas. All supplies were found to have a sufficiently high purity with SF₆ present only in marginal traces under 25 ppb. A stable gas composition is mandatory for a uniform drift velocity within the TRD. Thus, the procedure of cleaning the operational gas mixture with the purifier module was successfully modified to avoid the formerly present exhaustion of CO₂. The membranes used for CO₂ separation were commissioned, tested for satisfactory functionality and found to have an efficiency better than 2.5% of Xe loss. The removal of excess CO₂ after the insertion of new supermodules necessitated their operation as well as separating CO₂ from the gas mixture to be able to clean the Xe from Ar and N₂ afterwards with the help of a recovery plant. This plant, making use of the principle of cryogenic distillation, was equally tested, commissioned and operated. Its Ar and N₂ removal efficiencies

Summary and Outlook

were both found to be better than 99% - less than 0.7% of N₂ and 0.1% of Ar left in the gas - with no Xe lost. Since the amount of N₂ in the operational gas mixture of the TRD determines the frequency of operation of the recovery plan, the accumulated data from April to December 2011 was extrapolated to estimate when the contamination would be so high as to have a negative effect on the detector performance. For the end of 2012 this value was found to still be under 5%, thus making a cryogenic distillation only necessary in the LHC winter shutdown. Several improvements for a user friendly and more efficient operation of the recovery plant have been developed and proposed to the CERN detector development gas section to be implemented as soon as possible.

Another large part of this work was dedicated to gas leak hunting, detecting and fixing using different devices and techniques to this end. Minimizing the leaks to the maximum possible extend has let to an improvement of the gas loss of under 0.3 l/h (while 0.5 l/h are still with in the estimations/agreement of the TRD collaboration). Furthermore, each new supermodule assembled at the University of Münster and shipped to the ALICE experimental site was tested for integration readiness on the surface before being added to the already installed supermodules in the TRD setup within ALICE. Thus, each supermodule has undergone specific gas tightness tests, and malfunctions (leaks) were fixed before the installation. To facilitate these tests, a pressure sensor read-out software has additionally been successfully developed as part of this work. For the purpose of surface storage of tested supermodules that can not yet be implemented into the TRD, a gas supply setup has been designed and built to which up to three supermodules can be connected at the same time.

- The drift velocity and gas surveillance monitors “GOOFIE” of the TRD and TPC had to be modified for the specific needs of the detectors - both on the hardware and the software side. At present both monitors are installed within the respective gas systems, and are fully functional and operating.

Since the TRD GOOFIE was initially built for the FTPC of the STAR experiment it was adapted to run with a Xe-CO₂ gas mixture and a drift field

of 700 V/cm. For this purpose, several modifications and improvements on its setup were implemented before and during the commissioning phase. The high voltage cable was replaced and equipped with new connectors since the original equipment had become faulty and unreliable. The same was necessary for the resistor box of the pressure sensor, because this device was broken and caused noise on the read-out of the ambient measurement. Furthermore, the RC filter box between the power supply and the GOOFIE was modified from $R = 1.1 \text{ M}\Omega$, $C = 1 \text{ nF}$ to $R = 10 \text{ M}\Omega$, $C = 2.5 \text{ nF}$ to further decrease the noise level caused by the AC component of the power supply. Additionally, several modifications on the interior of the GOOFIE were undertaken with the result of clean signals and reliable measurements of the drift velocity.

The existing software was equally modified and upgraded to improve the quality of the signals provided by the GOOFIE. With these better results the removal of outliers in the read-out data and satisfying calculations of the gain and drift velocity are obtained. The drift velocity measurements of the TRD GOOFIE can now be used for comparison in order to be able to adjust the HV of the TRD accordingly and more precisely. In addition, the remote control of the online application as well as the power supplies were successfully developed and implemented together with a suitable (graphical) user interface. All these software upgrades were carried out and implemented on the TRD and TPC systems.

The online calculation of the TRD gas composition with respect to CO_2 and N_2 has also been implemented. However, the data retrieved from the TRD GOOFIE is not yet reliable and further adjustments remain an open task.

- For the monitoring, control, operation and data collection of the ALICE experiment a process control and visualization software called PVSS is used. In general, PVSS creates a connection between the detector hardware components and the Detector Control System (DCS). Another project presented in this document was the renovation and further development of the user interface of the TRD DCS with the aim of improving its usability and therefore the operation of the detector. A common upgrade to all panels as well as

Summary and Outlook

modifications specific to the individual TRD sub-systems were performed and completed successfully.

- The large quantity of TRD electronics is mostly kept in a stand-by mode in order to save energy and minimize the amount of heat created. For efficient data taking it is therefore necessary to have an early wake-up signal which is generated by the TRD pre-trigger system. As part of this work, the conceptional idea for the read-out of the complete pre-trigger data to study the efficiency and functionality of the pre-trigger system was further investigated, developed and finalized. After the production and first functionality tests of the hardware for this module called PIMDDL at the University of Heidelberg (Institute of Physics) it was successfully tested in the TRD test setup at CERN/point 2. The next stage in continuing this project will be the development and implementation of a fully functional read-out software and the insertion of this module into the pre-trigger system in the ALICE cavern, which is scheduled for the shutdown period starting at the end of 2012.

List of Figures

1.1	The model to describe the particles and forces that comprise all that surrounds us is called the Standard Model - it has been widely successful in explaining observed phenomena and correctly predicting new measurements. The above picture shows the elementary particles and gauge bosons (i.e. the force “carriers”) [4].	3
1.2	Measurements of the strong coupling constant α_S as a function of the respective energy scale Q [5].	5
1.3	The QCD phase diagram: One of the primary goals of the experimental programs at BNL (RHIC) and CERN (LHC) is to produce and study the quark-gluon plasma. The line shows the phase boundaries for the indicated phases. The blue circle depicts the critical point. Temperatures reachable with the two accelerator facilities are indicated [7].	7
2.1	The actual (2011) CERN accelerator complex including the four big LHC experiments (ATLAS, CMS, ALICE, LHCb) as well as the Antiproton Decelerator (AD), the ISOLDE (Isotope Separator On-Line) facility, the CNGS (CERN Neutrinos to Gran Sasso) project and the CLIC (Compact Linear Collider Study) test area. [7].	15
2.2	Summary of the planned LHC upgrade [25].	17

LIST OF FIGURES

3.1 The ALICE detector with its main sub-detectors in the CERN/point 2 cavern. Located inside the red L3 magnet - from the inside out: the Inner Tracking System (ITS; see close-up for details) consisting of two layers of high-resolution silicon pixel (SPD), drift (SDD), and strip (SSD) detectors, having the Forward Multiplicity Detector (FMD), V0 and T0 on its outsides, the Photon Multiplicity Detector (PMD), the cylindrical Time Projection Chamber (TPC), three particle identification arrays of Time Of Flight (TOF), Ring Imaging Cherenkov (HMPID) and Transition Radiation (TRD) detectors, and two electromagnetic calorimeters (PHOS and EMCal). The adjacent forward muon arm consists of absorbers, tracking and triggering chambers and a dipole magnet. An array of scintillators (ACORDE) can be found on top of the L3 [27]. 20

3.2 The basic principle of the forward muon spectrometer is shown: an absorber to filter everything but the muons, a set of tracking chambers before, inside and after the magnet and a set of trigger chambers [27]. 26

4.1 Illustration of the mirror charge model for the creation of **transition radiation**. A charged particle produces a mirror charge when passing the boundary between two media of different dielectric constants ϵ_1 and ϵ_2 . These two opposing charges build an oscillating dipole which radiates a photon γ and the [32]. 30

4.2 Spectrum of TR photons absorbed by a Si detector from electrons with $p = 30 \text{ GeV}/c$ and an emission angle of $\Theta = 90^\circ$. The mean detected TR photon energy is $E_\gamma \approx 10 \text{ keV}$ [35]. 31

4.3 Design of the TRD radiator [38]. It consists of a 32 mm stack of polypropylene fibre mats enclosed by two 8 mm Rohacell[®] foam sheets surrounded by a lamination of 0.1 mm carbon fibre sheets. . . 32

4.4 Pad geometry of an MWPC [37]. The cathode plane is divided into cathode pads, orientated orthogonal to the anode wires. 35

LIST OF FIGURES

4.5	Schematic of a TRD read-out chamber [39]	35
4.6	Modular design of the TRD. When fully assembled it will consist of 18 supermodules with five (SM 13, 14, 15 only four) stacks of six chambers each. This makes a total of 522 chambers for the entire TRD. Each chamber consists of 12 - 16 rows of pads each with 8 multi-chip modules (MCMs). Each MCM has 18 read-out channels making it a total of 1.16×10^6	36
4.7	Spectrum of the average pulse height vs. drift time for pions (blue triangles), electrons (green squares) and electrons+TR photons (red circles) - test beam data. At later drift times there is a significant increase in the average pulse height for electrons, due to the preferential absorption of the TR near the entrance of the drift chamber [27].	37
5.1	Schematic of the TRD gas system. From the mixer unit on the surface the Xe-CO ₂ mixture is sent to the plug just above the ALICE cavern to be distributed into the 18 TRD supermodules. With the help of the pump module (equally in the plug) the return gas from the detector is compressed and pumped back to the surface gas building where it is recycled with the help of the purifiers. The loop pressure regulation is performed by acting on the suction speed of the compressor; this reaction mechanism is driven by the pressure sensor located at the detector [37].	40
5.2	Pressure regulation segmented into 14 individually controllable sections [37]. Sectors 03, 04, 05 as well as 12, 13, 14 are grouped as one section each, since they basically lie on the same height level.	42
5.3	A TRD manifold (middle) with bubbler (right) and pressure sensor unit (left).	44

LIST OF FIGURES

5.4 Schematic of the mixer module in the TRD gas system. The amount of the two primary gases (Xe-CO₂) is regulated through Mass Flow Controllers (MFC). Each gas type has two MFCs: one for the purge/fill/direct and one for the run mode. 46

5.5 Principle of a pressure control valve [36] similar to the ones used in the TRD gas system. The spring keeps the valve open until the outlet pressure overcomes its setting which is when the valve begins to close to keep the output pressure constant. 47

5.6 Pulse height spectrum for a drift field of 770 V/cm for different amounts of O₂ in the TRD operating gas [44]. 50

5.7 Pulse height spectrum for different drift voltages in the TRD operating gas with an SF₆ contamination of 0.94 ppm [44]. 50

5.8 Simulated impacts of N₂ on the operation of the TRD regarding the drift velocity and gain. The results show that a few percent of N₂ in the mixture can be tolerated [46]. 52

5.9 Absorption length as a function of the photon energy for argon, krypton and xenon [47]. 53

5.10 A galvanic fuel cell. The flow of electrons from anode to cathode via the external circuit results in a measurable current proportional to the partial pressure of oxygen [48]. 54

5.11 Principle of an aluminum oxide sensor with a gold layer and aluminum probe forming the anode and cathode [49] 55

5.12 Twin column purifier module with inline regeneration [42]. 58

5.13 Schematic setup and principle of operation of membranes consisting of capillary tubes of polyamide. 59

5.14 Schematic of the 2-stage membrane module used for CO₂ removal in the TRD [42]. 60

LIST OF FIGURES

5.15 The recovery plant as designed for the ALEPH experiment. It consists of a 100 l distillation column divided into three compartments (E01, E02, C01), a sample volume R01, a LN₂ cooling circuit with temperature regulation, provisions for heating up the bottom of the column, and several pneumatic and manual valves for the operation of the plant [45]. 62

5.16 The PVSS-based UI as it is integrated into the TRDs main DCS. Here, the data can only be displayed, but not controlled. Nonetheless it is possible to get informed about alarms, follow the trends of the different data points provided by the GCS and also to archive this information. 64

5.17 GCS-provided UI of the mixer module of the TRD gas system. . . . 64

5.18 Chromatograms of an SF₆-contaminated Xe supply 65

5.19 Erratic decrease of the CO₂ content due to the swapping of the purifier cartridges. (Swaps indicated with red lines.) 67

5.20 Increase of nitrogen in the TRD gas mixture over a period of eight month (April - December 2011). 69

5.21 Increase of argon as a function of time caused by a faulty pressure regulator. Data taken from analysis with the gas chromatograph. . . 70

5.22 Simulation of the impact of the N₂ and Ar contamination in the TRD gas on its pion rejection (per supermodule layer) [51]. 72

5.23 A schematic of the recovery plant as it is presently installed in the TRD gas circuit. 74

5.24 Schematic of the clean room test stand with a SM (upper left) and the gas supply (upper right). It is equipped with an oxygen analyzer ("ppm"), three mass flow controllers, a safety bubbler, a compressor ("pump") and a fan (triangle). 76

LIST OF FIGURES

5.25 Data taken from an Orbisphere measurement. The O₂ contamination [ppm] as well as the temperature [°C] are plotted over time. 77

5.26 A block diagram of the logic for operating the LogicBox as realized with LabView: Step 1 - opening of the port, Step 2 - connecting and initializing, Step 3 - sequence control (parameter setting, data read-out and displaying), Step 4 - closing of the port [52]. 79

5.27 Block diagram of the specific logic developed for the read-out of the pressure sensors in the gas testing surface setup at CERN. 79

5.28 Pressure read-out display of one of the pressure sensors connected to a supermodule. The graphic shows the differential pressure [mbar] over time [sec]. 80

6.1 Schematic of the TRD GOOFIE [60]. A stainless steel vessel houses a field cage together with two α -sources for gas ionization, two trigger counters, a pick-up detector and two PT-100 sensors for the temperature measurement (T_1, T_2). 84

6.2 Schematic of a trigger counter in the GOOFIE field cage [56] 87

6.3 Schematic of a pick-up counter in the GOOFIE [56] 88

6.4 The data acquisition setup. The information from the near, far and pickup counters is processed by the GOOFIE board and sent to a “Linux PC”. The ambient measurements such as near/far temperature (T_n, T_f), pressure and field cage voltage (V_{FC}) are retrieved by a PCI DAQ board. 90

6.5 Plots of a single near (top) and far (middle) event and the sum over 2500 events from both (bottom) [62]. 92

6.6 Drift velocity in Xe-CO₂ plotted against the normalized gas density and drift cage voltage $\rho_{Gas}/U_{drift} \approx \frac{p_n}{T_n \cdot U_n}$ [56]. 93

6.7 Resistor box connected to the pressure sensor. 95

LIST OF FIGURES

6.8	Location of the last resistor inside the GOOFIE	96
6.9	Spectra showing the near and far signal before (top) and after (bottom) installing the mylar foil [62].	98
6.10	Drift velocity spectrum before (top) and after (bottom) applying the software improvements [62].	100
6.11	Simulated 3D spectrum of the gain vs. N ₂ (y) and CO ₂ (x) content.	101
6.12	Serial-to-ethernet device PortServer®TS from Digi [65] interfacing between a Heinzinger (left) and an Iseg (right) power supply and a PC server.	103
6.13	PVSS-based UI for the GOOFIE on the operator node of the TRD DCS. Highlighted are the control panels for the pick-up (“PU”) and field cage (“FC”) HV. It is possible to switch the devices on and off, set the desired voltage, ramping speed and maximal, abandon a ramping process or even recover in case a hard-/software problem has occurred.	104
7.1	Overview of the ALICE DCS structure which is divided into three layers - both physically and logically [26].	107
7.2	The datapoint (DP) concept. “trd_goofie” (1) is a DPT with “TRD-Goofie” (2) as a DP. “Actual” and “FSM” (3) are DPE defined as BLOB with “sub-DPEs” (e.g. “Action” and “State” for “FSM”). “T1_over_p” (4) is a DPE defined as a float with several “configs” such as “_dp_fct” (5).	109
7.3	TRD FSM state diagram [72].	111
7.4	Overview of the TRD DCS structure and its connection to the central (ALICE) detector and experiment control systems [73].	112
7.5	GUI for displaying and controlling the TRD front-end detectors (FED). Marked in the red box on the left is the tree-like FSM browser.	114

LIST OF FIGURES

7.6 Comparison of the former and recent DCS top node. 118

7.7 Monitoring and control panels of the gas and cooling systems. 119

7.8 GUI for monitoring and operation of the GOOFIE. 120

7.9 FED overview panel. 120

7.10 Monitoring and control panel of the HV of an individual SM. 121

7.11 LV and PCU. 122

8.1 The context diagram of the ALICE CTP [75]. 127

8.2 The CTP boards in a VME crate. 1 - 4: trigger inputs, 5 - 10 trigger outputs transmitted to the sub-detectors via the LTU, 11 interface to DAQ (via DDL) and RoIP [75]. 128

8.3 A block diagram of the ALICE trigger system [76]. 130

8.4 Layout of the ALICE trigger system. Its location in the ALICE cavern being underneath the muon spectrometer [27]. 130

8.5 The architecture of the ALICE DAQ; The CTP selects the events, initiates the detectors' read-out via their LTUs and the TTC, and synchronizes the experiment with the LHC clock. The DAQ takes care of the data flow from the detector FEEs to the permanent storage, and of the control of this data flow using more than 500 DDLs. The HLT filters the information by quality to keep the amount of data on a reasonable level [77]. 132

8.6 A diagram of the PT creation logic [80]. 134

LIST OF FIGURES

8.7 Timeline of a trigger sequence. The FEE on the TRD supermodules expect three trigger pulses each being 25 ns long: PT, L0a and L1a. (The 50 ns L1 pulse from the CTP is reduced to 25 by the pre-trigger processing logic.) All three triggers are identical and therefore have to arrive in the right chronological order to be identified correctly. The timing is uploaded to the FEE of the SM during the start-of-run configuration. [78]. 135

8.8 Schematic of the connections between the different hardware components of the pre-trigger system. The CB-B is the center of the system. It receives inputs from CTP (via TTC), GTU (via PIM), CB-A/C and the TLMU; its outputs go to the TRD and CTP. CB-A/C get their inputs from the five FEBs and have one output to the CB-B each [78]. 136

8.9 Hardware setup of the CB-A/C and CB-B [80]. 138

8.10 The pre-trigger main-board of the CB-B with its DCS and FPGA board, plus the interfaces to the TLMU, CB-A/C and TTC modules [80]. 139

8.11 Physical locations of the pre-trigger subcomponents within the ALICE cavern (not shown: PIM) [80]. 141

8.12 Readout concept [84]. 142

8.13 Schematic of an SMU board [76]. 145

8.14 Schematic of an RCU mother board [85]. 145

8.15 The "new" CB-B with the modifications for the PIMDDL functionality. 147

List of Tables

1.1	Fundamental interactions and their characteristics [1].	1
5.1	Freezing and boiling points of the components contained in the TRD gas mixture.	61
5.2	Gas chromatography results of the operation of the TRD membrane module.	67
5.3	Gas chromatography of the recuperated gas after a full distillation process.	70
7.1	The TRD sub-systems and their dedicated worker nodes.	110
8.1	Functions of the CBs in the pre-trigger system [82].	137
8.2	Details of the data to be read-out by the PIMDDL. The data is listed for a single bunch crossing (BC) and for the range of 21 bunch crossings around a pre-trigger (e.g.: +15/-5) at the LHC CLK rate of 40MHz [84].	143

References

- [1] B. Povh, *Particles and Nuclei*. Springer, 6 ed., February 2008.
- [2] W. Siegel, “Fields,” *hep-th*, December 1999, arXiv:hep-th/9912205v3.
- [3] R. K. Ellis, W. J. Stirling, and B. R. Webber, *QCD and collider physics*. Cambridge: Cambridge University Press, 2003.
- [4] Fermilab, “Search for W’ boson production in the top quark decay channel.” www-d0.fnal.gov/Run2Physics/WWW/results/final/TOP/T06C/T06C.html, 2006.
- [5] S. Bethke, “The 2009 World Average of α_S ,” *hep-ph*, August 2009, hep-ph/0908.1135v2.
- [6] D. Griffith, *Einführung in die Elementarteilchenphysik*. Wiley-VCH, July 1995.
- [7] Interactions.org, “Quantum Diaries - Thoughts on work and life from particle physicists from around the world.” <http://www.quantumdiaries.org/>, 2011.
- [8] B. Müller, J. Schukraft, and B. Wyslouch, “First Results from Pb+Pb collisions at the LHC,” *hep-ex*, February 2012, arXiv:1202.3233v1.
- [9] A. Grelli, “Heavy Flavour Physics with the ALICE detector at the CERN-LHC,” *Journal of Physics: Conference Series*, vol. 316, no. 1, 2011.
- [10] A. Dainese, “Heavy-flavour production in Pb-Pb collisions at the LHC, measured with the ALICE detector,” *nucl-ex*, July 2011, arXiv:1106.4042v2.
- [11] T. Matsui and H. Satz, “J/ Ψ suppression by quark gluon plasma formation,” *Physics Letters B*, July 1986.

REFERENCES

- [12] D. Jouan, “NA50 results on Pb-Pb interactions at 158 GeV per nucleon.” CERN paper, January 2001.
- [13] A. Andronic, P. Braun-Munzinger, K. Redlich, and J. Stachel, “Evidence for charmonium generation at the phase boundary in ultra-relativistic nuclear collisions,” *nucl-th*, July 2007, arXiv:nucl-th/0701079v2.
- [14] Y. Pachmayer, “Physics with the ALICE Transition Radiation Detector,” *nucl-ex*, December 2011, arXiv:1112.2098v1.
- [15] S. Bass, M. Gyulassy, H. Stoecker, and W. Greiner, “Signatures of Quark-Gluon-Plasma formation in high energy heavy-ion collisions: A critical review,” *hep-ph*, p. 70, December 1998, arXiv:hep-ph/9810281v2.
- [16] G. A. et al., “Observation of a Centrality-Dependent Dijet Asymmetry in Lead-Lead Collisions at $E = 2.76$ TeV with the ATLAS Detector at the LHC,” *Phys. Rev. Lett.*, December 2010.
- [17] L. Gerward and C. Cousins, “The discovery of the electron: a centenary ,” *Physics Education*, vol. 32, no. 4, 1997.
- [18] CERN Press Office, “LHC proton run for 2011 reaches successful conclusion.” <http://press.web.cern.ch/press/pressreleases/releases2011/pr22.11e.html>, October 2011.
- [19] O. Bruning, P. Collier, P. Lebrun, S. Myers, R. Ostojic, J. Poole, and P. Proudlock, “LHC Design Report Volume I: The LHC Main Ring,” tech. rep., CERN, 2004.
- [20] Fermilab, “Accelerator - Fermilab’s Tevatron.” <http://www.fnal.gov/pub/science/accelerator/>, August 2011.
- [21] CERN, “The “Super” LHC.” <http://slhcpp.web.cern.ch/slhcpp/>, April 2012.
- [22] J. Wenninger, “The LHC Accelerator Complex.” Hadron Collider Summer School, June 2007.

REFERENCES

- [23] X. C. Vidal and R. C. Manzano, “Taking a closer look at LHC.” <http://www.lhc-closer.es>, 2011.
- [24] E. Tsismelis, “SLHC - THE LHC UPGRADE.” Corfu Summer Institute, September 2009.
- [25] L. Evans, “SLHC Accelerator and Injector Upgrades.” SLHC-PP kick-off meeting, April 2008.
- [26] ALICE collaboration, “The ALICE experiment at the CERN LHC,” *JINST*, vol. 3, August 2008.
- [27] ALICE collaboration, “A Large Ion Collider Experiment.” <http://aliceinfo.cern.ch/>, 2011.
- [28] R. Grosso, “The ALICE Inner Tracking System.” <http://w3.ts.infn.it/experiments/alice/alice-its/welcome.html>, May 2003.
- [29] P. G. et al., “The ALICE TPC, a large 3-dimensional tracking device with fast readout for ultra-high multiplicity events,” *physics.ins-det*, January 2011, arXiv:1001.1950v1.
- [30] J. Schukraft, “Heavy-ion physics with the ALICE experiment at the CERN Large Hadron Collider,” *Phil. Trans. R. Soc.*, 2012.
- [31] A. D. Mauro, “The High Momentum Particle IDentification detector.” <http://alice-hmpid.web.cern.ch/alice-hmpid/>, 2002.
- [32] J. Schnapka, “Doppelspurerkennung unter Verwendung der Kathodenauslese am ZEUS-Übergangsstrahlungsdetektor,” Master’s thesis, Universität Bonn, Bonn, October 1998.
- [33] B. Dolgoshein, “Transition radiation detectors,” *Nuclear Instruments and Methods in Physics Research Section A: Accelerators, Spectrometers, Detectors and Associated Equipment*, vol. 326, no. 3, pp. 434 – 469, 1993.
- [34] M. Krammer, “Detektoren zur Teilchenidentifikation.” www.hephy.at/project/halbleiter/VOSkriptum/VO-7-TeilchenID.pdf, 2009.

REFERENCES

- [35] S. J. Aplin, *Monte Carlo Simulation of Transition Radiation and Detectors in High Energy Physics*. PhD thesis, University of Portsmouth, January 2004.
- [36] W. F. Inc., “Wikipedia.” www.wikipedia.org, 2001.
- [37] ALICE collaboration, “ALICE TRD Technical Design Report,” Tech. Rep. CERN/LHCC 2001-021, CERN, October 2001.
- [38] T. Gunji, “Study of Electron Identification Capability of the ALICE Transition Radiation Detector,” Master’s thesis, University of Tokyo, 2003.
- [39] D. Emschermann, “ALICE TRD in Heidelberg.” <http://www.physi.uni-heidelberg.de/~demscher>, 2011.
- [40] J. Klein, “Triggering with the ALICE TRD,” *nucl-ex*, December 2011, arXiv:1112.5110v1.
- [41] C. Adler, “Position reconstruction in drift chambers operated with Xe, CO₂ (15%),” *Nuclear Instruments and Methods in Physics Research Section A: Accelerators, Spectrometers, Detectors and Associated Equipment*, vol. 540, no. 1, 2005.
- [42] CERN, “LHC - experiments Gas Control Systems.” <http://j2eeps.cern.ch/wikis/display/EN/LHC-GCS>, 2012.
- [43] IT-CO Gas Working Group, *A common approach for the control of the LHC experiments gas systems*. CERN, September 2009.
- [44] A. A. et al., “Pulse height measurements and electron attachment in drift chambers operated with Xe,CO₂ mixtures,” *physics.ins-det*, March 2003, arXiv:physics/0303059v1.
- [45] C. Garabatos, “TRD gas regeneration by cryogenic distillation.” CERN internal note, September 2002.
- [46] A. Andronic, S. Biagi, P. Braun-Munzinger, C. Garabatos, and G. Tsileidakis, “Drift velocity and gain in argon- and xenon-based mixtures,” *physics.ins-det*, p. 7, February 2004, arXiv:physics/0402044v1.

REFERENCES

- [47] J. H. Hubbell and S. M. Seltzer, “Tables of X-Ray Mass Attenuation Coefficients and Mass Energy-Absorption Coefficients from 1 keV to 20 MeV for Elements $Z = 1$ to 92 and 48 Additional Substances of Dosimetric Interest*.” <http://www.nist.gov/pml/data/xraycoef/index.cfm>, September 2009.
- [48] N. Mandal and G. Mandal, “Measurement of gas concentrations: oxygen, carbon dioxide, nitrogen, nitrous oxide and volatile anaesthetic agents,” *Anaesthesia; Intensive Care Medicine*, vol. 9, December 2008.
- [49] Systech Instruments Ltd and Illinois Instruments, Inc., “Systech Illinois.” <http://www.systechillinois.com>, 2010.
- [50] ALEPH collaboration, “The ALEPH detector and subdetectors - The Electromagnetic Calorimeter.” <http://aleph.web.cern.ch/aleph/aleph/SUBDET/ecal.html>, November 1999.
- [51] C. Garabatos, “Status TPC and TRD gas.” ALICE Technical Board, March 2011.
- [52] P. von Walter, “Personal communication,” April 2009.
- [53] C. Markert, “Driftgeschwindigkeitsmessung zur Gasüberwachung im NA49-Experiment,” Master’s thesis, Goethe Universität, Frankfurt, September 1995.
- [54] C. Lippmann, “Aufbau und Inbetriebnahme eines Gasqualitätsmonitors für die HADES-Driftkammern,” Master’s thesis, Goethe Universität, Frankfurt, September 2000.
- [55] A. Gärtner, “Kalibrierung der Driftgeschwindigkeit von Elektronen im Kammergas der Vorwärts-Spurdriftkammern des Experiments STAR,” Master’s thesis, Max-Planck-Institut für Physik, München, January 2002.
- [56] D. Wegerle, “Ein Gasmonitor für den Übergangsstrahlungszähler des ALICE-Experimentes,” Master’s thesis, Goethe Universität, Frankfurt, June 2008.
- [57] J. F. C. Hernández, “Entwicklung eines Ternärgasgemischmonitors,” Master’s thesis, Technische Universität, Darmstadt, May 2006.

REFERENCES

- [58] D. Antonczyk, *Detailed Analysis of Two Particle Correlations in Central Pb-Au Collisions at 158 GeV per Nucleon*. PhD thesis, Technische Universität, Darmstadt, October 2006.
- [59] J. F. C. Hernández, *Charged particle multiplicity studies in proton-proton collisions at a centre-of-mass energy of 10 TeV with the ALICE detector*. PhD thesis, Universität Heidelberg, 2010.
- [60] D. Wegerle, “Gas Monitor for the ALICE TRD.” DPG Frühjahrstagung, March 2007.
- [61] CERN - EP/ED, *ALICE TPC Readout Chip User Manual*. CERN, June 2002.
- [62] M. Arslandok, “Progress in Gas Monitoring System GOOFIE.” ALICE TPC weekly meeting, December 2011.
- [63] M. Arslandok, “Personal communication,” 2012.
- [64] S. Dyba, “Personal communication,” 2012.
- [65] Digi International, *DIGI ONE SP IA - Industrial Serial Server*. USA, 2009.
- [66] A. Augustinus, P. Chochula, L. S. Jirdén, M. Lechman, P. Rosinský, O. Pinazza, G. D. Cataldo, A. N. Kurepin, and A. Moreno, “COMPUTING ARCHITECTURE OF THE ALICE DETECTOR CONTROL SYSTEM,” *Proceedings of ICALEPCS2011*, 2011.
- [67] P. Cochula, “Windows Terminal Services for the ALICE Detector Controls System.” <http://alicedcs.web.cern.ch/AliceDCS/Documents/>, August 2006.
- [68] J. Mercado, *Development of the control system of the ALICE Transition Radiation Detector and of a test environment for quality-assurance of its front-end electronics*. PhD thesis, Ruperto-Carola University, Heidelberg, November 2008.
- [69] ETM, *PVSS II - Process visualization and control system - Getting Started - Basics*. Eisenstadt, Austria, 2 ed., July 2004.

REFERENCES

- [70] M. Gonzales-Berges, “The Joint COntrols Project Framework,” *Physics*, 2003.
- [71] L. Jirdèn, “The ALICE Control System,” *ICFA Beam Dynamics Newsletter*, vol. 47, p. 191, December 2008.
- [72] O. Busch, “The Detector Control System of ALICE TRD,” *Nucl. Instr. Meth. A*, September 2011.
- [73] “ALICE TRD Project.” <https://wiki.kip.uni-heidelberg.de/ti/TRD/index.php>, 2012.
- [74] ALICE collaboration, “ALICE Technical Design Report of the Trigger, Data Acquisition, High-Level Trigger and Control System,” tech. rep., CERN, Geneva, December 2003.
- [75] D. Evans, “The ALICE Central Trigger Processor.” Real Time Conference, 2005. 14th IEEE-NPSS, June 2005.
- [76] S. Kirsch, “Development of the Supermodule Unit for the ALICE Transition Radiation Detector at the LHC (CERN),” Master’s thesis, Universität Heidelberg, Heidelberg, September 2007.
- [77] T. Anticic, V. Barroso, F. Carena, W. Carena, S. Chapeland, O. Cobanoglu, E. Dénes, R. Divià, U. Fuchs, T. Kiss, I. Makhlyueva, F. Ozok, F. Roukoutakis, K. Schossmaier, C. Soós, P. V. Vyvre, and S. Vergara, “Commissioning of the ALICE data acquisition system,” *Journal of Physics: Conference Series*, vol. 119, no. 2, 2008.
- [78] S. Zimmer, “Design, Implementation and Commissioning of the Pretrigger System for the Transition Radiation Detector at the ALICE experiment of CERN,” Master’s thesis, Universität Heidelberg, Heidelberg, 2008.
- [79] J. Lehnert, “Status of the Pretrigger System for the ALICE Transition Radiation Detector,” *GSI Scientific Report*, no. 61, 2009.
- [80] S. Schmiederer, “Development and Implementation of the Control System for the Pre-Trigger System of the Transition Radiation Detector at ALICE,” Master’s thesis, Universität Heidelberg, Heidelberg, 2009.

REFERENCES

- [81] F. Reidt, “Development and Implementation of a Diffractive-Gap Trigger for the ALICE TRD Pre-Trigger System.” Bachelor Thesis, June 2010.
- [82] T. Dietel, J. Klein, K. Oyama, and K. Schweda, *TRD Documentation Project*, subversion rev: 3788 ed., February 2012.
- [83] K. Oyama, “TRD Pre-Trigger System.” <http://alice.physi.uni-heidelberg.de/oyama/PreTrigger/pkwk/>, August 2007.
- [84] J. Lehnert, “Readout of the TRD Pretrigger System ”PIMDDL Project”.” ALICE TRD Meeting, August 2010.
- [85] Institutt for Fysikk og Teknologis, “Electronics for the Time Projection Chamber (TPC).” <https://wikihost.uib.no/ift/index.php>, 2012.
- [86] V. Angelov, “Personal communication,” 2011.

Danksagung

Zunächst möchte ich mich bei meinem Doktorvater Prof. Dr. Harald Appelshäuser für die Aufnahme in seine Arbeitsgruppe und die Ermöglichung des Aufenthalts am CERN bedanken. Mein größter Dank gilt Dr. Chilo Garabatos, der es mir während der dreieinhalb Jahre am CERN zwar nicht immer einfach gemacht hat, von dessen Wissen ich jedoch in höchstem Maße profitieren und lernen konnte. Auch danke ich Dr. Ken Oyama, Dr. Kai Schweda und Dr. Jörg Lehnert für die Betreuung sowie der gesamten TRD Kollaboration für die Zusammenarbeit.

Über allem stehen jedoch Cátia und meine Familie, ohne die ich sicher nicht bis zum Ende durchgehalten hätte. Durch ihre moralische Unterstützung konnte ich diese Arbeit überhaupt erst verfassen.

Grazie, Attilio e Ombretta! Merhaba, Mesut! Danke, Yvonne, Hans, Uli, Tim, Bastian, Christian, Tobias und Frederick! Thanks, Steven! Gracias, Jorge!

Curriculum Vitae

NORA PITZ

Am Brauhaus 13

35584 Wetzlar

Germany

Phone: +49-6441-32625

E-Mail: Nora.Pitz@cern.ch

EDUCATION

08/08 - Present Ph.D. Student - Johann Wolfgang Goethe-University

10/03 - 07/08 Diploma Physics - Johann Wolfgang Goethe-University

07/00 - 06/03 Grammar School (Abitur) - Goethe-School-Wetzlar

HONORS AND AWARDS

08/08 - present Support for Ph.D. research studies from the German Federal
Ministry of Education and Research (BMBF)

2009 Michael Loulakis-Preis of the Frankfurter Förderverein für
Physikalische Grundlagenforschung and the University of Frank-
furt

2001 Scholarship for four weeks of high-school in the USA (11th grade)

Curriculum Vitae

SCIENTIFIC SCHOOLS

- 10/08 - present Helmholtz Graduate School for Hadron and Ion Research
- 05/06 - 05/07 Mentoring program for women in science and engineering
“MENTORINNENNETZWERK”

PROFESSIONAL EXPERIENCE

- 03/07 - 07/08 Support of a laboratory experiment for undergraduate students
at the Uni of Frankfurt (Experimental Physics)
- 10/06 - 03/07 Function as a tutor at the Uni of Frankfurt (Atomic Physics)
- 12/04 - 11/06 Part time job at EINSATZ marketing agency
- 11/03 - 12/04 Part time job at RHEIN MAIN TV
- 2003 Debt collection agency
- 2002 WETZLARER NEUE ZEITUNG (local newspaper)
- 2001 BUDERUS steel
- 2000 IBC bearings

THESIS

- 2012 Dissertation: “Gas system, gas quality monitor and detector control of the ALICE Transition Radiation Detector [and studies for a pre-trigger data read-out system]”, Johann Wolfgang Goethe-University
- 2008 Diploma: “Irradiation tests with neutrons on Large Area Avalanche Photo Diodes for the electromagnetic calorimeter of the PANDA-detector”, Johann Wolfgang Goethe-University

MEMBERSHIP IN RESEARCH ORGANIZATIONS

Deutsche Physikalische Gesellschaft

Physikalischer Verein Frankfurt

ADDITIONAL SKILLS

Languages	German (mother tongue)
	English (fluent)
	French (proficient)
	Italian (conversant)
OS	MacOSX, Linux, Windows
Comp. appl.	Adobe Illustrator, Adobe Photoshop, Adobe Acrobat, C++, LaTeX, XEmacs, Microsoft Word, Microsoft Excel, Microsoft PowerPoint, OpenOffice, Keynote, LabView

INTERESTS	Player of competitive rugby
	Player of competitive softball (Germany, Switzerland, France)
	Former coach of a softball team
	Softball referee (B licence)
	Other sports: swimming, running, cycling, ski, snowboard